Universidad de la República

Facultad de Ciencias

Departamento de Astronomía

Master thesis

Systematic census of RR Lyrae in Milky Way stellar streams

Author:
Lic. Ing. Bruno Domínguez

Advisors:
Prof. Dra. Cecilia Mateu
Dr. Pau Ramos

November 7, 2025

Abstract

Nearly 150 tidal streams are known today; yet, full phase-space information exists for only a handful. RR Lyrae stars (RRL) – pulsating horizontal branch stars that serve as excellent standard candles – offer a powerful means to probe these structures, but they have only been specifically identified in less than dozen streams. In this work we study the RRL population in all the known stellar streams with reported proper motion in the `galstreams` library, performing the first systematic census of these stars across the streams. Our goals are to *i)* identify likely RRL members, *ii)* map distances along streams, and *iii)* compare RRL populations in streams and surviving progenitors. We use a union of the largest RRL catalogs (Gaia DR3 SOS, PS1, and ASAS-SN-II) to construct a Bayesian probabilistic membership model and associate RRL to the 56 streams (75 tracks) studied. We find that only 32 of the 56 streams have RRL in their tidal tails – 13 with progenitors and 19 without. Of these, 13 streams present more than 3 RRL in their tails. We report new RRL detections in 31 of the 32 streams with identified RRL, anchoring the distances of the streams and, in particular, inferring new distance gradients for 5 stellar streams. Our method also provides intrinsic dispersion estimates in distance and proper motion for each track and statistically quantifies the expected contamination. In addition, the census revealed some complex origin histories, such as the new plausible origin scenario we propose for M92 with multiple progenitors. We also find that the presence of RRL in the tidal tails is linked to the late stages of progenitor dissolution. This census represents a first step toward identifying which of the studied stellar streams contain a significant number of RRL based on currently reported tracks while also providing a homogeneous and robust catalog of RRL members with precise empirical distances, crucial for a full phase-space analysis of these structures and their use to probe the Galaxy.

Resumen

Hoy se conocen alrededor de 150 corrientes de marea; sin embargo, sólo existe información completa en el espacio de fases para unas pocas. Las estrellas RR Lyrae (RRL) – estrellas pulsantes de la rama horizontal que sirven como excelentes estándares de luminosidad – ofrecen un poderoso medio para estudiar estas estructuras, pero sólo han sido específicamente estudiadas en menos de una docena de corrientes. En este trabajo estudiamos la población de RRL en todas las corrientes estelares conocidas con movimientos propios reportados en la biblioteca `galstreams`, realizando el primer censo sistemático de estas estrellas entre las corrientes. Nuestros objetivos son: *i)* identificar probables miembros RRL, *ii)* mapear distancias a lo largo de las corrientes, y *iii)* comparar las poblaciones de RRL en las corrientes y en sus progenitores supervivientes. Usamos la unión de los catálogos más grandes de RRL (Gaia-DR3 SOS, PS1 y ASAS-SN-II) para, a través de un modelo Bayesiano de probabilidad de membresía, asociar RRL a las 56 corrientes (75 trazas) estudiadas. Encontramos que sólo 32 de las 56 corrientes tienen RRL en sus colas de marea – 13 con progenitor identificado y 19 sin ellos. De estas, 13 corrientes presentan más de 3 RRL en sus colas. Reportamos nuevas detecciones de RRL en 31 de las 32 corrientes con RRL identificadas, anclando las distancias de las corrientes y, en particular, infiriendo 5 nuevos gradientes de distancia. Nuestro método también provee estimaciones de dispersiones intrínsecas en distancia y movimiento propio para cada traza y estadísticamente cuantifica la contaminación esperada. Además, el censo reveló algunas historias de origen complejas, como el nuevo y plausible escenario de origen con múltiples progenitores que proponemos para M92. También encontramos que la presencia de RRL en las colas de marea está vinculada a las etapas finales de la disolución del progenitor. Este censo representa un primer paso hacia la identificación de las corrientes estelares estudiadas que contienen un número significativo de RRL basándose en las trazas actualmente reportadas, mientras que también proporciona un catálogo homogéneo y robusto de miembros RRL con distancias empíricas precisas, crucial para el análisis completo en el espacio de fases de estas estructuras y su uso para estudiar la Galaxia.

Contents

Chapter 1

Introduction

Currently, it is known that galaxies like our own have grown by gradually assimilating smaller galaxies in what is called 'hierarchical formation' (e.g., White & Rees, 1978; White & Frenk, 1991). These accretion events have left behind fossil records that can be discovered by studying the most ancient populations, such as the Galactic halo (e.g., Naidu et al., 2020; Helmi, 2020; Deason & Belokurov, 2024). An important part of these fossil records are the globular clusters present in the halo, many of which were brought into the Milky Way through the accretion of their respective host galaxies (e.g., Searle & Zinn, 1978; Zinn, 1993; Kruijssen et al., 2019; Callingham et al., 2022). But these are only the surviving clusters. During the accretion process, clusters and dwarf galaxies can be disrupted due to tidal forces, causing the stars to escape from the progenitor, approximately tracing its orbit and producing a dynamically coherent structure called 'stellar stream' (e.g., Helmi et al., 1999; Combes et al., 1999; Eyre & Binney, 2009). Fig. 1.1 shows four examples of stellar streams found in the Milky Way, from top to bottom: GD-1, Pal 5, Jhelum, and Orphan-Chenab (OC).

Thanks to the arrival of large area photometric surveys such as the Sloan Digital Sky Survey (SDSS, York et al., 2000), the *Gaia* mission (Gaia Collaboration et al., 2016), and the Dark Energy Survey (DES, Shipp et al., 2018), almost 150 stellar streams are known in the Galaxy today, as shown in Fig. 1.2 (from Mateu, 2023), most of which have likely been produced by globular clusters (Bonaca & Price-Whelan, 2025). Being dynamically cold structures, they are powerful tools for inferring the gravitational potential of the Milky Way (e.g., Ibata et al. 2021, hereafter I21; Ibata et al. (2024); Palau et al. 2025) providing constraints on the enclosed mass and the distribution of dark matter; as well as the nature of dark matter itself through the study of perturbations such as gaps, blobs, and spurs (see top panel of Fig. 1.1), from which constraints on the underlying distribution of subhalos could be inferred (e.g, Price-Whelan & Bonaca, 2018; Bonaca et al., 2019b; de Boer et al., 2020). In addition, streams are sensitive to encounters with massive objects like the Magellanic Clouds or the Sagittarius dwarf galaxy, which can cause misalignments between their celestial paths and the velocities of their members (e.g., Mateu, 2023; Koposov et al., 2023), as shown in the bottom panel of Fig. 1.1. Unveiling these interactions can help to decipher the dynamic history of the Milky Way and to rebuild its past. On smaller scales, residuals of past accretion events can also be traced in stellar streams that exhibit multiple components, such as a cocoon feature (see middle bottom panel of Fig. 1.1), further enriching the fossil record of the Galaxy assembly (Malhan et al., 2021a). Moreover, studying the dynamic properties of the stellar streams, such as their integrals of motion, also allows us to associate different streams with the different massive accretion events that built our Galaxy and to obtain a more complete picture of its formation history (Bonaca et al., 2021). In order to conduct all these kinds of studies, full phase-space information for the stellar streams is required; yet, empirical distance information exists for only about half of the known streams (Mateu, 2023).

One way to overcome this issue is to work with RR Lyrae stars (RRL), pulsating horizontal branch giants that serve as excellent standard candles. There are mainly two types of RRL: the *ab* type (RRab), which pulsate in their fundamental mode, and the *c* type (RRc), which pulsate in their first

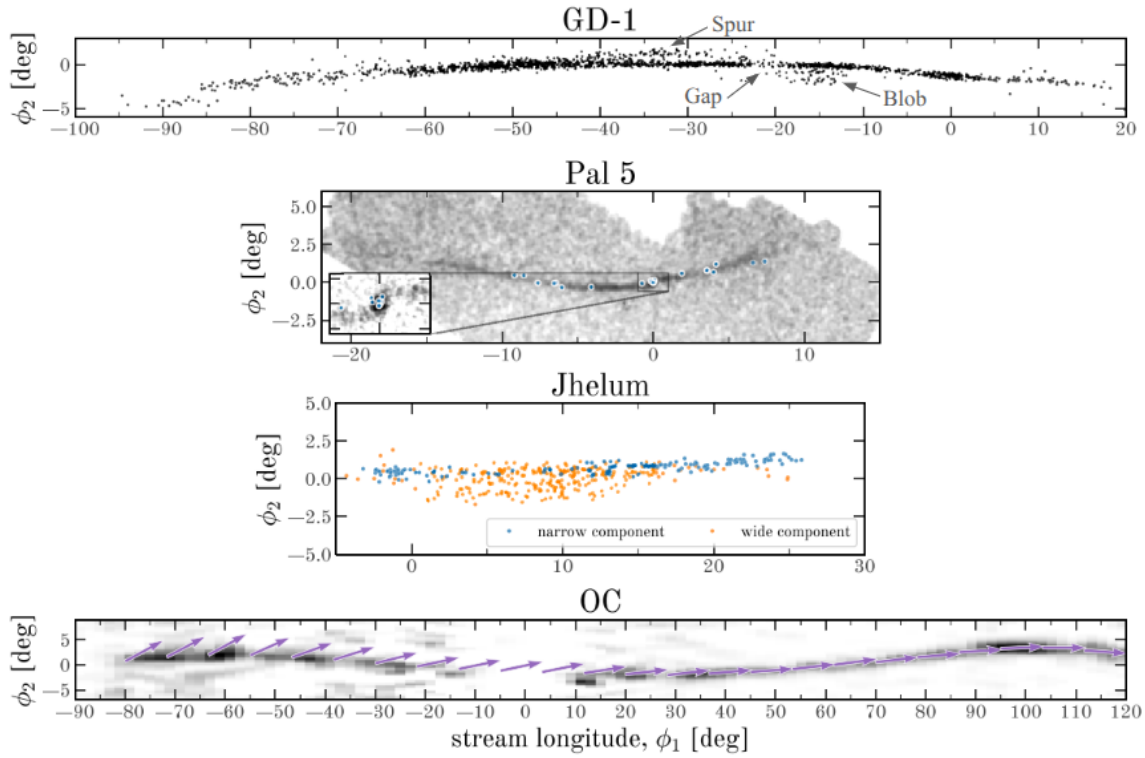

Figure 1.1: Four examples of observed stellar streams showing the complexity and diversity of morphologies they might present; they are shown in the frame of reference of each stream where ϕ_1 is the stream-aligned longitude and ϕ_2 is the stream-aligned latitude. **Top panel:** The GD-1 stream, which shows clear perturbations such as spurs, gaps and blobs. **Middle top panel:** The Palomar 5 (Pal 5) stream, the blue circles are RR Lyrae stars associated with the stream reported by Price-Whelan et al. (2019). **Middle bottom panel:** The Jhelum stream, which present an overlapping narrow and broad component in sky. **Bottom panel:** The Orphan-Chenab (OC) stream, a very long stream useful to infer the gravitational potential of the Milky Way and presents strong misalignments between the position of the stars in the stream (gray-scale image) and their proper motions (violet arrows). Figure adapted from Bonaca & Price-Whelan (2025).

overtone mode (Smith, 1995). Figure 1.3 shows the amplitude-period diagram, indicating the loci occupied by RRab and RRc, which illustrates the shorter periods of the RRc with respect to the RRab and the anti-correlation between the amplitude and the period of the RRab. RRL are abundant in globular clusters and have proven to be excellent tracers of the canonically oldest ($\gtrsim$ 10 Gyr) and metal-poor ([Fe/H]< -0.5) populations in the Galaxy, mainly the halo (Vivas et al., 2006a,b; Iorio & Belokurov, 2021), bulge (Kunder et al., 2008; Prudil et al., 2024a,b), and thick disk (Mateu & Vivas, 2018, and references therein). Being luminous stars and one of the few astronomical objects for which distances can be measured with great precision ($\lesssim 5\%$), they serve as ideal markers for studying the six-dimensional structure of the Galaxy when combined with all-sky kinematic information (Iorio & Belokurov, 2021). Therefore, by identifying which RRL belong to the different stellar streams, we can anchor a precise mean distance to all of them and, in cases with numerous RRL populations, determine a distance gradient along the stream. In addition, we can estimate the masses of the streams and study the properties of their population compared to the progenitor population while the latter still exists, allowing us to understand more about the origins of the stellar system.

Despite the powerful utility of the RRL, so far only a handful of streams have been characterized using RRL: Orphan (Koposov et al., 2019), Palomar 5 (Price-Whelan et al., 2019), LMS-1 (Yuan et al., 2020), and Sagittarius (e.g., Ramos et al., 2020); however, these studies rely on completely different

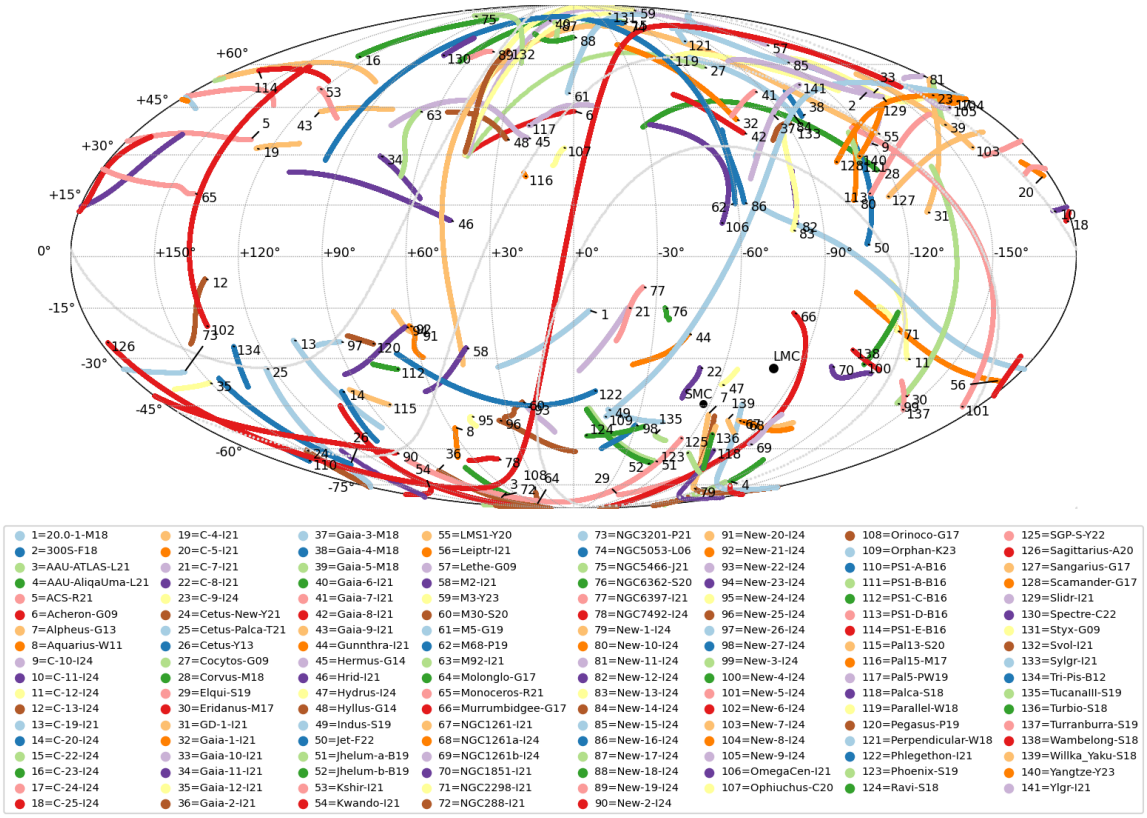

Figure 1.2: All known stellar stellar streams reported in the `galstreams` library (Mateu, 2023).

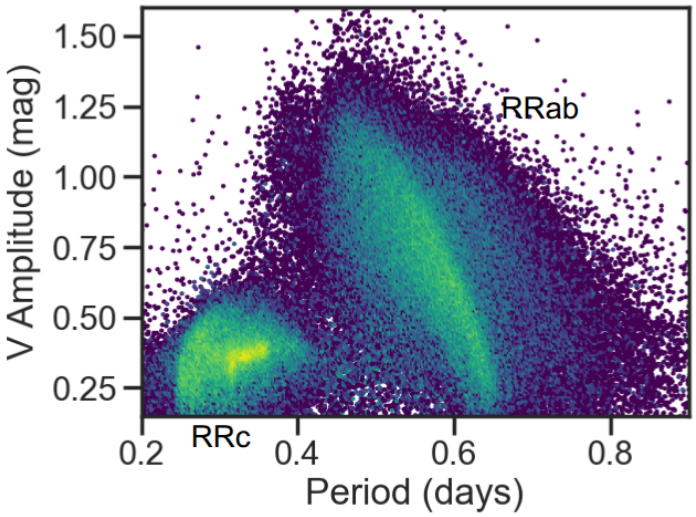

Figure 1.3: Amplitude-Period diagram of all the RRL of our catalog (see Sec. 2) color coded by number density, showing the locus of the two mainly types of RRL.

catalogs and methods – some with kinematic information and some without – making comparison of their results difficult. There have also been a few studies that have systematically searched for RRL in stellar streams with associated progenitors: Kundu et al. (2019) and Abbas et al. (2021) in globular clusters and Vivas et al. (2020) and Tau et al. (2024) in dwarf galaxies. However, in these studies, the RRL were visually associated based on positional, proper motion, and color-magnitude diagram criteria. In addition, several other studies (e.g., Shipp et al. 2019; Hanke et al. 2020; I21; Xu et al. 2024; Li et al. 2019) have searched for stream members in general and, in some cases, have identified RRL as well; however, these works were not specifically designed to target RRL or exploit their properties to study the stream populations.

These precedents highlight the need to conduct a systematic and robust RRL census of all known streams, which, additionally to enabling a homogeneous study of the RRL stream population, also allows for a comparison between the populations in clusters and in their tidal tails for streams with surviving progenitors particularly, since RRL are very common in globular clusters. For example, the RRL population of the Palomar 5 (Pal 5) stream was characterized in detail by Price-Whelan et al. (2019) using a probabilistic kinematics membership model. They identified 10 RRL within the tidal radius of the cluster and nearly twice as many in the tidal tails (blue circles in the middle top panel of Fig. 1.1). This study revealed an intriguing segregation in the RRL population of the stream: while most of the RRc (67%) are in the cluster, the majority of the RRab (87%) are in the tails. This raises several questions: Is such segregation a standard feature across streams or just a peculiarity of Pal 5? Could other types of segregation exist in the stellar population of the stream that are not reported yet? How frequent are RRL in the tidal tails of globular clusters?

The general goal of this work is, therefore, to study the RRL population of known stellar streams by performing a systematic census. The specific goals are as follows:

1. To implement a probabilistic membership model following Price-Whelan et al. (2019) to identify RRL associated with each of the known stellar streams with proper motion information reported in the `galstreams` library (Mateu, 2023).

2. Based on the RRL membership:

   (a) Determine the distance to each stream as a function of an angular coordinate along the stream.

   (b) Compare the RRL populations of the stream and progenitor and investigate possible differences.

The structure of the present work is as follows: In Chapter 2, we describe the RRL catalogs used to search for stream members, the `galstreams` library (Mateu, 2023) from which we obtain the stream information reported in the literature, and the catalogs where the information about the surviving progenitors can be found. In Chapter 3, we describe the probabilistic membership model implemented to identify candidate members of the streams. In Chapter 4, we present the identified RRL members for each stream individually and discuss their properties. Meanwhile, in Chapter 5, we use our results to discuss the statistical properties of the population of streams and shed light on the possible origins of a selection of streams. Finally, in Chapter 6, we present the conclusions and summarize the contributions of the thesis.

Chapter 2

Data

We used a catalog of 309,998 RRL conformed by the union of the Gaia DR3 Specific Objects Study (SOS, Clementini et al., 2023), Panoramic Survey Telescope and Rapid Response System 1 (Pan-STARRS1 (PS1), Sesar et al., 2017), and All-Sky Automated Survey for Supernovae II (ASAS-SN-II, Jayasinghe et al., 2019) RRL catalogs, the largest and most complete RRL catalogs currently available (Mateu et al., 2020; Mateu, 2024). This compilation is similar to the catalog used in Cabrera-Gadea et al. (2024), where the details of distance calculations are explained, except that in this work, for stars without a photometric metallicity estimate, we assigned a metallicity drawn from a normal distribution with a mean of -1.2 dex and a standard deviation 0.5 dex mimicking the average properties of (kinematically selected) halo stars in Gaia DR3 SOS according to Li et al. (2023). We restricted the final catalog to stars with RUWE < 1.4 to ensure the quality of the astrometric parameters, following the recommendation of Lindegren et al. (2021).

In this work we are not trying to find new streams, but to find RRL members of those already known. To do this, we use `galstreams` (Mateu, 2023), the most complete library of stellar streams in the Milky Way with reported tracks in the sky, proper motion, distance, and radial velocity when available. We will follow the same nomenclature introduced in this work: A *stream* is the object of study and each is unique, while a *track* is the measure of a property (sky position, proper motion or radial velocity) of the stream as a function of an angle. Different tracks may have been reported in the literature by different authors; therefore, in many cases multiple tracks exist for the same stream. Full details are explained in Mateu (2023). It is worth mentioning that Mateu (2023) refers to `galstreams v1.0`, while in this work we use `galstreams v1.2`, whose main updates are: the addition of more than 40 new streams, more than 40 new tracks for previously known streams (including radial velocity tracks), and information about the observed widths in the sky and in proper motion. In this version, there are 217 tracks that correspond to 137 unique streams, of which only 56 streams (75 tracks) have proper motion information. We exclude from the present analysis the tracks of Sagittarius-A20 (Antoja et al., 2020; Ramos et al., 2020; Ibata et al., 2020; Ramos et al., 2022), LMS1-Y20 (Yuan et al., 2020), and Cetus-Palca-Y21 (Yuan et al., 2022) because these are too long for our method to yield reliable results. We also exclude the Monoceros-R21 and ACS-R21 tracks (Ramos et al., 2021) because, even though they are included in `galstreams`, as noted by Mateu (2023) these structures are not considered to be real stellar streams but overdensities formed by stars kicked out of the Galactic plane (e.g., de Boer et al., 2018; Laporte et al., 2020); therefore, we do not consider them in this study.

In the case of streams with an associated progenitor, we used the astrometric, kinematic, and structural properties of globular clusters from the Database of Fundamental Parameters of Galactic Globular Clusters[1] (DbGC, Baumgardt & Hilker, 2018; Baumgardt & Vasiliev, 2021; Vasiliev & Baumgardt, 2021; Baumgardt et al., 2023). For Tucana III, the only surviving dwarf galaxy with an associated stream in our sample, we used data from Drlica-Wagner et al. (2015).

[1] https://people.smp.uq.edu.au/HolgerBaumgardt/globular/

Chapter 3

Method

With the aim of associating the RRL with the different stellar streams, we constructed a Bayesian probabilistic membership model. Taking the celestial, distance and proper motion tracks reported in `galstreams` as true, each star is modeled as having a probability of belonging to the stream in addition to a probability of belonging to the background, both of which depend exclusively on the star's distance and proper motion. We then estimate the membership probability as described below, and if this probability is higher than 50% and the star is near the celestial track, we classify that RRL as a member of the stream. In what follows, we describe the sample selection used followed by the details of the Bayesian model.

3.1 Sample selection

For each stream, we restrict our search for members to a sky window defined in the stream frame of reference $\phi_1 - \phi_2$, the rotated spherical coordinate system aligned with the stream, as reported in `galstreams`. To define it, we start by taking the sky track and width (σ_{ϕ_2}) of the stream from `galstreams`. The length of the window in ϕ_1 is taken as 1.5 times the length of the sky track in ϕ_1. For the window limits in ϕ_2, we take the maximum (minimum) of the sky track in ϕ_2 and add (subtract) $11\sigma_{\phi_2}$[1], placing the stream in the center of the window in both coordinates. Within this sky window, we define two regions of interest: an on-stream region defined as a polygonal footprint around the sky track with a width equal to $6\sigma_{\phi_2}$, and an off-stream region defined as two footprints parallel to the stream footprint, one immediately above (in ϕ_2) and the other immediately below, each with a width equal to $6\sigma_{\phi_2}$ and extended in all ϕ_1 within the sky window.

In some tracks, we took more extended regions on and off-stream in ϕ_2 in order to have enough stars for a robust representation of the background. In the case of TucanaIII-S19 (Shipp et al., 2019), we took a width of $9\sigma_{\phi_2}$ for each region (and therefore add/subtract $15.5\sigma_{\phi_2}$ to define the window's width). For M2-I21 and Kshir-I21 (I21), we took $8\sigma_{\phi_2}$for each region ($14\sigma_{\phi_2}$ to define the window's width). For Elqui-S19 (Shipp et al., 2019) and Spectre-C22 (Chandra et al., 2022), we took $10\sigma_{\phi_2}$ and $8\sigma_{\phi_2}$, respectively, for the off-stream region (therefore, $15\sigma_{\phi_2}$ and $13\sigma_{\phi_2}$ to define the window's width, respectively).

Finally, we also define limits along the line of sight by making a box for our search: we extrapolate the distance track up to the limits of the sky window in ϕ_1, select its maximum (minimum) value, and add (subtract) to it 4 times its 10% which corresponds to the mode of the distance error distribution. In Table A.1 we show a summary of the properties used for each track.

Once the box is defined, we remove from the sample all known globular clusters and dwarf galaxies that happen to fall inside our selection but are unrelated to the stream of interest. We do that by

[1]The size of the sky window was taken arbitrarily, but large enough to cover the stream and the control areas around it.

removing the stars within the tidal radius, r_t, of each of the contaminant objects. We also remove all RRL with latitude $|b| < 15^\circ$ (or $|b < |b_{\rm prog}| - r_t$ in the case of stream progenitors with latitude $|b_{\rm prog}| < 15^\circ$) to avoid the Galactic disk, and those within 6° from the Sagittarius-A20 (Antoja et al., 2020; Ramos et al., 2020) sky track when the distance track is also between the limits along the line of sight defined for the target stream.

3.2 Bayesian model

In this study, we work with 56 streams that have distance and proper motion tracks already reported in the literature; 12 of them have more than one track associated, leaving us with 75 tracks in total to analyze. We take these tracks as 'true' and use them to find the RRL's membership probability of belonging to each stream. To do this, we constructed a Bayesian probabilistic mixture model in proper motions and distance, $\vec{y_n} = (\mu_{\phi_1}, \mu_{\phi_2}, d)$, following Price-Whelan et al. (2019), which takes the form:

$$p\left(\mathbb{C}_{int}, f \mid \vec{y_n}\right) \propto p(\mathbb{C}_{int}, f) \prod_n^N \mathcal{L}(\vec{y_n} \mid \mathbb{C}_{int}, f), \tag{3.1}$$

where $p\left(\mathbb{C}_{int}, f \mid \vec{y_n}\right)$ is the posterior probability of the model parameters $\mathbb{C}_{int}$, the intrinsic covariance matrix, and f, the stream's RRL fraction; $p(\mathbb{C}_{int}, f)$ is the prior probability distribution over the parameters, and $\mathcal{L}(\vec{y_n} \mid \mathbb{C}_{int}, f)$ is the likelihood probability for the n-th star, given the model parameters.

3.2.1 The likelihood

The likelihood is modeled as the weighted sum of the probability that the RRL belongs to the stream, $p_{\rm st}$, plus the probability of belonging to the background, $p_{\rm bkg}$:

$$\mathcal{L}(\vec{y_n} \mid \mathbb{C}_{int}, f) = f p_{{\rm st},n} + (1 - f) p_{{\rm bkg},n} \tag{3.2}$$

The weight f is the stream versus background RRL ratio in the on-stream region (i.e., where the inference is made) and is a free parameter of the model.

Stream probability

The probability that a star belongs to the stream $p_{{\rm st},n} = \mathcal{N}(\vec{y_n} \mid \vec{y}(\phi_1), \mathbb{C})$ is modeled as a multivariate normal distribution, whose center follows the stream track[2] $\vec{y}(\phi_1)$. The Gaussian noise, $\mathbb{C}$, is taken as the quadratic sum of the intrinsic dispersion ($\mathbb{C}_{int}$) and observational noise ($\mathbb{C}_{obs}$) in proper motion and distance, where the intrinsic dispersion is a diagonal matrix consisting of $\left(\sigma^{int}_{\mu_{\phi_1}}, \sigma^{int}_{\mu_{\phi_2}}, \sigma^{int}_{d}\right)$ squared. These are, in addition to f, the remaining free model parameters.

Background probability

We calculated the probability that a star belongs to the background, $p_{\rm bkg}$, from a fixed empirical Gaussian mixture model of the proper motions and distance inferred from the RRL in the off-stream region. We assumed here that the proper motion and distance are locally independent of their position in the sky, which allows us to make cuts in the sky without biasing the sample. Under this assumption, the distribution of proper motions and distances that we obtain in the off-stream region can be considered representative of the on-stream region.

The number of Gaussians used in the mixture model is determined by choosing the number of components that minimizes the Bayesian Information Criterion (BIC). Additionally, after some trial

[2]Internally, the `galstreams` track is fitted in (ϕ_1, ϕ_2) with a third degree polynomial to provide the extrapolation outside the reported track and for the likelihood to be evaluated at any arbitrary ϕ_1.

and error, we determined that, on average, there should be more than 15 RRL per Gaussian so that the background is well modeled and the results can be trusted. The streams whose backgrounds do not achieve this condition cannot be reliably studied using this method (see Sec. 4.1).

3.2.2 The priors

We assume that the prior is separable in all parameters. For the weight f, we adopt a uniform distribution between 0 and 1. For the prior on the intrinsic dispersions (in proper motions and distance), we use a hierarchical inference model. For the proper motion dispersions, we first infer the individual intrinsic tangential velocity dispersion for each stream with published members (generic stars, non-RRL) by de-convolving the observational errors. The resulting distribution of inferred intrinsic dispersions is used as a hyper-prior probability distribution for the *population* of streams, which is then used as a prior for the inference of the intrinsic proper motion dispersions for each individual stream based on the RRL. For the distance dispersions, we used a uniform prior between 0.001 kpc and 5 kpc as a hyper-prior.

Intrinsic proper motion dispersion hyper-prior

We first created a deconvolved distribution of the tangential velocity dispersion. To do this, we need proper motions, distances, and their uncertainties. Unfortunately, of the ∼150 streams, only 4 have all of this data for RRLs[3]; therefore, we looked for additional sources of information. We used the streams from I21 that have reported members (in general, not restricted to RRL) with both proper motion and distance. Proper motion uncertainties were obtained from Gaia DR3. For most reported members, distance uncertainties are not provided. To estimate them, we selected the I21's streams with a living progenitor and reported members within the progenitor's tidal radius and assumed that the true size of the progenitor is negligible compared to its distance and, therefore, that the distance dispersion is solely due to uncertainties. Based on these estimates, the distance uncertainties were found to be $\sim 10\%$.

Applying this distance error to the other streams with members and distance data from I21, we calculated their tangential velocities along with their respective uncertainties. Using an extreme deconvolution model (Holoien et al., 2017) with a single Gaussian, a tolerance of 1×10^{-8} and a maximum of iteration of 2048, we obtained a deconvolved dispersion of tangential velocities for each stream. We then fitted a gamma distribution to the resulting distribution of tangential velocity dispersions of the *population* of streams, for which we obtained $\alpha = 1.97507$ and $\beta = 0.06927$. This result was obtained using only streams with reported members from I21; nevertheless, similar values are found when the distance error calculation is extended to include all streams with reported members.

This distribution is then transformed into proper motion space using a median distance for each stream (d_{st}) according to:

$$p\left(\sigma^{int}_{\mu_{\phi_i}}\right) = f_\Gamma\left(\kappa\sqrt{2}d_{st}\sigma^{int}_{\mu_{\phi_i}}\right)\left|\kappa\sqrt{2}d_{st}\right| \tag{3.3}$$

where $\kappa = 4.74$ km yr/s and with

$$f_\Gamma(x) = \frac{\beta^\alpha}{\Gamma(\alpha)}x^{\alpha-1}\exp\left(-\beta x\right), \tag{3.4}$$

so we can use it as a prior for the intrinsic proper motion dispersions for each stream, $\sigma^{int}_{\mu_{\phi_1}}$ and $\sigma^{int}_{\mu_{\phi_2}}$.[4]

[3] NGC5466-J21 (Jensen et al., 2021), Pal5-PW19 (Price-Whelan et al., 2019), Cetus-Palca-T21 (Thomas & Battaglia, 2022), and LMS1-M21 (Malhan et al., 2021b)

[4] d_{st} in kpc and $\sigma^{int}_{\mu_{\phi_i}}$ in mas/yr.

Streams without reported members

For the case without reported members, the hyper-prior in Eq. 3.3 inferred for the population of streams is used as the prior in the inference of the intrinsic proper motion dispersions. For the intrinsic distance dispersion, the flat hyper-prior mentioned above is used.

Streams with reported members

For the case with reported members, we used the hyper-priors and the published stream members to obtain a posterior probability, which is then used as the (more informative) prior in the inference with the RRL.

To obtain the posterior probability, we used a simple Bayesian model where the likelihood is a Gaussian distribution, $\mathcal{N}(y_{i,n} \mid y_i(\phi_1), \mathbb{C}_i)$, centered on the track $y_i(\phi_1)$, with the covariance matrix being the sum of the observational and intrinsic noise, $\mathbb{C}_i = {\sigma_{i,n}^{obs}}^2 + {\sigma_i^{int}}^2$, the latter being the free parameter we want to infer. To sample the posterior probability, we used the same Markov Chain Monte Carlo (MCMC) sampler described in Sec. 3.3. However, since this inference involves only one free parameter, we ran the sampler with 8 walkers. This posterior has a mode and a variance, which are used to calculate the parameters α and β of a gamma distribution[5] that serves as a bespoke prior for each stream with reported members.

For the posterior probability of the intrinsic distance dispersion, we have three cases of reported members: *i)* members with distances and their uncertainties, *ii)* members with distances but without their uncertainties, and *iii)* members without distances nor their uncertainties. In the first case, we use the data from the members. In the second case, as we do not have the uncertainties available, we used the photogeometric distance uncertainties from Gaia DR3. For the last case, as we do not have any distance information, the flat hyper-prior was used. In addition, there were some cases in which the inference based on the reported members did not converge; in this case the flat hyper-prior was used instead.

3.3 Markov Chain Monte Carlo sampler

We used the MCMC affine-invariant ensemble sampler `emcee` (Foreman-Mackey et al., 2013) to generate samples of the posterior probability given by Eq. 3.1 over the parameters $(\mathbb{C}_{int}(\sigma^{int}_{\mu_{\phi_1}}, \sigma^{int}_{\mu_{\phi_2}}, \sigma^{int}_{d}), f)$. The inference is made using only the RRL within the stream region. As we have 4 free parameters, we used 40 walkers to run `emcee` for an initial 2^9 steps to 'burn-in' the sample, then reset and restart the sampler for another 2^{14} steps. We thinned the chains by keeping only every 225^{th} steps, leaving us with $M = 2880$ posterior samples. The thinning value is chosen so that it is greater than the autocorrelation time (estimated with `emcee`) for all streams.

3.4 Membership probability

Once the posterior probability is sampled, we compute the membership probability for each star n, following Foreman-Mackey (2014), as the average in the posterior samples of the probability of belonging to the stream over the total probability:

$$P_{\text{memb},n} \simeq \frac{1}{M} \sum_{m=1}^{M} \frac{f^m p^m_{\text{st},n}}{f^m p^m_{\text{st},n} + (1 - f^m) p_{\text{bkg},n}}, \tag{3.5}$$

[5] A gamma distribution satisfies: mode $= (\alpha - 1)/\beta$ and $\sigma^2 = \alpha/\beta^2$

In what follows, an RRL is considered a member if its membership probability is higher than 50% and the star falls within the extended stream region in the sky. The complete list of RRL members for every track studied is provided in Table B.1.

3.4.1 Contamination

The mixture model considers the existence of a background and models it in proper motion and distance. However, due to possible background variations along the stream, we also consider possible contamination from RRL that may have consistent proper motion and distance with the stream but are not real stream members. To estimate this, we count the number of RRL with a membership probability higher than 50% outside the extended stream region in the sky. Assuming that proper motion and distance are locally independent of their sky position, we scaled this number by the sky area to determine the expected number of contaminants or false positive members according to our model, within the stream region. With this procedure we cannot say which of the stars that we find with our method are truly members of the stream or just background stars that, by chance, align with it; however, this provides a statistical estimate of the number of background RRL that we expect to have wrongly selected as members.

Chapter 4

Results and discussion

4.1 Summary of results

In what follows, we present tables summarizing, for the full set of streams and per stream track, the results of the census performed by applying the method described in Sec. 3 to the 75 tracks in `galstreams` with proper motions and distance tracks, whose properties are summarized in Table A.1 in Appendix A.

Table 4.1 summarizes the numbers of streams with different numbers of RRL found in the tails, the progenitor, or with no RRL members found. Table 4.2 presents, for each stream track, the number of RRab and RRc identified in the progenitor (when it exists) and in the tails, the number of contaminants estimated as described in Sec. 3.4.1, and the inferred f and intrinsic dispersions in proper motion and distance. Uncertainties for these quantities were computed as the standard deviation of the marginalized posterior probability of each quantity. Five tracks presented too few RRL in their background for the method to be applied reliably (C-4-I21, C-5-I21, Gaia-2-I21, M5-I21, Phoenix-S19) and were not taken into account for the analysis.

In what follows, we focus the discussion on the streams with $\geqslant 3$ RRL member identified and separate the discussion into two cases: streams with an associated progenitor and streams without one. In each case, we discuss according to the number of RRL detected in the tails. For each stream, we analyze the track adopted by default in `galstreams`, unless specified otherwise.

4.2 Streams with an associated progenitor

We first discuss the 17 streams (25 tracks) with an associated progenitor. Out of these, four progenitors did not have any RRL in their tails (NGC 288, NGC 2298, NGC 2808 and NGC 6397), and in particular, NGC 6397 did not have any RRL at all.

In order to discuss RRL within the cluster or in the tails of the stream, we adopted the tidal radius described by Eq. 8 of Webb et al. (2013), which takes into account the orbit and the orbital phase of the cluster. When compared with previous studies, some adopted different criteria (e.g., the value

Table 4.1: Summary of the results: number of streams classified according to how many RRL we have detected in them.

	>3 RRL in tails	1-3 RRL in tails	RRL in prog. only	No RRL	Not reliable
With prog.	5	8	3	1	0
Without prog.	9	11	-	15	4

Table 4.2: Summary of results for each track (with enough RRL in their background to be able to apply the method reliably). (1) Track name on `galstreams` (2) Corresponding stream name (3) Number of RRab in the tails (t) and the progenitor (p) (4) Number of RRc in the tails (t) and the progenitor (p) (5) Number of expected contaminants in the tails (6) Stream vs. background RRL ratio in the on-stream region (7) Distance intrinsic dispersion (8) ϕ_1-proper motion intrinsic dispersion (9) ϕ_2-proper motion intrinsic dispersion (10) Reference of the track.

TrackName	StreamName	RR_{ab} t, p	RR_c t, p	$N_{\rm cont}$	$d_{\rm mean}$ (kpc)	f (kpc)	σ_d^{int} (mas/yr)	$\sigma_{\mu_{\phi_1}}^{int}$ (mas/yr)	$\sigma_{\mu_{\phi_2}}^{int}$ (*)	Ref.
AAU-ATLAS-L21	AAU-ATLAS	8, -	2, -	0.00	19.40 ± 0.33	0.319 ± 0.085	1.76 ± 0.20	0.056 ± 0.015	0.068 ± 0.012	(1)
AAU-AliqaUma-L21	AAU-AliqaUma	0, -	1, -	0.45	25.9 ± 1.9	0.221 ± 0.14	1.66 ± 0.31	0.095 ± 0.023	0.097 ± 0.025	(1)
ATLAS-I21	ATLAS	7, -	2, -	0.32	20.29 ± 0.36	0.266 ± 0.077	4.07 ± 0.48	0.205 ± 0.028	0.162 ± 0.026	(2)
Aquarius-W11	Aquarius	0, -	0, -	0.00	-	0.016 ± 0.022	4.1 ± 2.3	0.87 ± 0.73	0.87 ± 0.73	(3)
C-19-I21	C-19	0, -	0, -	0.00	-	0.010 ± 0.014	4.1 ± 2.3	0.20 ± 0.17	0.20 ± 0.18	(2)
C-7-I21	C-7	0, -	0, -	0.00	-	0.0020 ± 0.0030	0.25 ± 0.11	0.79 ± 0.06	0.736 ± 0.051	(2)
C-8-I21	C-8	0, -	0, -	0.00	-	0.16 ± 0.17	4.1 ± 2.3	0.38 ± 0.13	0.60 ± 0.18	(2)
Cetus-New-Y21	Cetus-New	2, -	2, -	0.00	16.60 ± 0.52	0.0030 ± 0.0020	4.30 ± 2.51	0.31 ± 0.19	0.17 ± 0.11	(5)
Cetus-Palca-T21	Cetus-Palca	52, -	25, -	12.67	30.17 ± 0.20	0.0310 ± 0.0060	1.60 ± 0.13	0.038 ± 0.012	0.148 ± 0.010	(6)
Chenab-S19	Chenab	2, -	0, -	1.22	40.1 ± 1.4	0.23 ± 0.13	2.56 ± 1.98	0.035 ± 0.020	0.039 ± 0.021	(4)
Elqui-S19	Elqui	8, -	2, -	0.75	48.28 ± 0.91	0.71 ± 0.18	4.18 ± 0.58	0.100 ± 0.037	0.104 ± 0.034	(4)
Fimbulthul-I21	Fimbulthul	2, 34	1, 45	2.32	4.86 ± 0.03	0.240 ± 0.025	0.497 ± 0.058	1.69 ± 0.13	0.504 ± 0.047	(2)
Fjorm-I21	Fjörm	0, 0	1, 0	0.51	5.31 ± 0.27	0.0010 ± 0.0010	0.885 ± 0.056	0.715 ± 0.045	0.478 ± 0.030	(2)
GD-1-I21	GD-1	5, -	0, -	1.69	8.69 ± 0.19	0.0151 ± 0.0083	0.610 ± 0.037	0.450 ± 0.012	0.338 ± 0.010	(2)
GD-1-PB18	GD-1	3, -	0, -	0.56	8.10 ± 0.20	0.021 ± 0.011	1.35 ± 1.44	0.33 ± 0.17	0.21 ± 0.14	(7)
Gaia-1-I21	Gaia-1	1, -	0, -	0.00	5.27 ± 0.26	0.097 ± 0.072	1.19 ± 2.08	0.595 ± 0.041	0.444 ± 0.038	(2)
Gaia-10-I21	Gaia-10	1, -	0, -	0.36	15.48 ± 0.77	0.039 ± 0.030	3.53 ± 1.93	0.32 ± 0.19	0.18 ± 0.15	(2)
Gaia-11-I21	Gaia-11	0, -	0, -	0.00	-	0.012 ± 0.018	3.91 ± 2.32	0.504 ± 0.075	0.496 ± 0.076	(2)
Gaia-12-I21	Gaia-12	1, -	0, -	0.00	11.88 ± 0.55	0.16 ± 0.11	1.78 ± 2.20	0.19 ± 0.20	0.20 ± 0.21	(2)
Gaia-6-I21	Gaia-6	1, -	1, -	0.00	8.58 ± 0.25	0.035 ± 0.022	0.71 ± 1.46	0.61 ± 0.30	0.22 ± 0.21	(2)
Gaia-7-I21	Gaia-7	0, -	0, -	0.36	-	0.29 ± 0.24	3.87 ± 2.34	0.76 ± 0.65	0.75 ± 0.65	(2)
Gaia-8-I21	Gaia-8	0, -	0, -	0.00	-	0.010 ± 0.013	4.08 ± 2.32	0.914 ± 0.081	0.424 ± 0.041	(2)
Gaia-9-I21	Gaia-9	0, -	0, -	0.00	-	0.017 ± 0.025	0.164 ± 0.082	0.197 ± 0.031	0.456 ± 0.055	(2)
Gjoll-I21	Gjöll	2, 0	0, 0	0.00	3.51 ± 0.13	0.043 ± 0.035	0.209 ± 0.041	1.013 ± 0.075	0.261 ± 0.023	(2)
Gunnthra-I21	Gunnthrá	0, -	0, -	0.00	-	0.012 ± 0.017	3.9 ± 2.3	0.776 ± 0.075	0.457 ± 0.052	(2)
Hrid-I21	Hrid	0, -	0, -	0.00	-	0.007 ± 0.010	0.320 ± 0.028	0.794 ± 0.040	0.498 ± 0.027	(2)
Indus-S19	Indus	3, -	1, -	0.36	14.98 ± 0.35	0.022 ± 0.020	4.10 ± 0.49	0.145 ± 0.030	0.109 ± 0.020	(4)
Jet-F22	Jet	1, -	1, -	0.52	27.1 ± 1.0	0.133 ± 0.087	4.3 ± 1.9	0.095 ± 0.019	0.064 ± 0.018	(8)
Jhelum-I21	Jhelum	3, -	2, -	1.05	11.40 ± 0.27	0.111 ± 0.050	0.35 ± 0.13	0.552 ± 0.038	0.489 ± 0.035	(2)
Jhelum-a-B19	Jhelum-a	3, -	0, -	1.09	11.57 ± 0.34	0.069 ± 0.054	2.4 ± 2.0	0.45 ± 0.22	0.38 ± 0.20	(9)
Jhelum-a-S19	Jhelum-a	2, -	1, -	0.00	12.49 ± 0.36	0.061 ± 0.033	1.00 ± 0.41	0.134 ± 0.027	0.190 ± 0.041	(4)
Jhelum-b-B19	Jhelum-b	4, -	2, -	0.00	11.77 ± 0.25	0.071 ± 0.031	1.51 ± 0.98	0.38 ± 0.14	0.39 ± 0.14	(9)
Jhelum-b-S19	Jhelum-b	2, -	1, -	0.00	10.86 ± 0.32	0.192 ± 0.092	2.20 ± 0.66	0.171 ± 0.039	0.150 ± 0.035	(4)
Kshir-I21	Kshir	0, -	0, -	0.00	-	0.072 ± 0.090	3.9 ± 2.3	0.326 ± 0.046	0.188 ± 0.034	(2)
Kwando-I21	Kwando	0, -	0, -	0.00	-	0.015 ± 0.021	0.30 ± 0.14	0.214 ± 0.036	0.166 ± 0.030	(2)
LMS1-M21	LMS1	13, -	11, -	6.03	17.48 ± 0.18	0.066 ± 0.016	2.88 ± 0.72	0.175 ± 0.046	0.183 ± 0.045	(10)
Leiptr-I21	Leiptr	2, -	0, -	0.33	9.97 ± 0.97	0.0070 ± 0.0090	0.914 ± 0.061	0.685 ± 0.035	0.420 ± 0.021	(2)
M2-G22	M2	2, 11	0, 6	0.88	10.40 ± 0.12	0.083 ± 0.019	1.34 ± 0.19	0.215 ± 0.036	0.163 ± 0.025	(11)
M2-I21	M2	1, 11	0, 6	1.78	10.90 ± 0.13	0.288 ± 0.056	0.81 ± 0.34	0.259 ± 0.068	0.290 ± 0.053	(2)
M3-Y23	M3	4, 97	0, 19	0.69	9.75 ± 0.04	0.531 ± 0.032	1.08 ± 0.08	0.192 ± 0.013	0.182 ± 0.012	(12)
M5-G19	M5	1, 49	0, 22	1.41	6.06 ± 0.04	0.493 ± 0.041	1.27 ± 0.12	0.299 ± 0.027	0.480 ± 0.033	(13)
M68-I21	M68	0, 0	0, 0	0.00	-	0.061 ± 0.077	0.59 ± 0.16	0.80 ± 0.13	0.375 ± 0.073	(2)
M68-P19	M68	1, 11	0, 22	0.72	9.43 ± 0.09	0.0442 ± 0.0081	2.68 ± 0.18	0.180 ± 0.019	0.258 ± 0.028	(14)
M92-I21	M92	8, 7	3, 1	5.36	8.00 ± 0.10	0.073 ± 0.022	1.01 ± 0.15	0.798 ± 0.064	0.755 ± 0.059	(2)
NGC1261-I21	NGC 1261	1, 1	0, 1	0.00	17.22 ± 0.53	0.015 ± 0.014	4.7 ± 2.2	0.23 ± 0.16	0.15 ± 0.13	(2)
NGC1851-I21	NGC 1851	4, 8	1, 5	0.67	11.99 ± 0.15	0.106 ± 0.027	0.21 ± 0.25	0.141 ± 0.044	0.153 ± 0.044	(2)
NGC2298-I21	NGC 2298	0, 1	0, 2	0.00	6.82 ± 0.24	0.161 ± 0.082	4.4 ± 1.6	0.17 ± 0.17	0.23 ± 0.16	(2)
NGC2808-I21	NGC 2808	0, 0	0, 0	0.33	8.94 ± 0.26	0.044 ± 0.031	2.7 ± 2.2	0.61 ± 0.39	0.55 ± 0.25	(2)
NGC288-I21	NGC 288	0, 1	0, 1	0.00	8.21 ± 0.31	0.115 ± 0.074	3.5 ± 2.2	0.40 ± 0.22	0.214 ± 0.210	(2)
NGC3201-I21	NGC 3201	0, 68	0, 5	0.34	4.42 ± 0.02	0.782 ± 0.043	0.59 ± 0.04	1.084 ± 0.043	0.510 ± 0.022	(2)
NGC3201-P21	NGC 3201	3, 68	0, 5	1.84	4.40 ± 0.02	0.414 ± 0.037	0.84 ± 0.06	0.996 ± 0.067	0.279 ± 0.016	(15)
NGC5466-I21	NGC 5466	1, 14	0, 6	0.33	13.70 ± 0.15	0.577 ± 0.080	1.70 ± 0.37	0.113 ± 0.022	0.097 ± 0.021	(2)
NGC5466-J21	NGC 5466	2, 14	0, 6	0.36	13.45 ± 0.15	0.119 ± 0.024	2.15 ± 0.22	0.106 ± 0.016	0.092 ± 0.015	(2)
NGC6101-I21	NGC 6101	0, 3	1, 10	0.00	12.07 ± 0.18	0.118 ± 0.029	3.07 ± 0.70	0.229 ± 0.047	0.079 ± 0.021	(2)
NGC6397-I21	NGC 6397	0, 0	0, 0	0.00	-	0.036 ± 0.049	3.9 ± 2.3	0.365 ± 0.017	0.608 ± 0.026	(2)
OmegaCen-I21	OmegaCen	4, 32	2, 45	3.60	4.80 ± 0.03	0.183 ± 0.020	0.903 ± 0.088	0.500 ± 0.045	0.421 ± 0.046	(2)
Ophiuchus-C20	Ophiuchus	1, -	0, -	0.00	5.92 ± 0.32	0.042 ± 0.059	1.79 ± 0.12	0.645 ± 0.043	0.505 ± 0.032	(16)
Orphan-I21	Orphan	24, -	10, -	1.30	17.99 ± 0.16	0.071 ± 0.013	2.26 ± 0.12	0.237 ± 0.013	0.288 ± 0.015	(2)
Orphan-K19	Orphan	4, -	2, -	1.88	19.83 ± 0.39	0.153 ± 0.084	4.7 ± 1.9	0.116 ± 0.077	0.14 ± 0.12	(17)
Orphan-K23	Orphan	86, -	29, -	9.25	24.11 ± 0.12	0.0792 ± 0.0081	1.91 ± 0.29	0.262 ± 0.024	0.104 ± 0.019	(18)

Continued on next page

Table 4.2: Continued

TrackName	StreamName	RR_{ab} t, p	RR_c t, p	$N_{\rm cont}$	$d_{\rm mean}$ (kpc)	f (kpc)	σ_d^{int} (mas/yr)	$\sigma_{\mu_{\phi_1}}^{int}$ (mas/yr)	$\sigma_{\mu_{\phi_2}}^{int}$ (*)	Ref.
Pal5-I21	Pal 5	15, 1	5, 5	0.51	18.86 ± 0.20	0.237 ± 0.047	2.41 ± 0.37	0.108 ± 0.044	0.031 ± 0.025	(2)
Pal5-PW19	Pal 5	15, 1	5, 5	1.67	19.56 ± 0.21	0.131 ± 0.027	1.06 ± 0.52	0.028 ± 0.022	0.032 ± 0.023	(19)
Phlegethon-I21	Phlegethon	2, -	1, -	0.00	3.45 ± 0.10	0.0140 ± 0.0091	0.5 ± 1.2	1.136 ± 0.042	0.395 ± 0.018	(2)
Slidr-I21	Slidr	0, -	0, -	0.00	-	0.017 ± 0.023	3.9 ± 2.3	0.835 ± 0.049	0.500 ± 0.029	(2)
Spectre-C22	Spectre	0, -	0, -	0.00	-	0.12 ± 0.14	3.9 ± 2.3	0.168 ± 0.062	0.083 ± 0.048	(20)
Svol-I21	Svöl	0, -	0, -	0.00	-	0.0050 ± 0.0070	0.331 ± 0.088	0.777 ± 0.052	0.584 ± 0.041	(2)
Sylgr-I21	Sylgr	0, -	1, -	0.00	2.49 ± 0.14	0.019 ± 0.016	2.1 ± 2.1	1.203 ± 0.070	0.407 ± 0.026	(2)
TucanaIII-S19	Tucana III	4, 0	2, 0	0.78	20.12 ± 0.39	0.37 ± 0.18	5.2 ± 1.9	0.067 ± 0.029	0.068 ± 0.028	(4)
Turranburra-S19	Turranburra	13, -	1, -	1.76	26.19 ± 0.35	0.59 ± 0.12	2.71 ± 0.49	0.151 ± 0.048	0.176 ± 0.028	(4)
Ylgr-I21	Ylgr	2, -	0, -	0.00	7.05 ± 0.23	0.0080 ± 0.0060	1.374 ± 0.054	0.691 ± 0.019	0.603 ± 0.018	(2)

(*) **References:** (1): Li et al. (2021), (2): I21, (3): Williams et al. (2011), (4): Shipp et al. (2019), (5): Yuan et al. (2022), (6): Thomas & Battaglia (2022), (7): Price-Whelan & Bonaca (2018), (8): Ferguson et al. (2022), (9): Bonaca et al. (2019a), (10): Malhan et al. (2021a), (11): Grillmair (2022), (12): Yang et al. (2023), (13): Grillmair (2019), (14): Palau & Miralda-Escudé (2019), (15): Palau & Miralda-Escudé (2021), (16): Caldwell et al. (2020), (17): Koposov et al. (2019), (18): Koposov et al. (2023), (19): Price-Whelan et al. (2019), (20): Chandra et al. (2022).

of the tidal radius at the pericenter). This means that there will be some differences in the number of RRL in and out of the cluster. However, unless the differences have a significant impact on the interpretation, they are not discussed.

4.2.1 Tucana III

Tucana III is an ultra-faint dwarf galaxy (UFD) and, in our sample, the only stream with a surviving associated progenitor that is not a globular cluster. This UFD has a luminosity of $L_{\rm UFD} \simeq 800 L_\odot$, a stellar mass of $M_{\rm UFD} \simeq 0.8 \times 10^3 M_\odot$ and a metallicity of [Fe/H]$= -2.42$ dex (Drlica-Wagner et al., 2015). The tracks used to study the stream are from Shipp et al. (2018), who estimated the initial stellar mass of the progenitor to be $M_{i,\rm prog} = 3.8 \times 10^3 M_\odot$ using the mass-metallicity relation from Kirby et al. (2013). However, it is worth noting that two dwarf galaxies in the Local Group, Leo IV and Andromeda X, have nearly the same metallicity as Tucana III ([Fe/H]$= -2.45$ dex and [Fe/H]$= -2.46$ dex, respectively); yet, their masses are significantly higher ($M \sim 10^4 M_\odot$ and $M \sim 10^5 M_\odot$, respectively), showing the large dispersion in this relation.

We found 6 RRL in the Tucana III stream (with an expected number of contaminants of 0.8) and none of them in the UFD itself, which is consistent with its low stellar mass. Three of the RRL have photometric metallicities measured by Li et al. (2023), with values of –1.96, –2.30, and –2.40 dex (uncertainties ~ 0.3 dex), all in agreement with the spectroscopic metallicity of the UFD. The stellar mass of the stream can be estimated from the number of RRL as follows: Combining the number of RRL in globular clusters from Cruz Reyes et al. (2024) with their stellar masses from Baumgardt & Hilker (2018) we get a production rate of one RRL per $1.39^{+4.25}_{-1.05} \times 10^4 M_\odot$; this implies that the stream's progenitor lost on the order of $2\text{–}34 \times 10^4 M_\odot$ of its mass and suggests that the UFD is about to be totally disrupted.

This value, although significantly larger than the estimate of Shipp et al. (2018), is consistent with those of Leo IV and Andromeda X. In addition, Riley et al. (2025), using the suite of Milky Way-mass halos from the Auriga project (Grand et al., 2017, 2024), found that departures from the intrinsic mass-metallicity relation are a sign of disruption. The logic is that if tidally disrupted dwarfs are (inadvertently) used in the calibration of the relation, then the mass will naturally be underestimated (because they have lost mass). Our lower bound for the mass of Tucana III is consistent with Riley et al. (2025)'s findings that using the Kirby et al. (2013)'s mass-metallicity relation underestimates the mass by ~ 0.34 dex, which corresponds roughly to a factor of ~ 2.2.

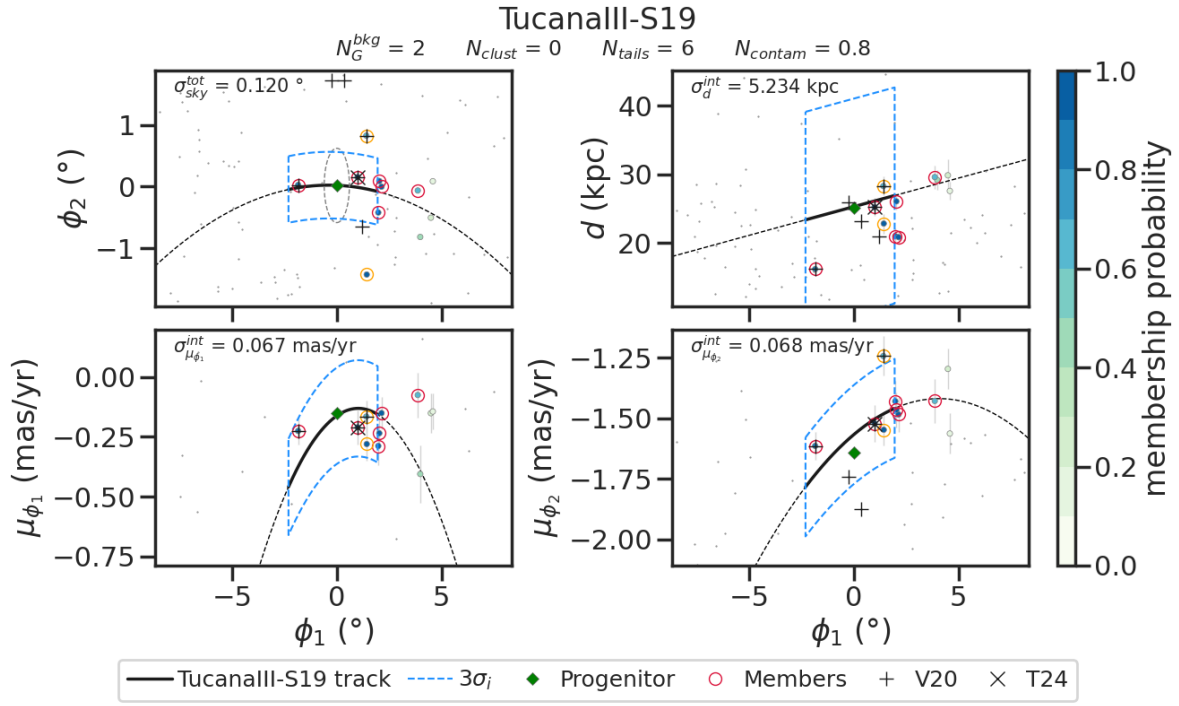

Figure 4.1: RRL stars in the vicinity of the Tucana III stream colored by membership probability with its tracks (solid black) and extrapolation (dashed black), RRL with membership probability < 0.1 are plotted with a small gray marker. **Upper left:** Sky position (in the stream coordinate frame) of the RRL. **Upper right:** Distances as a function of ϕ_1. **Lower panels:** Proper motions in ϕ_1 and ϕ_2 as a function of ϕ_1. The blue dashed regions shown 3σ to each side of the track, with σ equal to the observed width for the sky and to the intrinsic dispersions for the rest. In all panels, RRL with a membership probability higher than 50% and closer than $3\sigma_{sky}^{tot}$ in the sky are marked as red circles and are considered members of the stream, while if they are further than $3\sigma_{sky}^{tot}$ are marked as orange circles and are used to estimate the number of contaminants within the members, the black plus symbols are RRL detected by Vivas et al. (2020) and the black cross is the RRL detected by Tau et al. (2024). Additionally, we also show the number of Gaussians used for the background model, the number of RRL detected in the cluster and tails, and the number of expected contaminants.

In the literature, only two studies have searched for RRL around Tucana III (among other ultra-faint dwarf galaxies): Vivas et al. (2020) and Tau et al. (2024). Vivas et al. (2020) used the Gaia DR2 catalog of RRL (Clementini et al., 2019) to select all stars within a 2° radius centered on Tucana III and compared their proper motions with those of spectroscopically confirmed members of the UFD. Additional constraints were then applied based on the mean G-band magnitude of the RRL and their position on the color–magnitude diagram, equivalent to a distance requirement matching the dwarf's distance. Using this approach, they found no RRL within Tucana III, but identified six extra-tidal candidates, shown in Fig. 4.1 as black plus symbols (all of them belong to our sample as well). However, as noted in their study, these stars do not appear to follow the tails of the stream but are instead distributed around the UFD. Tau et al. (2024) searched for extended stellar populations in UFDs following Vivas et al. (2020), but they enhanced it by using the RRL catalogs from Gaia DR3, Zwicky Transient Facility (ZTF; Huang & Koposov, 2022), Dark Energy Survey (DES; Stringer et al., 2021), and PS1. They applied selection criteria based on angular separation (within 15 times the half-light radius; $r < 1.275°$ for Tucana III), Gaia G-band magnitude (within $m_G \pm 0.5$ mag relative to the UFD), and proper motion (within a box defined by confirmed members). Applying these criteria, they identified one RRL on the outskirts of Tucana III — one of the same stars previously reported by Vivas et al. (2020) — which is shown as a black cross in Fig. 4.1.

Both studies based their methods on the argument that the population of RR Lyrae stars in the Milky Way declines with Galactocentric radius, becoming very rare beyond ∼50 kpc (e.g. Zinn et al., 2014; Medina et al., 2018; Stringer et al., 2021). Since most UFD lie at greater distances, contamination from the halo field stars can generally be neglected. However, Tucana III is located at a Galactocentric distance of only ∼23 kpc; therefore, this argument becomes less strong and a more rigorous method, like that used in this work, would provide a more robust association to the dwarf and the stellar stream.

We recovered three of the RRL identified by Vivas et al. (2020) with a membership probability greater than 50%. Of these, two are classified as members — one of which is also the one reported by Tau et al. (2024) — while the third is not, as it lies significantly far from the celestial track. Our model allows us to assess the reliability of detected members through their membership probabilities, which exceed 90% for the two confirmed RRL in common. In contrast, the remaining three RRL candidates from Vivas et al. (2020) have membership probabilities below 10%. As shown in Fig. 4.1, not only are these stars spatially distant from the track on the sky, but they also have proper motions in ϕ_1 that fall outside the range displayed in the figure. This is not surprising, as Vivas et al. (2020) had already noted that their candidates do not appear to follow the stream.

In summary, we have identified 6 RRL, 2 of which were previously reported as extra-tidal by Vivas et al. (2020) and Tau et al. (2024). Of the remaining 4 RRL previously identified by Vivas et al. (2020), 3 have membership probabilities $p_{\rm memb} < 0.5$ and are therefore rejected as members by our model. The fourth has a $p_{\rm memb} > 0.5$, but lies at $7.2\sigma^{\rm tot}_{\rm sky}$ from the celestial track, exceeding our sky selection box and is therefore, also not reported here as a member. Finally, of the 4 new detections, 2 have photometric metallicity, both consistent with the spectroscopic metallicity of the UFD, as mentioned above, making their classification as members even more trustworthy. In addition, all are in the extrapolation of the trailing arm of the stream, extending its length up to $\sim 2^\circ$.

4.2.2 M92

M92 (NGC 6341) is a metal-poor globular cluster ([Fe/H]$=-2.35$ dex, Carretta et al., 2009) located at a heliocentric distance of 8.5 kpc and is currently near its apocenter ($R_{\rm gal}$ = 9.85 kpc, $R_{\rm peri}$ =1.25 kpc, $R_{\rm apo}$ =10.62 kpc, Baumgardt & Vasiliev, 2021). Several tracks have been reported in the literature for the M92 stream (Sollima 2020; Thomas et al. 2020, T20 hereafter; I21; Ibata et al. 2024); however, only the track presented by I21 includes proper motion and distance measurements and is, therefore, the one adopted in this work. Figure 4.2 shows the results of the census using the I21 track. We identified 8 RRL within the cluster (compared to the 17 reported by Cruz Reyes et al. 2024, who did not impose RUWE quality constraints) and 11 candidates along the tidal tails of the M92 stream. We estimate that 5.4 of the latter are likely field contaminants.

In previous studies, Kundu et al. (2019) and Abbas et al. (2021) identified 1 extra-tidal RRL nearby M92, which we recover as part of the cluster[1], as shown in the left panel of Fig. 4.3. Hanke et al. (2020) and Xu et al. (2024) searched for escapee stars; however, none of their candidates are RRL. In both cases, their candidates appear to follow the sky track presented by T20 and Sollima (2020), instead of the one from I21, as shown in the left panel of Fig. 4.3.

In the right panel of Fig. 4.3, we show the Amplitude–Period diagram for the RRL that we have identified as members of the stream. A clear bimodality appears between the RRab stars within the cluster (circles) and those in the tails (star symbols), where the former show longer periods than the latter. This segregation could be explained by two possible factors: *i)* at constant metallicity, more evolved RRL leave the zero-age horizontal branch, increasing their luminosity and therefore their period; *ii)* at constant age, a metallicity gradient exists, where more metal-rich stars have shorter periods.

[1]They used a tidal radius of r_t = 30.5 pc (Moreno et al., 2014). However, using a larger tidal radius of r_t = 113 pc (which takes into account the eccentricity of the orbit and the orbital phase of the cluster, Eq. 8 of Webb et al. (2013)), that same star would be considered bound to the cluster.

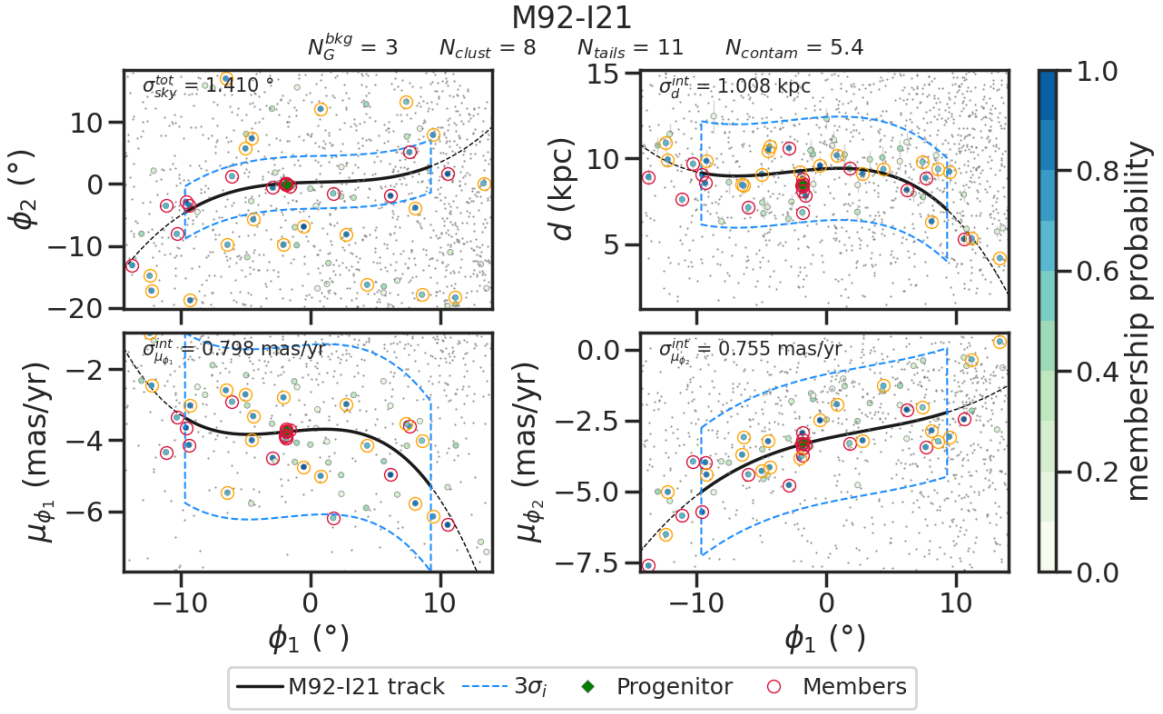

Figure 4.2: Similar to Fig. 4.1 but for the M92 stream.

In this case, the RRL in the tails lie in a higher metallicity locus of the diagram (-1.6 ± 0.1 dex), consistent with their photometric metallicities from Li et al. (2023, determined from the ϕ_{31} Fourier parameter); meanwhile, the RRL in the cluster lie in a more metal-poor locus (-2.2 ± 0.1 dex), consistent with both their photometric metallicities and the spectroscopic metallicity of M92 (-2.35 ± 0.05 dex, Carretta et al., 2009). This coincidence, along with the fact that we expect all the stars in a globular cluster to have roughly the same age, supports the second explanation presented, and thus a clear segregation with a difference in metallicity of ~ 0.6 dex between the tails and the cluster.

Since the metallicities of the RRL in the tails are consistent with the mean metallicity of the halo background (~ -1.2 dex), the question of whether these are genuine stream members or simply field contaminants (stars with proper motions and distances consistent with the stream but not physically associated with it) arises. To assess this possibility, we performed a control experiment using stars within the same box sample but located outside the on-stream and off-stream regions. This analysis yielded zero expected halo contaminants, suggesting that the 11 RRL identified in the stream region represent a significant overdensity with respect to the halo background.

On one hand, the metallicity dispersion obtained considering both the cluster and tail populations is too large (~ 0.6 dex) to have originated from a single globular cluster. On the other hand, the observed segregation implies a metallicity gradient that increases outward, opposite to what is typically seen in most of the dwarf galaxies in the Local Group (Pilkington et al., 2012). However, dwarf galaxies in the Centaurus group have been observed to have nuclei dominated by a Nuclear Star Cluster that is much more metal-poor than the rest of the galaxy and has a roughly simple star formation history (Fahrion et al., 2020). If this were the case for M92, it could represent the remnant Nuclear Star Cluster of a now-disrupted dwarf galaxy, with the stream tracing the *galaxy's tidal debris* (similar to the case of the M54 globular cluster and the Sagittarius stream, although M54 presents a metallicity spread). In addition, the high metallicity of the tails (∼-1.6 dex) implies a progenitor stellar mass of $\sim 2 \times 10^6\ M_\odot$, based on the mass-metallicity relation from Kirby et al. (2013). This in-

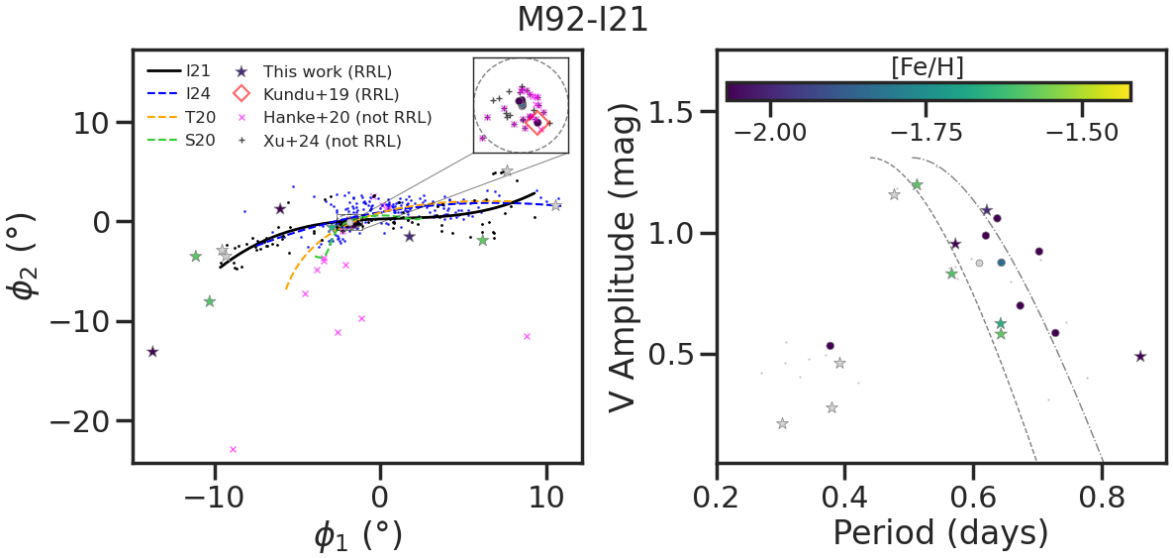

Figure 4.3: Left: Sky position (in the stream coordinate frame) of the vicinity of the M92 stream. The circles and star symbols are the RRL members identified by us colored by the photometric metallicity from Li et al. (2023), the red empty diamond is the RRL identified by Kundu et al. (2019) and recovered by Abbas et al. (2021), the pink crosses and gray plus symbols are the members from Hanke et al. (2020) and Xu et al. (2024) respectively (in both cases these are not RRL). We also show the different tracks reported in the literature with its members for each case if available: green by Sollima (2020), orange by T20, black by I21 (the one used for this work), and blue by Ibata et al. (2024). **Right:** Amplitude vs. Period diagram of the RRL members that we identified in the vicinity of the M92 stream colored by its photometric metallicity. In both panels the star symbols are the RRL associated to the tails and the circles are the RRL associated to the globular cluster.

ferred mass places the progenitor within the dwarf galaxy regime rather than that of a globular cluster.

T20 proposed a similar scenario with a key difference: M92 was accreted with its host dwarf galaxy; however, the tidal debris was produced by the *cluster itself*, and the host galaxy is now totally phase-mixed or in a completely different orbit. The authors proposed this origin history to explain the discrepancy between the dynamical age of the stream ($\sim$ 500 Myr according to them) and the stellar age of the cluster (between 11.0 and 13.80 Gyr, depending on the study, Ying et al., 2023). The two scenarios are not necessarily contradictory. Since the track proposed by T20 is not the same as that proposed by I21, T20's track might be tracing the cluster's tidal tails, while I21's might trace the galaxy's tidal tails. Similar interpretations have been proposed for other stellar streams (e.g., Jhelum, Bonaca et al. 2019a; LMS-1, Yuan et al. 2020; GD-1, Cetus-Palca, Thomas & Battaglia 2022; Valluri et al. 2025; C-19, Yuan et al. 2025). However, to confirm this hypothesis, more information is needed; in particular, the T20 proper motion tracks, which currently do not exist.

Additionally, the intrinsic proper motion dispersions result in $\sigma^{int}_{\mu_{\phi_1}} = 0.798$ mas/yr and $\sigma^{int}_{\mu_{\phi_2}} = 0.755$ mas/yr, which, at the distance of M92 (8.5 kpc), correspond to an intrinsic tangential velocity dispersion of $\sigma^{int}_{vt_{\phi_1}} = 32.13$ km/s and $\sigma^{int}_{vt_{\phi_2}} = 30.41$ km/s. These values are significantly larger than both the internal velocity dispersion of the cluster ($\sim$6.5 km/s, Baumgardt & Hilker, 2018) and the typical velocity dispersion of globular cluster streams (usually less than 5 km/s, Li et al., 2022). To check this, we performed two tests: *i)* Running our model while fixing the intrinsic velocity dispersion to match that of the M92 cluster; *ii)* Running a more conservative prior based on the stream velocity dispersion distribution from Li et al. (2022, same as Eq. 3.3 but with $\alpha = 1.28427$ and $\beta = 0.15706$), which allows high dispersions but favors smaller values. In both cases, no RRL were identified as stream members. We then repeated the experiments including the 84 confirmed stream members from

I21 in our RRL sample. Under the fixed-dispersion model, we recovered less than 35% of them. In contrast, when using the conservative prior, the intrinsic velocity dispersion converged to the one given by the I21 members (∼30 km/s, consistent with our findings), and we recovered ∼90% of their members as well as all the RRL that we had originally identified. These results indicate that the data from I21 require a large intrinsic velocity dispersion. Moreover, the low number of candidate RRL members prevents the inference from converging on this dispersion on its own, but this does not imply that these RRL are contaminants, as already addressed through our control experiments outside the on-stream and off-stream regions.

It is important to note that the intrinsic dispersion we measured is accurate only if the uncertainties of the observations are correctly estimated. There are a few ways this assumption could fail. On one hand, the proper motion errors might be underestimated. However, for this to really account for the observed dispersion, the errors would have to be significantly larger than the reported, an unlikely scenario given the precision of Gaia data. On the other hand, there could be a real gradient in distance and/or tangential velocity that is steeper than the one modeled on the stream tracks, which would translate as a large apparent dispersion in proper motion. To get a better handle on this, a more numerous tracer than RRL would be needed for which reasonably accurate distances could be measured. However, if the intrinsic dispersion obtained truly reflects the internal velocity dispersion of the stream, such a high value would imply a large mass, inconsistent with a globular cluster origin. This points to the same conclusions drawn from the metallicity measurements via the mass–metallicity relation, further supporting our scenario in which the stream we detect is the remnant of a disrupted dwarf galaxy that once hosted M92.

4.2.3 NGC 3201-Gjöll

NGC 3201 is a globular cluster with a mass of $1.93 \times 10^5\ M_\odot$ (Baumgardt & Hilker, 2018), a metallicity of -1.51 dex (Carretta et al., 2009), and a total of 87 RRL according to Cruz Reyes et al. (2024). For its associated stream, three tracks are available in `galstreams`: Two short segments reported by I21, one centered around the cluster with an extent of $\sim 10^\circ$ and another, part of the trailing arm and originally detected as Gjöll by Ibata et al. (2019b), with an extent of $\sim 60^\circ$ (later I21 recognized that Gjöll is the tidal debris of NGC 3201). The third more extended track ($\sim 140^\circ$) was reported by Palau & Miralda-Escudé (2021) and encompasses both segments of I21. All the tracks are in good agreement in sky, distance, and proper motion. It is worth noting that NGC 3201 has recently crossed the Galactic disk ($b = 8.74^\circ$). Therefore, there is a part of the stream embedded in the disk that is very difficult to separate from it; this is why we exclude the RRL in this region, as shown by the gray dashed lines in the top-left panel of Fig. 4.4.

We identified 3 RRL in the tails and 73 in the cluster (Fig. 4.4). The difference in the number of cluster RRL with respect to the 87 identified by Cruz Reyes et al. (2024) arises from the 12 RRL with RUWE 1.4 that we do not count, and the two additional RRL that are not in our catalog (one detected by them and the other detected by Clement (2017)). Using the previously mentioned (Sec. 4.2.1) RRL production rate (one RRL per $1.39^{+4.25}_{-1.05} \times 10^4 M_\odot$), we estimate the stellar mass of the cluster to be between $2.6 \times 10^5 M_\odot$ and $4.9 \times 10^6 M_\odot$; the lower end of this distribution is consistent with the mass reported by (Baumgardt & Hilker, 2018).

Kundu et al. (2019) already had searched for extra-tidal RRL nearby NGC 3201, identifying the 13 shown in Fig. 4.5 as black crosses. Using the tidal radius adopted in this work (82.34 pc) instead of the one they used (36.13 pc, Moreno et al., 2014), we consider all these stars to still be within the cluster. However, they appear to be in a more elongated structure with respect to the rest of the RRL of the cluster, suggesting that they are going to be the next totally unbounded RRL from NGC 3201. The ratio of RRL type *ab* (RRab) to *c* (RRc) of these stars, 12 RRab to 1 RRc, is consistent with the rest of the RRL in the cluster (56 RRab to 4 RRc). Their photometric metallicities are also consistent with those of the cluster (Fig. 4.5) and with its spectroscopic metallicity. The only peculiarity is their

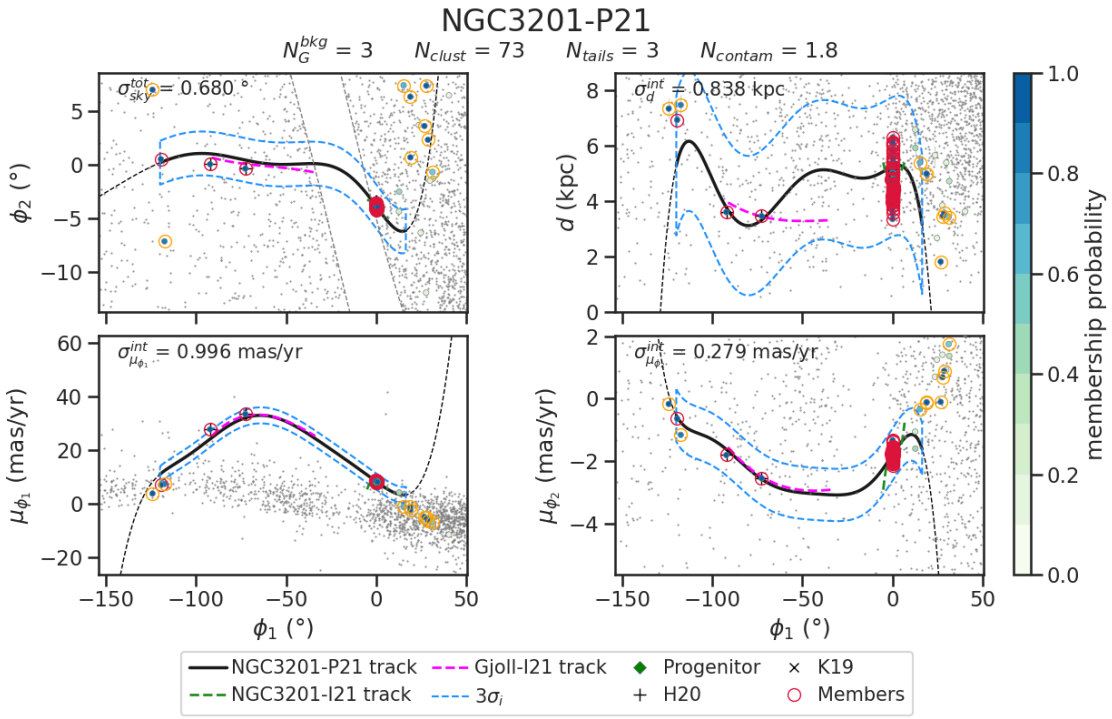

Figure 4.4: Similar to Fig. 4.1 but for the NGC 3201 stream. The black crosses are the 'extra-tidal' RRL identified by Kundu et al. (2019) and the black plus symbols are the RRL identified by Hansen et al. (2020). The black solid lines are the tracks reported by Palau & Miralda-Escudé (2021), and the magenta (Gjöll segment) and green (NGC 3201 segment) dashed lines are the tracks reported by I21.

asymmetrical spatial distribution, with 4 in the direction of the leading arm and 9 in the direction of the trailing arm. This asymmetry was also observed by Kundu et al. (2019), who attributed it to the combined effects of tidal disruption with stripped debris from NGC 3201.

Hansen et al. (2020) chemo-dynamically linked the NGC 3201 cluster with the Gjöll stream, and identified 2 RRL as stream members in the process. These are shown in Fig. 4.3 as black plus symbols and correspond to 2 of the 3 RRL that we identified as members of the tails. All 3 RRL are located at the end of the detected trailing arm. The absence of RRL closer to the cluster is not surprising because of the presence of the Galactic disk. However, given the elongated structure on the outskirts of the cluster, one might expect to find RRL in this region as well. With respect to the mass of the stream, using the lower end of the RRL production rate distribution to be consistent with the cluster, we estimate a minimum stellar mass of $1.02 \times 10^4 M_\odot$ for the trailing arm.

In summary, we identify a new RRL member in the trailing arm of the stream, with a membership probability of $p_{\rm memb} = 0.992$. The identified RRL members do not show any segregation in type or metallicity, apart from the asymmetrical distribution in the elongated structure on the outskirts of NGC 3201.

4.2.4 Palomar 5

Palomar 5 (Pal 5) was the first stellar stream associated with a globular cluster to be discovered (Odenkirchen et al., 2001; Rockosi et al., 2002), with an originally detected extent of 10°. Subsequent observations have extended this length to approximately 30° (Starkman et al., 2020). The globular cluster itself has a mass of $1.39 \times 10^4 M_\odot$ (Baumgardt & Hilker, 2018) and is located at 21.94 kpc

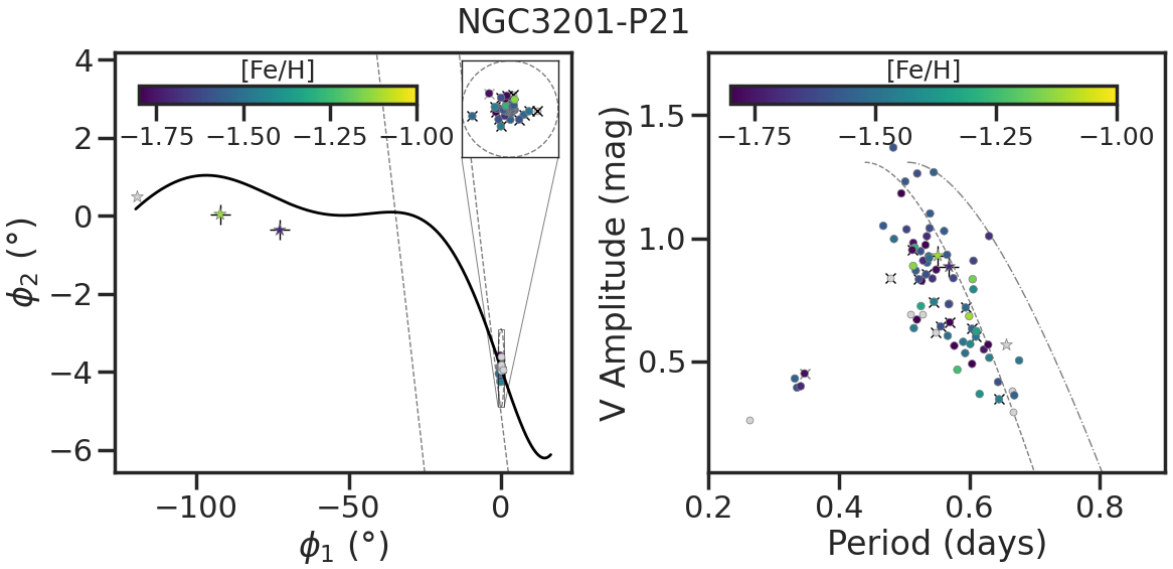

Figure 4.5: Similar to Fig. 4.3 but for the NGC 3201 stream

from the Sun (Baumgardt & Vasiliev, 2021). The total observed mass of the system, including the cluster and its tidal tails, has been estimated at $1.2 \times 10^5 M_\odot$ (Ibata et al., 2017), which means that the majority of the mass is concentrated in the tails.

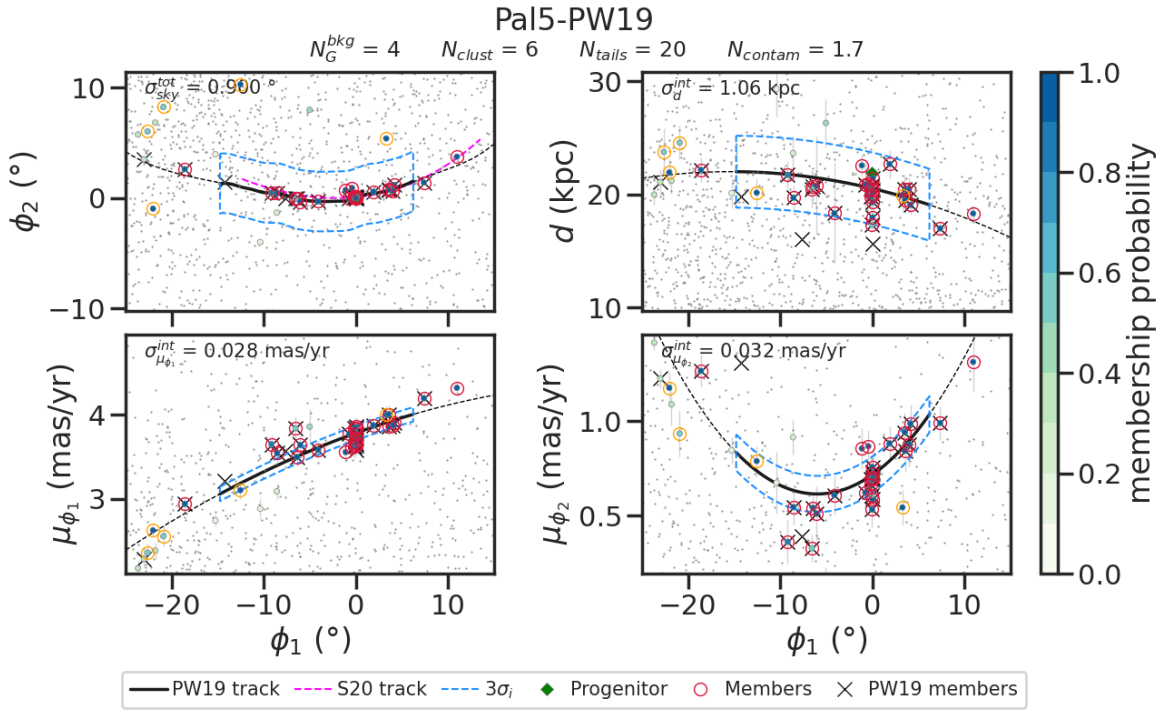

Figure 4.6: Similar to Fig. 4.1 but for the Pal 5 stream. The black crosses are the RRL members identified by Price-Whelan et al. (2019). The magenta dashed line in the upper left panel correspond to the Pal 5 track from Starkman et al. (2020).

This stream has two tracks with 5D information available in `galstreams`: One reported by I21 and the other by Price-Whelan et al. (2019). The latter is one of the few studies characterizing a stellar stream with RRL. Using Gaia DR2 data, they identified 10 RRL within the tidal radius of the cluster (11′ according to them) and almost twice as many (17) located in the tails. Furthermore, they observed a segregation in the RRL population of the system: While most of the RRc (8 out of 12) are in the cluster, most of the RRab (13 out of 15) are in the tails.

Adopting a tidal radius of 49.73 pc (corresponding to 7.8′ at the distance adopted), we identified 6 RRL in the cluster and 20 in the tidal tails (expecting 1.7 of them to be contaminants) based on the track from Price-Whelan et al. (2019), as shown in Fig. 4.6. We recover the strong segregation by RRL type previously reported by Price-Whelan et al. (2019): 5 out of the 6 RRL of the cluster are RRc, while 15 out of the 20 RRL of the tails are RRab.

Of the RRL of the cluster, we were able to recover all except one of those identified by Price-Whelan et al. (2019)[2] (and Cruz Reyes et al., 2024). The missing star is the furthest from the cluster in terms of distance (Fig. 4.6); however, this is due to the slightly richer metallicity assigned from the halo metallicity distribution (see Sec. 2). Of the RRL of the tails, we recover most of the RRL identified by Price-Whelan et al. (2019), except for 3 in the trailing arm, which, due to the updated value of their distances, are now less consistent with the track. Furthermore, we identified 3 new RRL: 2 located near the cluster in the trailing arm, and 1 in the extended track of the leading arm. The latter RRL is consistent with the track identified by Starkman et al. (2020), providing new distance and proper motion information for that segment of the stream, which previously only had positional information.

4.2.5 NGC 1851

NGC 1851 is a relatively massive globular cluster, with a stellar mass of $M = 2.83 \times 10^5\ M_\odot$ (Baumgardt & Hilker, 2018), located at a heliocentric distance of 11.95 kpc (Baumgardt & Vasiliev, 2021). Several studies have reported the presence of an extended halo up to ∼250 pc from the cluster (Olszewski et al., 2009; Carballo-Bello et al., 2014, 2018; Kuzma et al., 2018), well beyond its tidal radius of 123.89 pc. More recently, using data from the Dark Energy Survey and Gaia EDR3, Shipp et al. (2018) and I21, respectively, identified a diffuse ∼ 8° long tidal tail around the cluster.

The tracks identified by I21 show an offset with respect to the cluster in distance and proper motion ($\Delta d = -1.8$ kpc, $\Delta\mu_{\phi_1} = -0.12$ mas/yr, and $\Delta\mu_{\phi_2} = 0.18$ mas/yr; see Fig. 4.7). We therefore apply a manual correction to make them match with the cluster before applying our method. We identified 13 RRL in the cluster and 5 in the tails (expecting 0.7 of them to be contaminants); 2 out of the 5 tail members are new detections. Regarding the cluster members, we recovered all but one of the RRL with RUWE < 1.4 (28 in total, Cruz Reyes et al., 2024).

Abbas et al. (2021) previously searched for extra-tidal RRL in the vicinity of NGC 1851, visually classifying 5 stars as candidate members of the cluster: 2 with high confidence and 3 with intermediate confidence. As shown in Fig. 4.7, we confirmed the 2 high-confidence RRL candidates located closer to the cluster, as well as 2 of the 3 intermediate-confidence ones. The one that we do not identify is due to its proper motion not being consistent with the stream. The other two also have a lower membership probability in our model ($p_{\rm memb}$ = 0.654 and 0.584) compared to the rest of the identified members, which have $p_{\rm memb} > 0.88$. Furthermore, one of them (Gaia DR3 4822412580148688896) has a photometric metallicity of [Fe/H]=−2.53 ± 0.30 dex (Li et al., 2023), which is much more metal-poor than both the rest of the members ($\overline{\rm [Fe/H]} = -1.59 \pm 0.17$ dex) and the spectroscopic metallicity of the NGC 1851 cluster (−1.18±0.08 dex, Carretta et al., 2009), suggesting that this RRL might be a contaminant.

[2]The other 3 RRL that Price-Whelan et al. (2019) consider from the cluster are part of the tidal tails under our criteria.

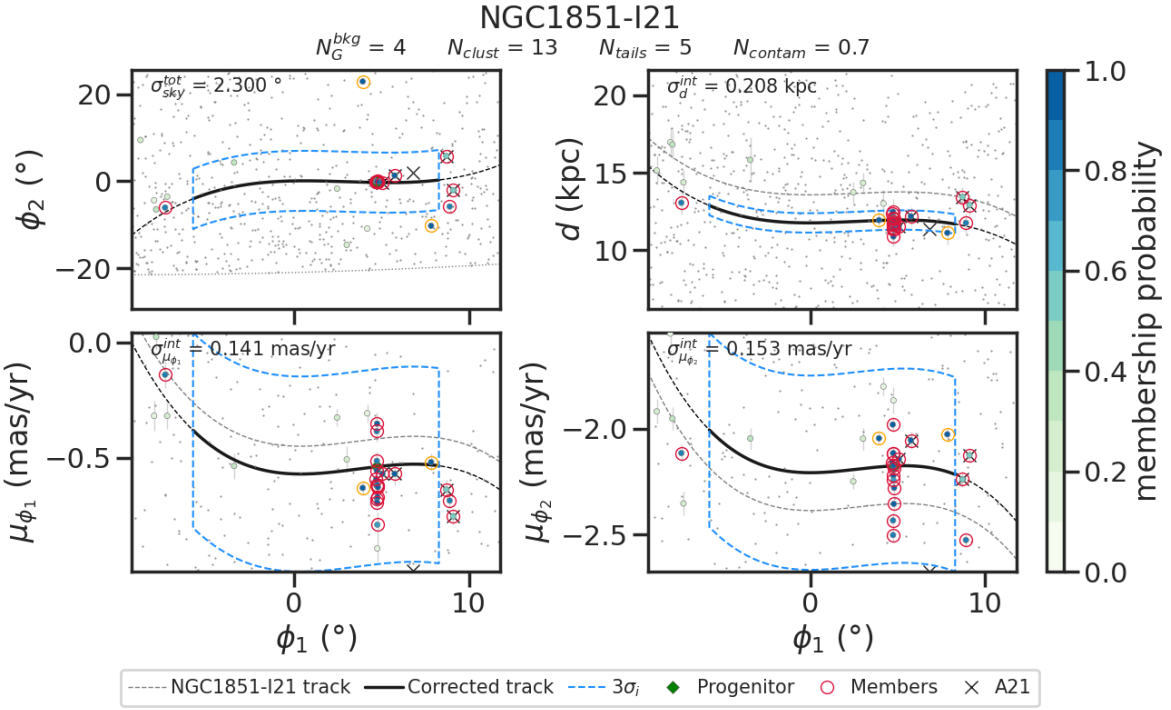

Figure 4.7: Similar to Fig. 4.1 but for the NGC 1851 stream. The black crosses are the RRL candidates identified by Abbas et al. (2021). The gray dashed lines are the original tracks (without correction) from I21.

In order to assess whether correcting the tracks to match the cluster distance and proper motion was justified, we performed a control experiment. We first ran our method using the original (uncorrected) tracks on stars in the on-stream region (as usual), and second on stars within the same box sample (sky window plus distance limits) but located outside both the on-stream and off-stream regions (since this was used for the background model). In the first case, we identified 12 RRL in the tails; however, in the second case, we identified between 3 and 6, indicating a statistical overdensity of halo RRL consistent with the distance and proper motion of the uncorrected tracks, but which are not actual stream members. When we repeat the same experiment using the corrected tracks, the expected number of halo RRL is consistent with zero, confirming that our decision was appropriate. More importantly, this highlights that the method is very sensitive to the choice of tracks, and a reason to, in a next stage of this work, perform this analysis blindly (i.e., without assuming tracks) in the cases with enough RRL members (as in the case of Pal 5, Price-Whelan et al., 2019).

4.2.6 ωCentauri-Fimbulthul

ωCentauri (ωCen; NGC 5139), located at a heliocentric distance of 5.43 kpc (Baumgardt & Vasiliev, 2021), is the most massive globular cluster in the Milky Way (3.94×10^6 $M_\odot$, Baumgardt & Hilker, 2018). It presents several peculiar features, including distinct multiple stellar populations with a wide range of ages and metallicities (Johnson & Pilachowski, 2010), as well as different kinematics correlated with chemical abundances (Bellini et al., 2018). These characteristics have led to the hypothesis that ωCen is the remnant core of a dwarf galaxy accreted by the Milky Way (Majewski et al., 2000). Its tidal tails were first detected in Gaia DR2 data by Ibata et al. (2019b), who named them the Fimbulthul stream, and were afterward associated with the cluster as its trailing arm (Ibata et al., 2019a). A more extended and slightly different track was later reported using Gaia EDR3 by I21; this is the version adopted as default in `galstreams` and analyzed in this work. The relatively low Galactic latitude of ωCen ($b = 14.98°$) makes it difficult to identify its leading arm due to the pres-

ence of the disk; nonetheless, Ibata et al. (2024) reported a candidate segment, designated Stream #55.

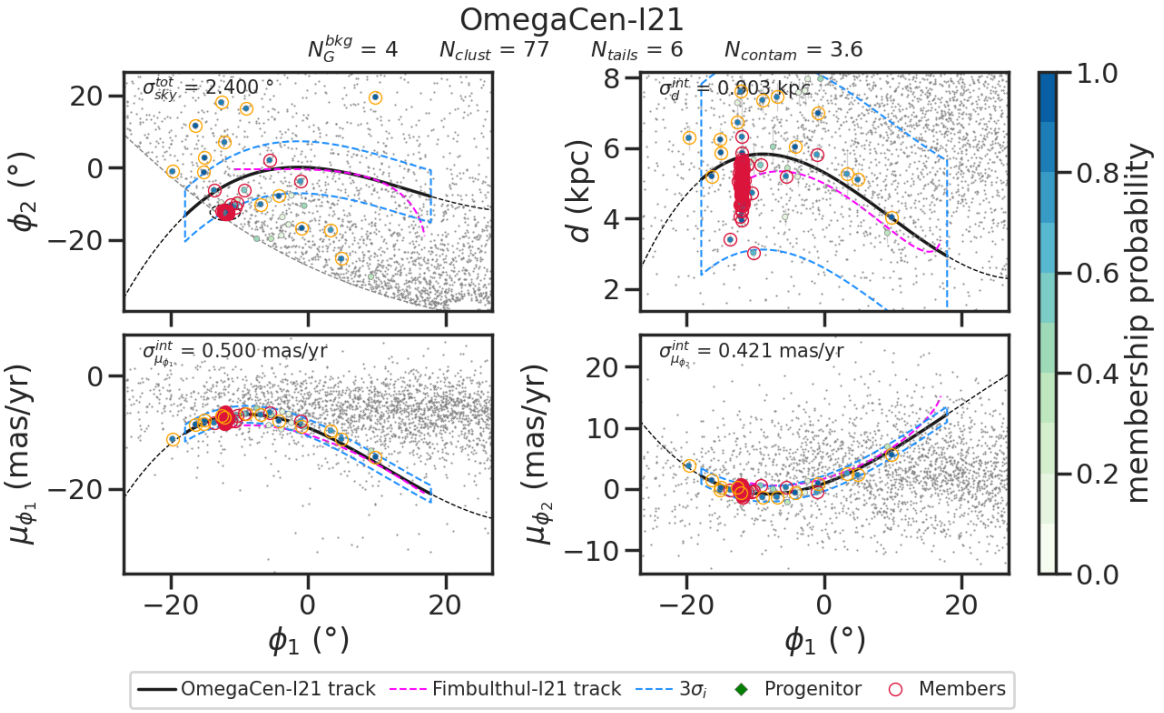

Figure 4.8: Similar to Fig. 4.1 but for the ωCen stream. The magenta dashed line correspond to the Fimbulthul track reported by Ibata et al. (2019b). The lack of RRL in the lower left of the first panel is due to the presence of the disk that we removed from the sample to avoid further contamination.

It is important to note that while both tracks are connected to the cluster in proper motion and distance, they are not spatially connected to it (Fig. 4.8). This suggests that the results using these tracks must be taken with caution, and highlights again the importance of performing this analysis blindly when the number of RRL members allows it.

We recovered 77 out of the 84 RRL present in our catalog with RUWE<1.4 in the cluster (Cruz Reyes et al., 2024) and identified 6 RRL in the tail debris, all of which are new detections; however, we expect 3.6 of them to be contaminants (Fig. 4.8). Among the 77 RRL in the cluster, 29 have photometric metallicity available from Li et al. (2023). We fitted a 1D Gaussian mixture model to their metallicity distribution using three components, according to the BIC fitting. There are two populations centered at -2.11 and -1.50 dex, the former being the dominant one. The third component contains a single star (Gaia DR3 6083704592196499328) with [Fe/H]$=-2.87 \pm 2.21$ dex; such a large error means that its photometric metallicity is extremely unreliable. The two populations correspond to the two groups of RRab visible in the right panel of Fig. 4.9. They are consistent with two of the four stellar populations identified by Kuzma & Ishigaki (2025) within a radial distance of 15′ from the cluster center, which show peaks at -2.11, -1.83, -1.50, and -1.19 dex (the middle two being the most dominant).

Out of the 6 RRL identified in the tails, 3 have photometric metallicity: 2 are consistent with the more metal-rich population ([Fe/H]$=-1.60\pm0.29$ and -1.41 ± 0.32 dex), while the third ([Fe/H]$=-1.90\pm$ 0.28 dex) is consistent with the more metal-poor population; this behavior is also appreciated in the right panel of Fig. 4.9. We find no sign of spatial, type, or metallicity segregation within the cluster or the tails, although the number of RRL in the tails is too small to draw robust conclusions. Further-

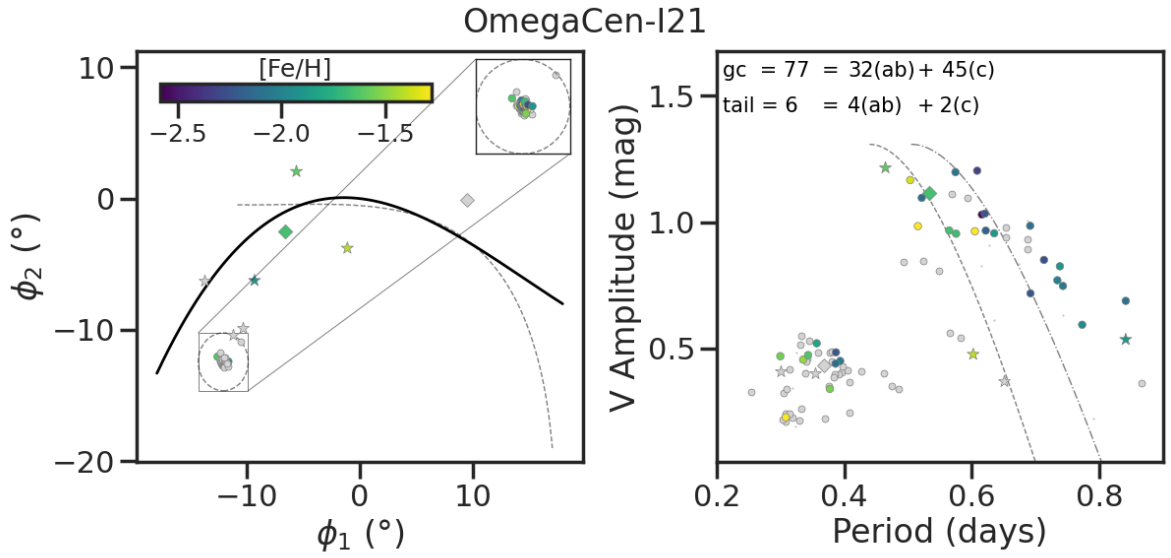

Figure 4.9: Similar to Fig. 4.3 but for the ωCen stream. The diamond symbols correspond to the two additional RRL identified with the Fimbulthul track (gray dashed line of left panel) from Ibata et al. (2019b).

more, using the track from Ibata et al. (2019b), we identified two additional RRL members in the tails (diamond symbols in Fig. 4.9); one of them has a photometric metallicity of [Fe/H]$=-1.66\pm0.67$ dex, which is also more consistent with the more metal-rich population.

In summary, within the cluster, the RRL stars are grouped into two populations with different metallicities ([Fe/H] = –2.11 and –1.50 dex). We identified 6 (+2) RRL stars in the tidal tails, whose photometric metallicities and positions in the period–amplitude diagram suggest they also belong to the same populations found within the cluster, with the more metal-rich population being dominant (opposite to what happens within the cluster). This is the first time RRL stars have been detected in the ωCen stream and associated with its distinct stellar populations. However, it is important to note that this analysis was made using tracks whose celestial components do not directly connect to the cluster, illustrating one more reason to perform this analysis blindly when possible.

4.2.7 M68-Fjörm

M68 (NGC 4950) is a metal-poor globular cluster ([Fe/H] =–2.27 dex, Carretta et al., 2009) with a mass of 1.23×10^5 $M_\odot$ (Baumgardt & Hilker, 2018), located at 10.4 kpc from the Sun (Baumgardt & Vasiliev, 2021). Its long stream, although barely detected close to the cluster (Sollima, 2020), was first detected by Ibata et al. (2019b) as the Fjörm stream and later associated with M68 by Palau & Miralda-Escudé (2019) based on their orbital properties.

There are three 5D tracks available on `galstreams` for this stream: M68-P19 (default, Palau & Miralda-Escudé, 2019), Fjorm-I21 and M68-I21 (I21). However, the latter track has several discrepancies with the M68 cluster and the other two tracks; therefore, it is not taken as a track for this stream (as suggested by Mateu, 2023), but for a completely different stream without a progenitor associated. The other two tracks are in disagreement with the cluster's distance and between them at $\phi_1 \lesssim 30°$, with I21 predicting a shorter distance than Palau & Miralda-Escudé (2019), as shown in the fifth row of Fig. 11 from Mateu (2023).

Using the default track (Palau & Miralda-Escudé, 2019), with or without applying a distance correction to align it with the cluster, we identified all 33 RRL within the tidal radius that have RUWE<1.4

(Cruz Reyes et al., 2024) and only a single RRL in the tails. This is another case, like with NGC 3201 and ωCen, where we observe a significant amount of RRL in the progenitor and only a handful in its tidal tails; given the mass segregation that occur in globular clusters this result is not unexpected (see discussion in Sec. 5.2).

4.2.8 M3-Svöl

M3 (NGC 5272) is a globular cluster located at 10.18 kpc from the Sun and 12.09 kpc from the Galactic center (Baumgardt & Vasiliev, 2021). It has a stellar mass of 4.09×10^5 $M_\odot$ (Baumgardt & Hilker, 2018) and a metallicity of -1.50 dex (Carretta et al., 2009). M3 contains the largest known population of RRL in any globular cluster of the Milky Way, with 236 reported by Cruz Reyes et al. (2024). Of these, 192 are included in our catalog and 118 have RUWE < 1.4. A segment of the tidal debris was first reported by Ibata et al. (2019b) as the Svöl stream based on Gaia DR2 data, and later associated with M3 by Bonaca et al. (2021) based on their energies and angular momenta. Yang et al. (2023), using Gaia DR3 data, verified this association and detected 35° of the leading arm and 21° of the trailing arm. These are the tracks analyzed in this study.

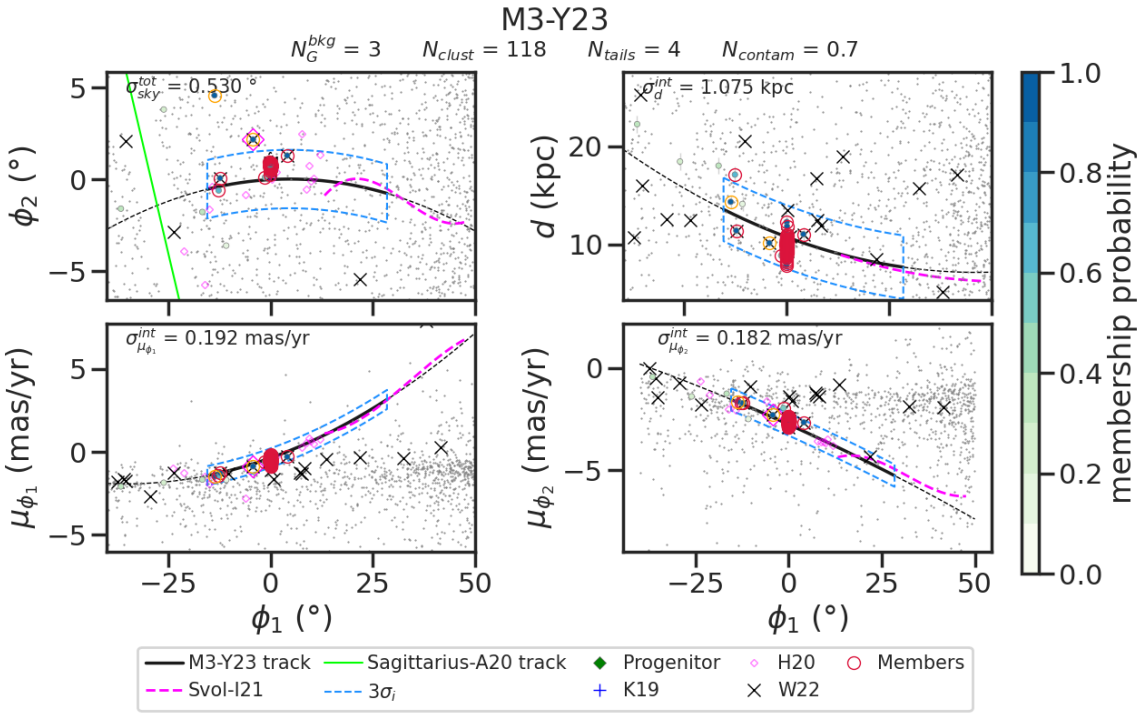

Figure 4.10: Similar to Fig. 4.1 but for the M3 stream. The black lines correspond to the tracks from Yang et al. (2023) and the magenta correspond to the Svöl segment from I21. The blue plus symbols are the extra-tidal RRL identified by Kundu et al. (2019); the light magenta diamonds are the star candidates from Hanke et al. (2020) and the bold diamond is the RRL identified by them; and the black crosses are the RRL associated with M3 by Wang et al. (2022). The empty space in the first panel correspond to area of sky occupied by the Sagittarius stream (green line, Antoja et al., 2020; Ramos et al., 2020).

We identified the 118 RRL with RUWE<1.4 within the cluster in our sample and only 4 RRL in the stream (expecting 0.7 of them to be contaminants); this is another case of a progenitor with a significant number of RRL within the cluster and just a few in the tidal tails. Previous studies have already identified RRL associated with M3. Kundu et al. (2019) identified 2 extra-tidal RRL (according to their classification), which we identified as part of the cluster. Hanke et al. (2020) identified 17

candidate member stars, including one RRL (magenta diamond on Fig. 4.10); we found that this RRL has a $p_{\rm memb} > 0.5$ but it is located too far from the celestial track ($4.28\sigma_{\phi_2}$) to be considered a member. Wang et al. (2022) using integrals of motion to identify RRab associated with halo substructures found that 31 RRL are likely to be associated with M3 (black crosses on Fig. 4.10); out of these, we identified only 3 with $p_{\rm memb} > 0.5$, including the one identified by Hanke et al. (2020). The rest of the RRL are too far from the tracks on at least one of the components, and the majority of them follow the peak of the background proper motion distributions, supporting their rejection as stream members. One of these identified members (Gaia DR3 3958056665299734144) has the highest photometric metallicity ([Fe/H]$=-0.73 \pm 0.37$ dex, Li et al., 2023) among the identified members, suggesting that this star is likely a contaminant.

4.2.9 Remaining streams with an associated progenitor

The other streams with an associated globular cluster studied in the present work are: M2, M5, NGC 1261, NGC 5466 and NGC 6101. These streams have between 1 and 2 RRL in their tails each; therefore, there is not much to say about them on a statistical or population level.

M2 (NGC 7089)
Is a globular cluster located at 11.69 kpc from the Sun (Baumgardt & Vasiliev, 2021) with a stellar mass of 6.24×10^5 $M_\odot$ (Baumgardt & Hilker, 2018) and a metallicity of -1.66 dex (Carretta et al., 2009). Kuzma et al. (2016) detected a diffuse stellar envelope around M2, and more recently I21 and Grillmair (2022) discovered its long tidal tails. We detected all the 17 RRL with RUWE<1.4 within the cluster in our sample (Cruz Reyes et al., 2024) and 2 RRL in the tails that are new detections. The default track (Grillmair, 2022) does not have distance information; therefore, to apply the method we took the shorter distance track from I21 and extrapolated it along ϕ_1. The two RRL identified in the tails are in the segment of the stream detected by I21, therefore, we cannot confirm whether the extrapolation made of the distance track was correct.

M5 (NGC 5904)
Is a globular cluster located at 7.48 kpc from the Sun (Baumgardt & Vasiliev, 2021) with a stellar mass of 3.92×10^5 $M_\odot$ (Baumgardt & Hilker, 2018) and a metallicity of -1.33 dex (Carretta et al., 2009). The $\sim 50^\circ$ long trailing arm of the stream was first detected by Grillmair (2019), and then a segment of it was independently detected again by I21. Using the default track in `galstreams`, the one by Grillmair (2019), we detected 71 RRL within the cluster (6 more than the ones identified by Cruz Reyes et al. (2024)) and 1 in the tails, which is a new detection. Abbas et al. (2021) associated 6 RRL to the stream, 3 with high confidence, 1 with intermediate, and 2 with low. We detected one of the high-confidence ones within the tidal radius of the cluster, the other 2 have $p_{\rm memb} > 0.5$ but they are too far from the celestial track ($6.09\sigma_{\phi_2}$ and $10.17\sigma_{\phi_2}$). Using, instead, the track from I21 we identified 2 more RRL in the tails, one is the intermediate-confidence RRL from Abbas et al. (2021) and the other is already detected with the default track, but again too far from the sky track ($2.94\sigma_{\phi_2}$). This once again highlights the sensitivity of the method to the tracks used. The other two low-confidence RRL from Abbas et al. (2021) are rejected by our model by us because of the large differences in proper motion with respect to the track.

NGC 1261
Is a globular cluster located at 16.4 kpc from the Sun (Baumgardt & Vasiliev, 2021) with a stellar mass of 1.27×10^5 $M_\odot$ (Baumgardt & Hilker, 2018) and a metallicity of -1.33 dex (Carretta et al., 2009). Previous studies detected the presence of an envelope around the cluster (e.g. Carballo-Bello et al., 2018; Kuzma et al., 2018). More recently Shipp et al. (2018) and I21 have independently detected the presence of a stream. We identified 2 of the 10 RRL with RUWE<1.4 within the cluster in our sample (Cruz Reyes et al., 2024) and 1 RRL in the tails; however, because of its low metallicity ([Fe/H] = -2.68 ± 0.33 dex, Li et al., 2023) it is likely a contaminant. Abbas et al. (2021) associated 2 RRL with

the NGC 1261 stream, one with intermediate confidence and one with low confidence, we rejected all of them as stream members.

NGC 5466
Is a globular cluster located at 16.12 kpc from the Sun (Baumgardt & Vasiliev, 2021) with a stellar mass of 5.60×10^4 $M_\odot$ (Baumgardt & Hilker, 2018) and a metallicity of -2.31 dex (Carretta et al., 2009). Odenkirchen & Grebel (2004) first reported the presence of extended tidal tails around NGC 5466, and following studies by Belokurov et al. (2006), Grillmair & Johnson (2006), Weiss et al. (2018) and I21 extended the detection of the stellar stream. We identified 20 of the 22 RRL with RUWE<1.4 within the cluster in our sample (Cruz Reyes et al., 2024); however, we identified 1 RRL as a cluster member that they did not, and 2 of the 3 stars we rejected have proper motions that differ significantly from that of the cluster. We identified 2 RRL in the tidal tails (1 new detection), one of which was already associated with the stream by Abbas et al. (2021) as a high-confidence candidate; the other high-confidence candidate that they associate is a cluster member under our criteria. They associated 2 more RRL with intermediate and low confidence, but these are not detected by us due to large differences in proper motion with respect to the track.

NGC 6101
Is a globular cluster located at 14.45 kpc from the Sun (Baumgardt & Vasiliev, 2021) with a stellar mass of 1.70×10^5 $M_\odot$ (Baumgardt & Hilker, 2018) and a metallicity of -1.98 dex (Carretta et al., 2009). I21 recently detected that the cluster possesses tidal tails spanning $\sim 10^\circ$ on the sky. We identified the 13 RRL with RUWE<1.4 within the cluster in our sample (Cruz Reyes et al., 2024) and 1 RRL in the tails, which is a new detection.

NGC 2808
Is a globular cluster located at 10.06 kpc from the Sun (Baumgardt & Vasiliev, 2021) and close to the Galactic disk ($b = -11.25^\circ$). It has a stellar mass of 7.91×10^5 $M_\odot$ (Baumgardt & Hilker, 2018) and a metallicity of -1.18 dex (Carretta et al., 2009). Carballo-Bello et al. (2018) and Kundu et al. (2021) reported the presence of extra-tidal stars around NGC 2808, while no tidal tail was found by Sollima (2020). More recently, I21 detected a $\sim 20^\circ$ long tidal tail nearly parallel to the Galactic disk. These tracks present a similar disagreement as the NGC 1851 stream (see Sec. 4.2.5) with offsets of $\Delta d = 1.25$ kpc, $\Delta\mu_{\phi_1} = -2.75$ mas/yr, and $\Delta\mu_{\phi_2} = -0.96$ mas/yr. Like in the case of NGC 1851, we applied a manual correction to make the tracks match the cluster. However, in this case, we did not identify any RRL in the tails, with or without correcting the tracks.

4.3 Streams without an associated progenitor

Now we will discuss the 35 streams (45 tracks) without an associated progenitor. Out of these, 15 did not have any RRL detected: Aquarius, C7, C8, C19, Gaia7, Gaia8, Gaia9, Gaia11, Gunnthrá, Hrid, Kshir, Kwando, M68[3], Slidr and Spectre.

4.3.1 Orphan-Chenab

The Orphan stream was one of the first stellar streams discovered (Grillmair, 2006; Belokurov et al., 2007). Sesar et al. (2013) and Hendel et al. (2018) characterized this segment of the stream using RRL; later, Koposov et al. (2019) extended the originally $\sim 60^\circ$ long stream up to $\sim 200^\circ$ through the Galactic disk connecting it with the previously discovered Chenab stream (Shipp et al., 2018). Koposov et al. (2019) has already performed a comprehensive analysis of the Orphan-Chenab's RRL population using Gaia DR2 data; they identified 110 RRL (black crosses in Fig. 4.11) of which 108

[3]This stream was identified by I21 and associated to the M68 cluster; however, due to discrepancies with the cluster and the other two tracks of the M68 stream in proper motion , it is not taken as a track of the tidal tails of M68, but as a new stream without a progenitor associated (see Sec. 4.2.7)

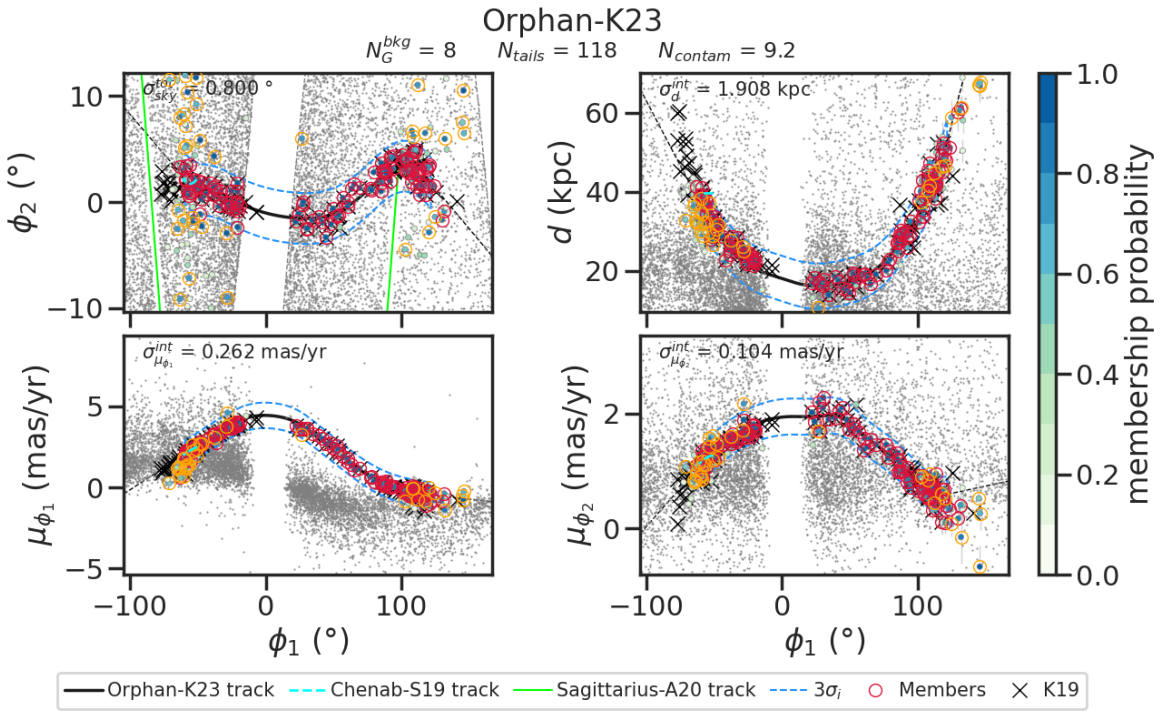

Figure 4.11: Similar to Fig. 4.1 but for the Orphan-Chenab stream. The black crossed are the RRL identified by Koposov et al. (2019). The cyan dashed lines is Chenab (the segment identified by Shipp et al., 2018). The green line is the Sagittarius stream track (Antoja et al., 2020; Ramos et al., 2020). The lack of stars correspond to the Galactic disk.

are in our catalog, all with RUWE<1.4 (although 9 of these are members of the Sagittarius stream, Ramos et al., 2021).

We identified 118 RRL in the Orphan-Chenab stream: 75 of them are shared with Koposov et al. (2019). Of the 33 that we did not recover, 6 are within the Sagittarius footprint (5 of them actually belonging to the Sagittarius stream (Ramos et al., 2021) and 3 more within the Galactic disk portion that we removed to avoid contamination (see Sec. 3.1). The rest are located in the locus of the intersection of the tracks with the background in proper motion (15 in the left extreme and 9 in the right; see Fig. 4.11), which makes the separation of both components more difficult. Among our identified members, there are 8 that belong to the Sagittarius stream (Ramos et al., 2021), 4 of them detected by Koposov et al. (2019) also. Therefore, we identified 39 new detections that belong to the Orphan-Chenab stream.

4.3.2 Jhelum

Jhelum is a complex stellar stream. It was first detected by Shipp et al. (2018) using DES data; later, by combining DES with Gaia DR2, Bonaca et al. (2019a) recognized two parallel branches of the stream separated in the sky ($\sim 1°$) with consistent proper motions. Meanwhile, also using DES and Gaia DR2, Shipp et al. (2019) detected two proper motion components with a spur in the spatial distribution. In addition, I21 using Gaia EDR3 recovered a unique component of Jhelum that lies between the components identified in previous studies. Among these tracks, the only one with a distance track is from I21; the others have only a mean distance (the same for both components). More recent studies (Woudenberg et al., 2023; Viswanathan et al., 2023; Awad et al., 2023) detected three components of Jhelum: The narrow and broad components (separated but not in parallel as in Bonaca et al. 2019a and separated in proper motion, similar to what Shipp et al. 2019 proposed) and

a tertiary spur component. A comparison of the different tracks is shown in Fig. 4.12.

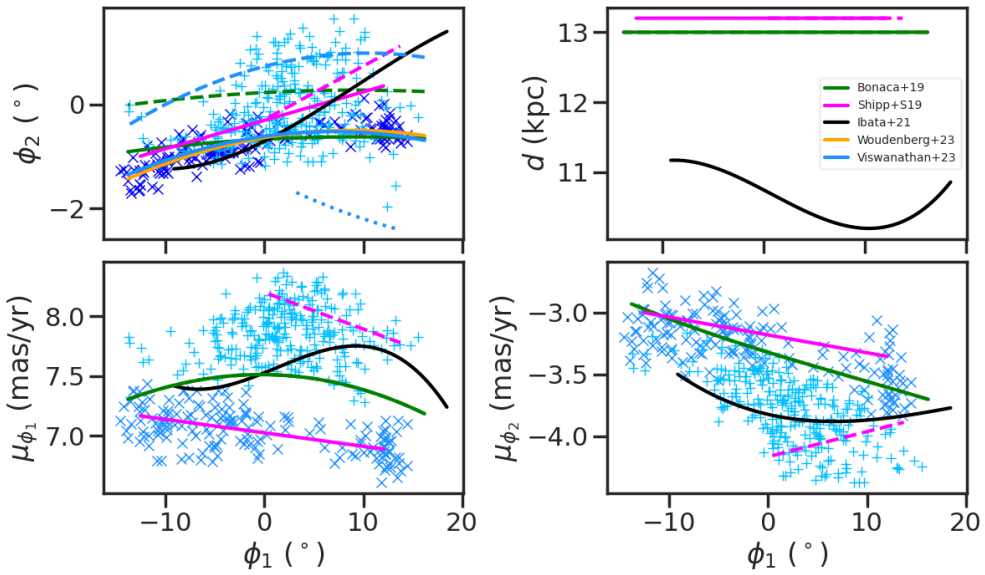

Figure 4.12: Comparison of the different tracks for the Jhelum stream in the literature. The solid lines correspond to the narrow component, the dashed lines to the broad one and the dotted one to the tertiary spur. The cross and plus symbols correspond to a robust selection of members from the narrow and broad component reported by Viswanathan et al. (2023, private communication).

We focus our analysis on the Shipp et al. (2019) track, which is the most consistent with the latest data. Component a is consistent with the narrow component, and component b is consistent with the broader one. We identified 3 RRL in the narrow component and 3 more in the broader one, all of which are new detections. The RRL of the broad component are too close together in ϕ_1; therefore, we only infer a mean distance (10.86 ± 0.32 kpc, dashed light red line in Fig. 4.13) instead of a distance track. This is different for the narrow component RRL, for which we fitted the 1D polynomial:

$$d[\text{kpc}] = 12.361 - 2.227 \times 10^{-2}\phi_1 \tag{4.1}$$

shown in Fig. 4.13 as a solid red line, which has a mean distance of $d = 12.49 \pm 0.36$ kpc. The mean values of the narrow and broad components are in perfect agreement with the mean values measured by Awad et al. (2023) for generic stars: 12.40 kpc for the narrow component and 10.95 kpc for the broad one. In addition, the mean distance of the narrow component is consistent with the mean values of Bonaca et al. (2019a, $d = 13.00$ kpc) and Shipp et al. (2019, $d = 13.20$ kpc), and the mean distance of the broad component is consistent with the mean value of Ibata et al. (2021, $d = 10.41$ kpc). We highlight the fact that we obtained two different values of distances for the two components, with the broader component located closer to the Sun than the narrow one; this is consistent with our method, even though the distance track used for both was the same.

The two components have different metallicities; we found that the narrow component is more metal-poor than the broad component ([Fe/H]$=-2.23 \pm 0.13$ and -1.74 ± 0.14 dex, respectively), but with the same spread ($\sigma_{[Fe/H]} \simeq 0.05$ dex). However, with only 3 stars per component, we cannot establish a robust value for the spread. These values are consistent with the spectroscopic members of Jhelum from Ji et al. (2020), who, using S^5 data, observed 7 stars with a mean metallicity of -2.19 dex and a spread of 0.17 dex, as well as another star with -1.62 dex. On the other hand, we obtained a more metal-poor narrow component and a slightly more metal-rich broad component than Awad et al. (2023), who, also using the metallicity data from the S^5 survey (Li et al., 2019), obtained a

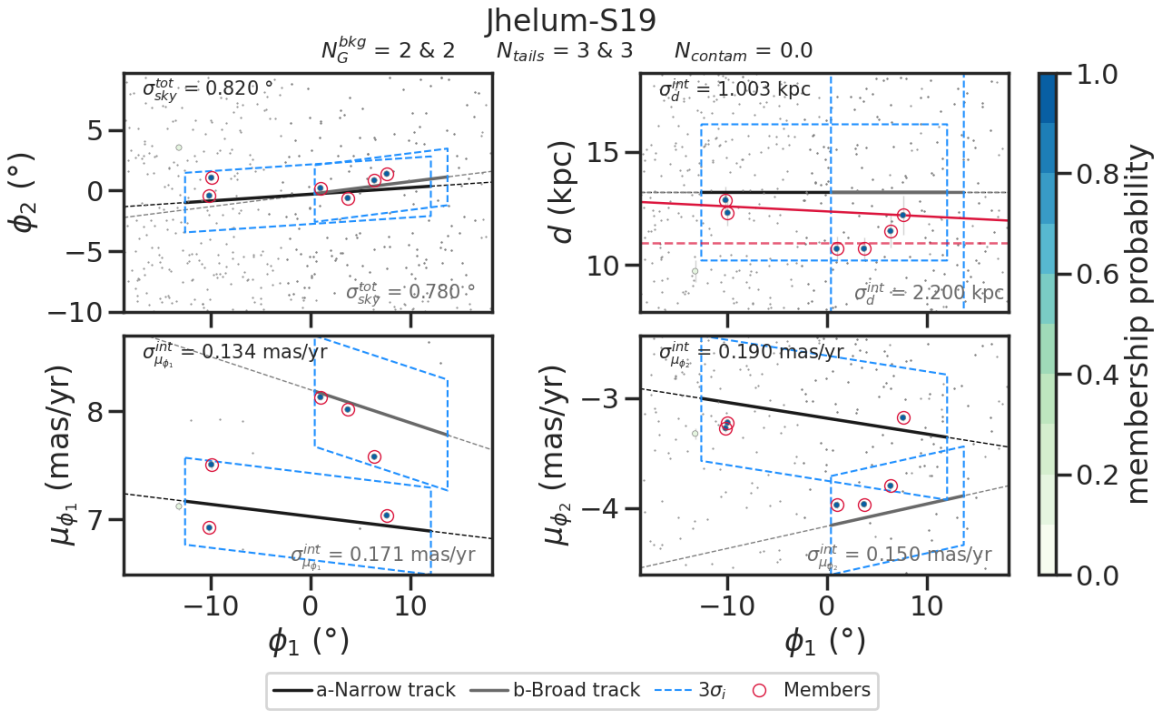

Figure 4.13: Similar to Fig. 4.1 but for the Jhelum stream. The black track and dispersions correspond to the component *a* of Shipp et al. (2019) (narrow component), and the gray ones to the component *b* (broad component). The solid red line correspond to the inferred gradient distance for the narrow component, and the dashed light red line correspond to the mean distance of the broad component.

mean metallicity (and spread) of -1.87 dex (0.15 dex[4]) and -1.77 dex (0.34 dex) for the narrow and broad components, respectively. Although the mean values of Awad et al. (2023) differ from ours, both results support the scenario in which the Jhelum stream is the result of a globular cluster accreted along with its host dwarf galaxy, both of which are now disrupted, similar to the M92 case (see Sec. 4.2.2). In this scenario, the cluster and dwarf galaxy would be responsible, respectively, for the narrow and broad components. Nonetheless, alternative scenarios have been proposed in the literature to explain the morphology of Jhelum (e.g., Bonaca et al., 2019a; Woudenberg et al., 2023); therefore, additional data are required to confirm this interpretation.

4.3.3 Cetus-Palca / Cetus-New

Cetus-Palca and Cetus-New are two different wraps of the same disrupted dwarf galaxy (Chang et al., 2020; Yuan et al., 2022). They occupy a similar portion of the sky, but Cetus-New is closer to the Sun than Cetus-Palca (average distance of $d \sim 18$ kpc and $d \sim 40$ kpc respectively, Yuan et al., 2022). The $\sim 145°$ long Cetus-Palca wrap is composed of the negative galactocentric radial velocity component of the Cetus stream (Newberg et al., 2009; Yuan et al., 2019) and the Palca stream (Shipp et al., 2018), whereas the $\sim 70°$ Cetus-New wrap is composed of the positive galactocentric radial velocity component of the Cetus stream (Newberg et al., 2009; Yuan et al., 2019) and the component detected by Yuan et al. (2022). The NGC 5824 globular cluster and the thin stellar streams Triangulum/Pisces (Bonaca et al., 2012; Martin et al., 2013), Willka Yaku, Turbio (Shipp et al., 2018), and C-20 (I21) are also associated with this accretion event (Bonaca et al., 2021; Li et al., 2022; Thomas & Battaglia, 2022; Yuan et al., 2022).

[4]This value is an upper limit of the metallicity spread for the narrow component.

We identified 77 RRL in the Cetus-Palca wrap, expecting 12.7 of them to be contaminants (Fig 4.14). There are 2 of them (Gaia DR3 4618720144066419200 and 5221073742370884352) that belong to the Large Magellanic Cloud (Soszyński et al., 2016) and another one (Gaia DR3 2569266959934381696) that belongs to the Sagittarius stream (Ramos et al., 2021). The majority of the RRab members are Oosterhoff type II (OoII, 39 out of 52). The separation between both types is made using Eq. 2 of Belokurov et al. (2018). The majority of the Oosterhoff type I (OoI, 9 out of 13) are located at the right extreme of the track, where the outskirts of the Magellanic Clouds are located; therefore, these stars are likely contaminants (even though they are not members according to Soszyński et al. 2016). The photometric metallicity of the RRL members is consistent with previous studies (Yuan et al., 2022; Thomas & Battaglia, 2022); we found a mean value of -1.94 ± 0.04 dex and a spread of 0.44 dex.

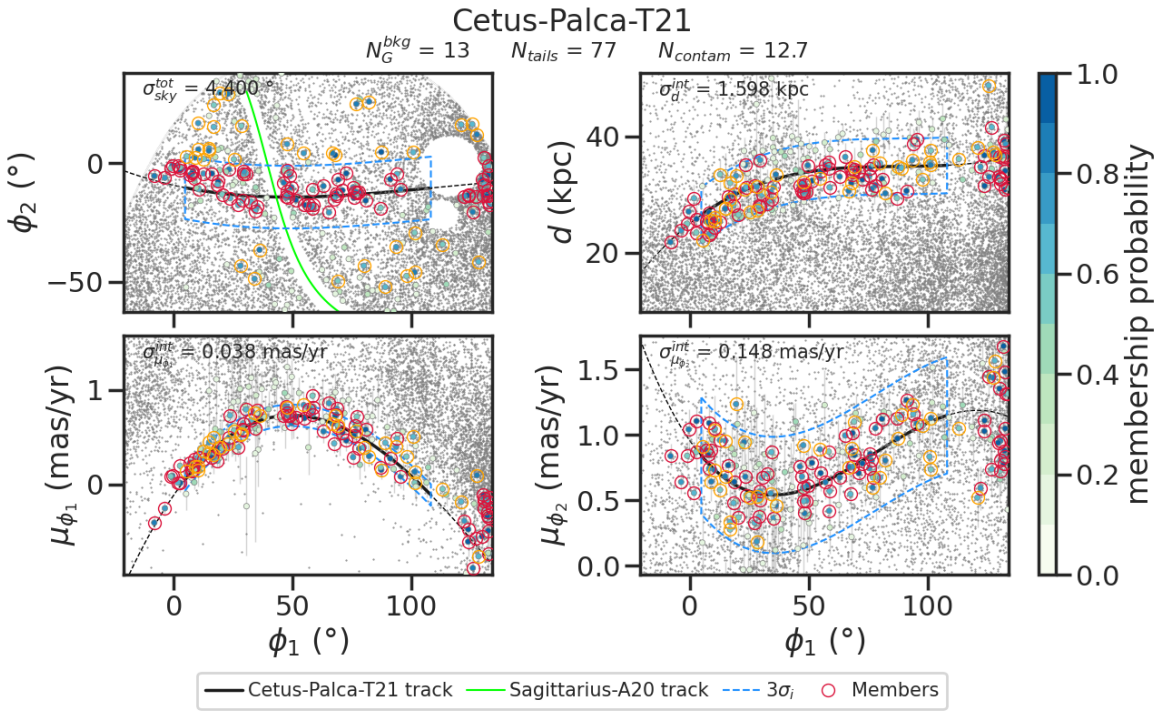

Figure 4.14: Similar to Fig. 4.1 but for the Cetus-Palca stream. The green line is the Sagittarius stream track (Antoja et al., 2020; Ramos et al., 2020). The empty areas in the sky correspond to the Galactic dik and the Magellanic Clouds.

In the Cetus-New wrap we identified 4 RRL, expecting no contaminants; however, the member Gaia DR3 4618054183617627904 actually belongs to the Large Magellanic Cloud. The other 3 members consist of 1 RRab and 2 RRc, where only 2 of them have photometric metallicity, consistent with the metallicity of the Cetus-Palca warp.

4.3.4 ATLAS-AliqaUma

The ATLAS-AliqaUma (AAU) stream was proposed by Li et al. (2021) to be a single structure that unifies the previously identified ATLAS (Koposov et al., 2014) and AliqaUma streams (Shipp et al., 2018). Observations from the S^5 spectroscopic survey revealed that the stream appears discontinuous in the sky but remains coherent in distance, proper motion, and radial velocity (see Fig. 4.15). Except for the features of "kink" ($\phi_1 \sim 12°$) and "broadening" ($\phi_1 \sim 0°$), the stream has a narrow width (< 100 pc) and low velocity dispersion ($\sigma_{GSR} = 4.8$ km/s); these, combined with a low metallicity dispersion and with a mean metallicity of [Fe/H]=-2.24 dex, suggest a globular origin (Li et al., 2021).

We identified 10 RRL in the AAU stream, expecting 0.4 of them to be contaminants; 9 of these are in the ATLAS segment of the stream. Li et al. (2021) using S^5 spectroscopic data identified 5 RRL in the stream (black crosses in Fig. 4.15). We are able to recover all 4 RRL that lie on the ATLAS segment; the one that lies on the AliqaUma segment has a $p_{\rm memb} > 0.5$ but it is too far from the celestial track to be selected as a member. The authors also selected 6 more non-spectroscopic candidates that are consistent with the stream in position and distance (green circles on their Fig. 6), in particular, 2 RRL located at $\phi_1 \sim 6$. However, they did not publish which stars they are, and therefore, no further comparison can be made; although visually they match the location of two of our detections. In summary, we identified 10 RRL members, of which 6 are new detections.

The photometric metallicity of the RRL is consistent with the spectroscopic metallicity of the stream; they have a mean metallicity of [Fe/H]$=-2.21 \pm 0.10$ dex, with a spread of 0.12 dex. There is a subtle spread on the Oosterhoff type of the RRL: there are 8 RRab, of which 3 are type OoI and 5 are type OoII. Since the spread in the period-amplitude diagram is small (much smaller than in the M92 system), it could be attributed to the RRL leaving the zero-age horizontal branch, increasing their luminosities and, therefore, their periods (instead of a metallicity gradient); this also occurs in several globular clusters, of both Oosterhoff types, such as M5, M68 and M3 (see Fig. 4 of Cacciari et al., 2005). There is no clear spatial segregation of the Oosterhoff type in the stream.

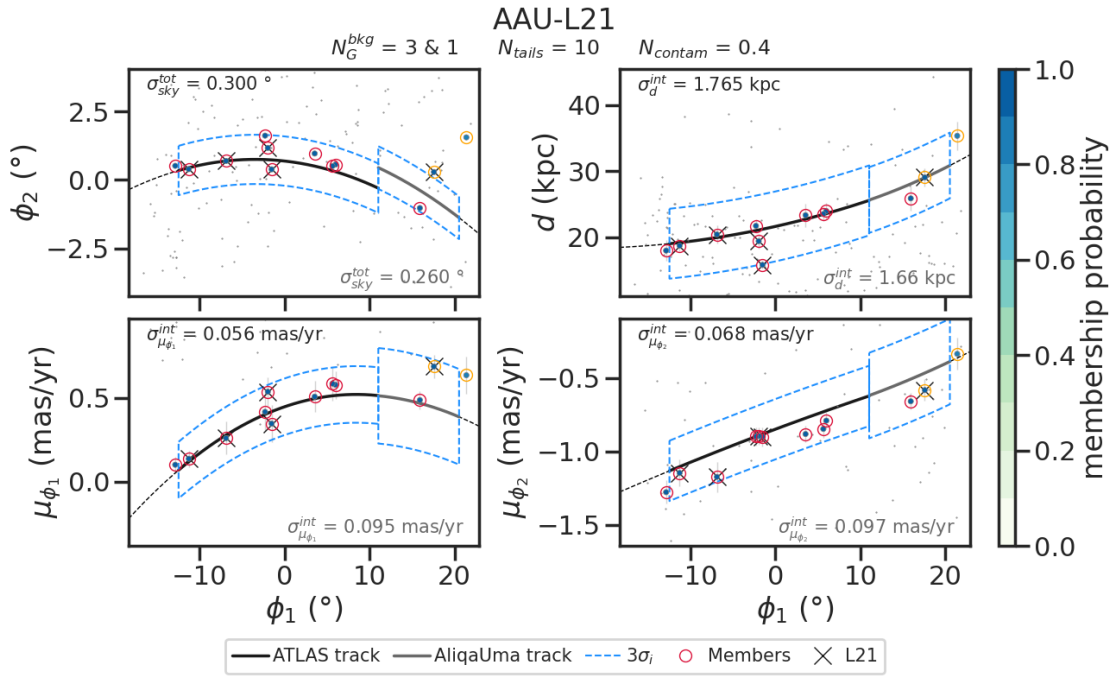

Figure 4.15: Similar to Fig. 4.1 but for the AAU stream. The black crosses are the RRL identified by Li et al. (2021). The black track and dispersions correspond to the ATLAS segment, the gray ones to the AliqaUma segment; both tracks are from Li et al. (2021).

4.3.5 GD-1

GD-1 is a long and cold stellar stream first detected by Grillmair & Dionatos (2006), believed to have a globular origin (Koposov et al., 2010) although no progenitor is associated with it. Subsequent studies revealed complex morphological features (see top panel of Fig. 1.1) such as gaps, 'spurs', 'blobs', and 'cocoons' (e.g., Price-Whelan & Bonaca, 2018; Malhan et al., 2019; Valluri et al., 2025). All these characteristics make it an ideal system for exploring the distribution of the dark matter halo and its

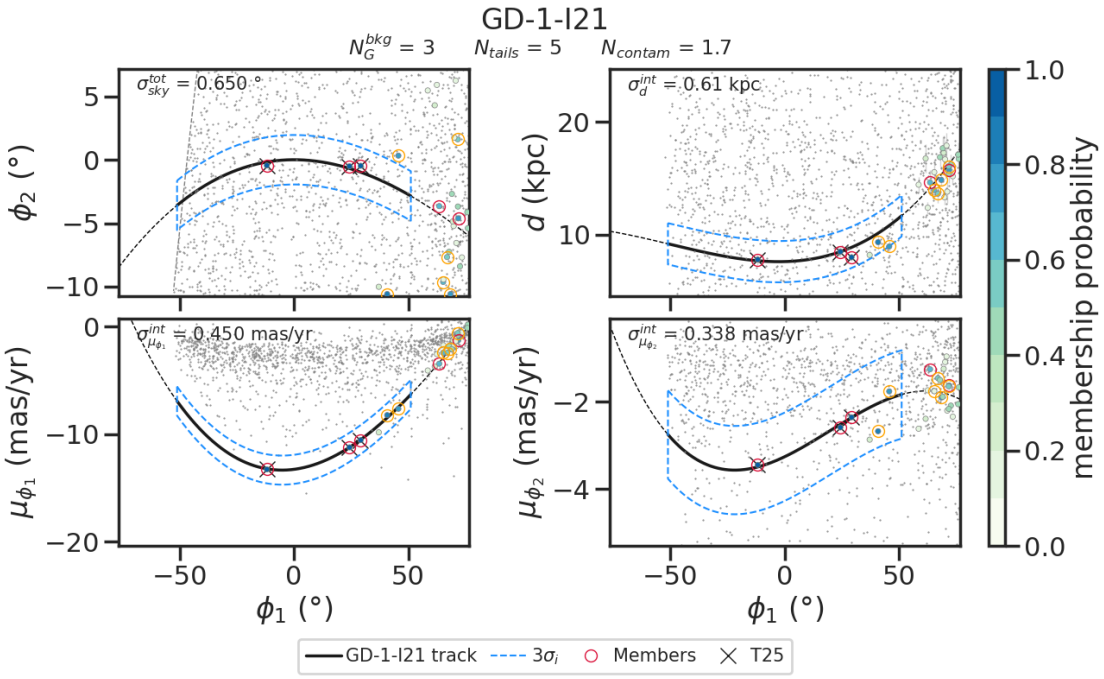

Figure 4.16: Similar to Fig. 4.1 but for the GD-1 stream. The black crosses are the RRL identified within the sample of Tavangar & Price-Whelan (2025). The lack of stars correspond to the Galactic disk.

subhalos (e.g., Koposov et al., 2010; Bonaca et al., 2019b; Nibauer & Bonaca, 2025).

The default track is from I21. We identified 5 RRL members, expecting 1.7 to be contaminants. There are two of these members (Gaia DR3 1412046334799096704 and 1429088936827962752) that lie on the intersection of the stream tracks and the locus of the background in proper motion (see Fig. 4.16). In addition, their photometric metallicity ([Fe/H]$=-1.62 \pm 0.32$ and -1.45 ± 0.46 dex) is very different from the metallicity of the stream ([Fe/H] $\simeq$ -2.50 dex, Valluri et al., 2025); therefore, they are likely contaminants. Although there is no study of RRL in GD-1 in particular, Tavangar & Price-Whelan (2025) used Gaia DR3 data to create a density map of the stream, where, within the sample they used, there are the other 3 RRL members that we identified successfully. Furthermore, using the track from Price-Whelan & Bonaca (2018), we identified only these 3 RRL, supporting these as bona-fide members of the stream.

4.3.6 LMS-1

The "low-mass stream" (LMS-1) is a stellar stream located towards the north of the Galactic bulge at the inner part of the Galaxy (between ∼10 kpc and ∼20 kpc from the center) in a very polar orbit (Yuan et al., 2020). It has a mean metallicity and spread of -2.10 and 0.42 dex, respectively, a physical width of 700 pc, and a tangential velocity dispersion of 35.4 km/s (Malhan et al., 2021b); these are indicators of a dwarf galaxy origin. Moreover, the globular clusters NGC 5054 and NGC 5053 are associated with the LMS-1 stream, where NGC 5054 is thought to be the nuclear star cluster of the dwarf galaxy progenitor of both the stream and the globular clusters (Yuan et al., 2020), similar to the scenario we propose for the M92 (Sec. 4.2.2) and Jhelum (Sec. 4.3.2) streams.

The default track in `galstreams` is from Yuan et al. (2020); however, this is too long to apply our method (∼ 175°); therefore, we analyzed the much shorter track from Malhan et al. (2021b, ∼ 50°). Both are in excellent agreement (fifth row of Fig. 5 from Mateu, 2023), although the track from Mal-

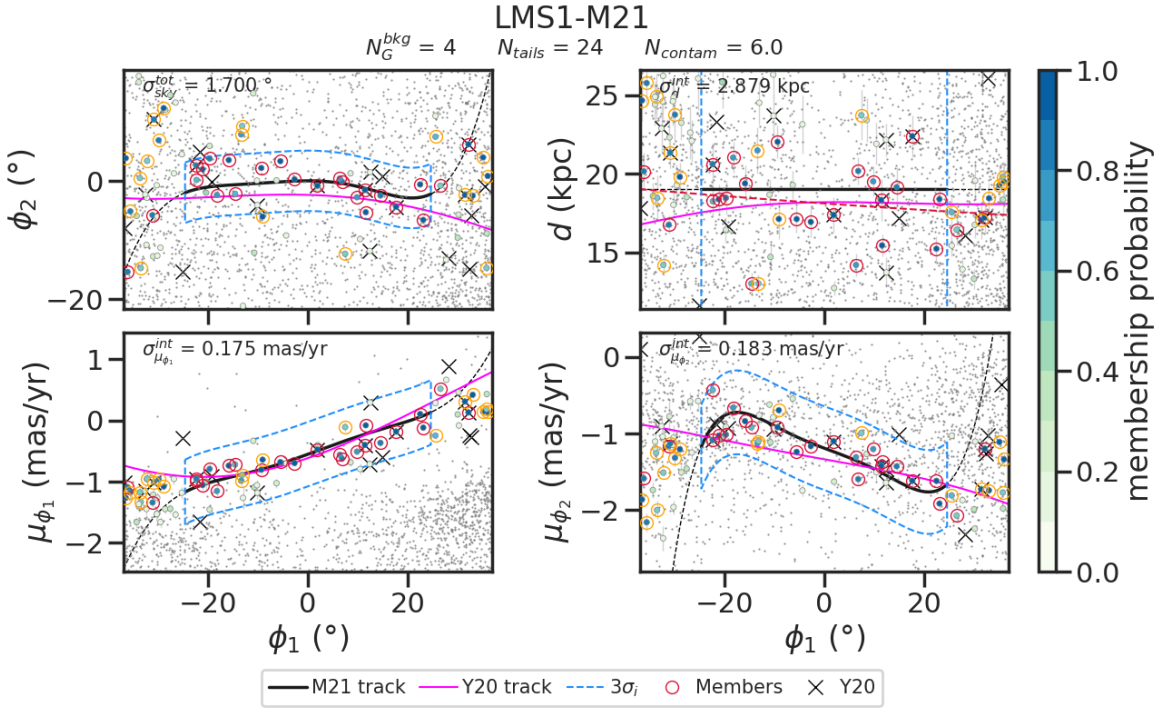

Figure 4.17: Similar to Fig. 4.1 but for the LMS-1 stream. The magenta lines are the tracks from Yuan et al. (2020) and the black crosses are the RRL reported by them.

han et al. (2021b) only has a mean distance (19.0 kpc). We identified 24 RRL of which 19 are new detections; however, we expect 6.0 of them to be contaminants.

Yuan et al. (2020) did the first report of LMS-1 identifying RRL and Blue Horizontal Branch stars (BHB) on the stream. They reported 20 RRL (black crosses in Fig. 4.17), of which we recovered only 5. It is important to mention that their RRL cover a projected width of 8.7° and are likely to belong to multiple wraps of the stream (Yuan et al., 2020). The projected width of the Malhan et al. (2021b) track is 1.7°; therefore, it is not surprising that we did not recover all the RRL from Yuan et al. (2020) since we focused on the analysis of only one wrap using the Malhan et al. (2021b) track. Malhan et al. (2021b) mention that they selected 91 RRL that follow the orbit of LMS-1; however, they did not publish a list of members; therefore, no further comparison is possible.

With the identified RRL we fitted a distance track using a first degree polygonal[5] (red dashed line in the upper right panel of Fig. 4.17):

$$d[\text{kpc}] = 18.13 - 2.25 \times 10^{-2}\phi_1. \tag{4.2}$$

The track is consistent with the mean value of Malhan et al. (2021b), and with the distance track of Yuan et al. (2020) in this segment of the stream ($-35° < \phi_1 < 35°$). However, since our inferred distance track has a negative slope, this behavior causes the track to differ from that of Yuan et al. (2020) for $\phi_1 \lesssim -15°$. This stream is another example of a good candidate for a blind search.

4.3.7 Turranburra

Turranburra is a stellar stream with an extension of 16.9° and a projected width of 0.60° (Shipp et al., 2018). It has a metallicity and spread of -2.18 and 0.39 dex, respectively (Li et al., 2022). Both the

[5]When a second degree polygonal is fitted, the quadratic coefficient is neglectable (6.49×10^{-5}); therefore, we used a first degree polygonal.

projected width and the metallicity spread are indicators of a dwarf galaxy origin (Shipp et al., 2018; Li et al., 2022). The stream was first reported by Shipp et al. (2018) and was further studied by Shipp et al. (2019) and Li et al. (2022). The default track (Shipp et al., 2019) does not have distance information; therefore, the mean heliocentric distance of 27.5 kpc from Shipp et al. (2018) is instead implemented.

We identified 14 RRL in the stream, expecting 1.8 of them to be contaminants (Fig. 4.18). Among the members, there is one (Gaia DR3 5091015982252983680) that has a photometric metallicity of [Fe/H]=−4.12±0.27 dex (Li et al., 2023). Never before has such a metal-poor RRL been observed (only a few stars); therefore, this must be an extrapolation of the metallicity-ϕ_{31} relation in a regime in which it should not be valid. The other members have a mean photometric metallicity of -1.75 ± 0.08 dex with a spread of 0.12 dex – higher than the one proposed by Li et al. (2022), but in more agreement with the one estimated by Shipp et al. (2018, Z=0.0003, i.e. [Fe/H]=-1.67 dex using $Z_\odot = 0.014$). Shipp et al. (2019) selected 13 RRL around the Turranburra stream based on sky ($|\phi_1| < 8.5°$, $|\phi_2| < 5°$) and distance ($|\Delta d| < 3$ kpc with respect to mean distance), shown as black crosses in Fig. 4.18; however, none of them are identified as members of the stream according to their criteria. We identified 6 of them as members, and 3 more also have a $p_{\rm memb} > 0.5$ but they are too far from the celestial track.

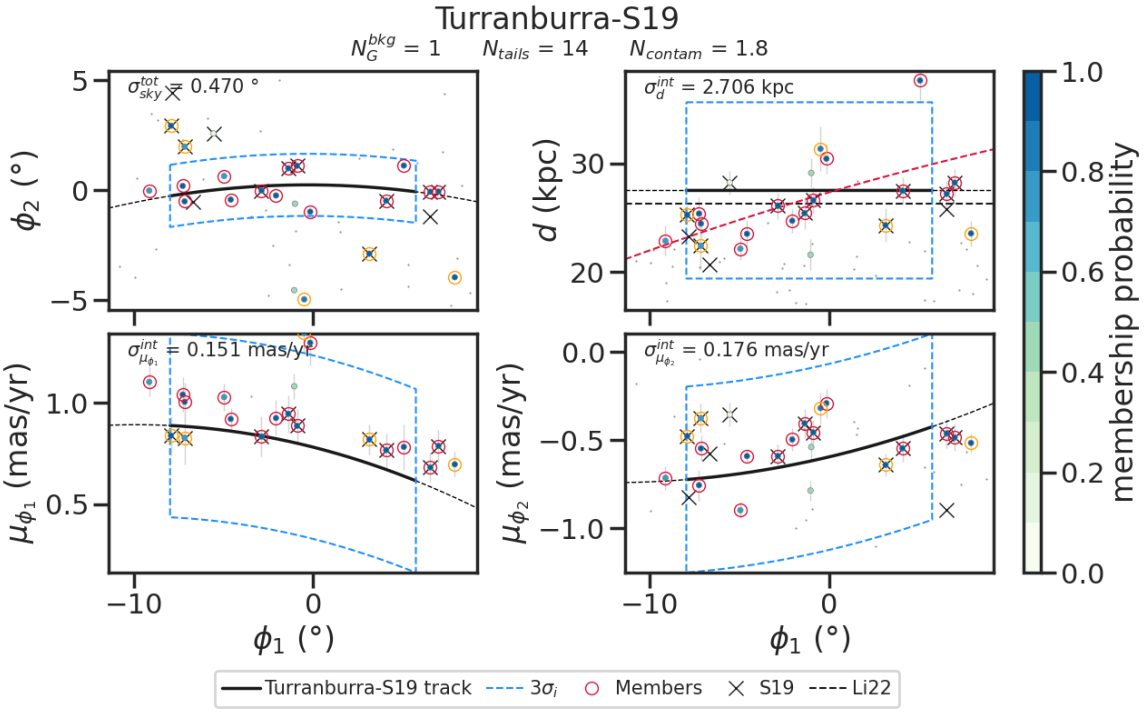

Figure 4.18: Similar to Fig. 4.1 but for the Turranburra stream. In the upper right panel, the red dashed line is the distance track inferred from the RRL we identified, and the black dashed line is the one proposed by Li et al. (2022).

Since this track does not have previously reported distance information as a function of ϕ_1, we fitted a second degree polynomial, obtaining the following distance track shown in the upper right panel of Fig. 4.18 as a red dashed line:

$$d[\text{kpc}] = 27.733 + 4.812 \times 10^{-1}\phi_1 - 5.368 \times 10^{-3}\phi_1^2. \tag{4.3}$$

Li et al. (2022) using the RRL of the S^5 survey in the Turranburra region inferred a mean distance of 26.3 kpc (black dashed line in the upper right panel of Fig. 4.18), consistent with our results.

4.3.8 Indus

Indus is a stellar stream with an extension of 20.3° and a projected width of 0.83° (Shipp et al., 2018). It has a metallicity and spread of -1.96 and 0.33 dex, respectively (Li et al., 2022). Both the projected width and the metallicity spread are indicators of a dwarf galaxy origin (Shipp et al., 2018; Li et al., 2022). The stream was first reported by Shipp et al. (2018) and was further studied by Shipp et al. (2019), Ji et al. (2020), Hansen et al. (2021), and Li et al. (2022). The default track (Shipp et al., 2019) does not have distance information; therefore, the mean heliocentric distance of 16.6 kpc from Shipp et al. (2018) is implemented instead.

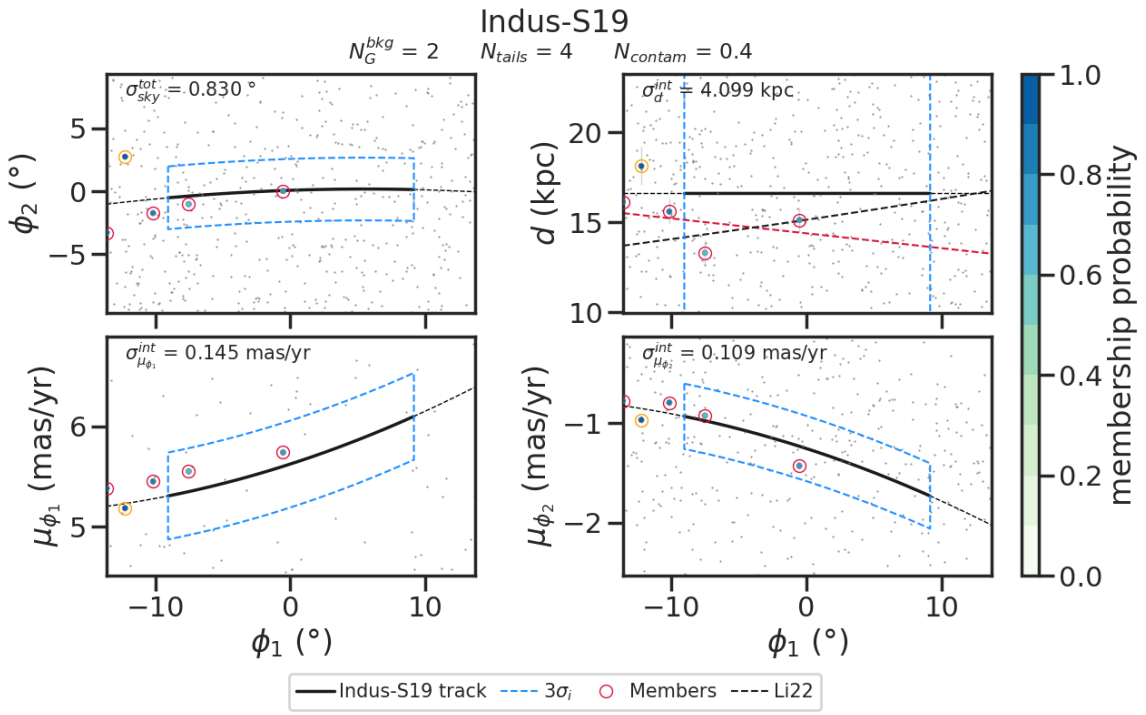

Figure 4.19: Similar to Fig. 4.1 but for the Indus stream. In the upper right panel, the red dashed line is the distance track inferred from the RRL we identified, and the black dashed line is the one proposed by Li et al. (2022).

We identified 4 RRL in the stream (expecting 0.7 contaminants); this allows us to assign a more precise value to the distance track of the Indus stream (Fig. 4.19). We fitted a first degree polynomial, obtaining the following distance track:

$$d[\text{kpc}] = 14.38 - 8.27 \times 10^{-2}\phi_1. \tag{4.4}$$

Li et al. (2022) used RRL from the S^5 survey to assign a distance modulus gradient: $\mu[\text{mag}] = 15.90 + 1.60 \times 10^{-2}\phi_1$[6]. This gradient has a slope opposite to ours; however, since they did not publish which RRL they used to make the deduction, a more detailed comparison is not possible. Nevertheless, while one of our identified RRL lies within the field of S^5, the other three are further along the direction of the stream. With this kind of low number statistics, each star has a strong influence on the inferred gradient; for example, excluding the leftmost RRL would yield a positive slope consistent with that of Li et al. (2022). This could account for the discrepancy between the two results.

[6]Li et al. (2022) adopted a left-handed coordinate system to define their stream frame of reference; therefore, we invert the sign of the angular coordinate ϕ_1 in their distance modulus gradient to be consistent with the right-handed coordinate system used here.

4.3.9 Elqui

Elqui is a stellar stream with an extension of 9.4° and a projected width of 0.54° (Shipp et al., 2018). It has a metallicity and spread of -2.22 and 0.27 dex, respectively (Li et al., 2022). Both the projected width and the metallicity spread are indicators of a dwarf galaxy origin (Shipp et al., 2018; Li et al., 2022). The stream was first reported by Shipp et al. (2018) and was further studied by Shipp et al. (2019) and Li et al. (2022). The default track (Shipp et al., 2019) does not have distance information; therefore, the mean heliocentric distance of 50.1 kpc from Shipp et al. (2018) is implemented instead (it is the most distant DES stream).

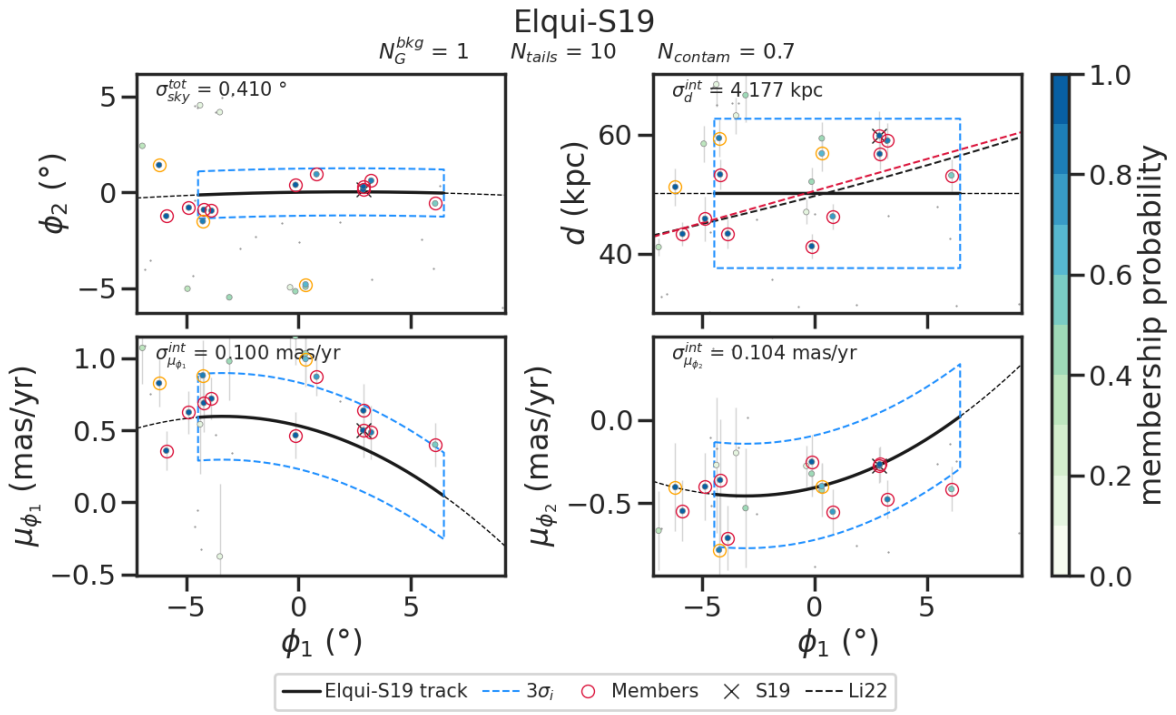

Figure 4.20: Similar to Fig. 4.1 but for the Elqui stream. In the upper right panel, the red dashed line is the distance track inferred from the RRL we identified, and the black dashed line is the one proposed by Li et al. (2022).

We identified 10 RRL in the stream, expecting 0.7 of them to be contaminants (Fig. 4.20). With them, we inferred a new distance gradient by fitting a 1D polynomial, obtaining the following track shown in the upper right panel of Fig. 4.20 as a red dashed line:

$$d[\text{kpc}] = 50.524 + 1.071\phi_1 \tag{4.5}$$

Li et al. (2022) using the RRL of the S^5 survey in the Elqui region inferred a gradient distance that is in excellent agreement with ours, shown as a black dashed line in (Fig. 4.20). In addition, all members, except for one already reported as a member by Shipp et al. (2019, black cross in Fig. 4.20), are new detections.

The photometric metallicity of the identified members is consistent with that reported by Li et al. (2022). They have a median of [Fe/H]=-2.06 ± 0.09 dex with a spread of 0.15 dex. However, there is one star (Gaia DR3 5000591527509120384) that has a photometric metallicity of [Fe/H]=-1.75 ± 0.28 dex, more metal-rich than the rest of the members but still consistent within the errors.

4.3.10 Phlegethon

Phlegethon is a 75° long retrograde stellar stream of globular origin, which lies close to the Sun at a mean heliocentric distance of 3.8 kpc (Ibata et al., 2018). It was first detected by Ibata et al. (2018) and was further studied in I21, who obtained a metallicity of [Fe/H]=-2.19 dex. We identified 3 RRL in the tails; these are new detections and have consistent photometric metallicity with the stream. One of them lies on the extended track of the stream, verifying that this extrapolation is correct.

4.3.11 Remaining streams without an associated progenitor

The other streams without an associated globular cluster studied in the present work are: Gaia1, Gaia6, Gaia10, Gaia12, Jet, Leiptr, Ophiuchus, Sylgr, and Ylgr. These streams have between 1 and 2 RRL; therefore, we restrict ourselves to giving an average measurement of the distance (see Table 4.2) since, with so few RRL, it is not possible to perform a statistical analysis of the population.

Chapter 5

Discussion

5.1 Segregations and bimodalities

After analyzing all the 56 stellar streams with proper motion tracks and distance measurements available in `galastreams`, we found a segregation by RRL type exclusively in the Pal 5 stream. Resolving whether this kind of segregation was a common feature between the streams or just a peculiarity of Pal 5 was one of the motivations of this work. While it seems to be one of a kind, we did observe a segregation by Oosterhoff type in three streams: Cetus-Palca, AAU and M92. In the Cetus-Palca stream, while the majority of their RRab members are OoII (39 of 52), we identified a concentration of OoI RRL (9 of 13) at the right extreme of the reported track; however, this region is close to the LMC in the sky and one of them was identified as an LMC member by Soszyński et al. (2016); therefore the rest of the OoI RRL of this group might be contaminants that belong to the LMC too. In the AAU stream, we identified 8 RRab, of which 3 are OoI and 5 are OoII; since the spread in metallicity of this stream is small (Li et al., 2021), this segregation might be due to stellar evolution where the OoII are leaving the zero-age horizontal branch, increasing their luminosity and therefore their period. In the M92 stream, there is a clear segregation between the RRL of the cluster and tails, where the cluster ones are OoII and the tails ones are OoI; in this case, this is a consequence of the different metallicity of both groups of RRL (lower metallicities imply higher pulsation periods Catelan & Smith, 2015), as described below.

Moreover, we observed three cases with a bimodality in metallicity: ωCen, Jhelum and M92. In ωCen, we observed a bimodal segregation in the RRL population of the cluster ([Fe/H] = -2.11 and -1.50 dex) consistent with the multiple populations reported using other tracers ([Fe/H] = -2.11, -1.85, -1.50 and -1.19 dex, Kuzma & Ishigaki, 2025); we also identified these two populations in the RRL population of the tidal tails. In the case of Jhelum, we found that its narrow and broad components have different distances and metallicities: while the narrow one is more distant ($d = 12.49 \pm 0.36$ kpc) and more metal-poor ([Fe/H]$= -2.23 \pm 0.13$ dex), the broad one is closer ($d = 10.86 \pm 0.32$ kpc) and more metal-rich ([Fe/H]$= -1.74 \pm 0.14$ dex); this supports the scenario where Jhelum is the result of both a disrupted globular cluster and dwarf galaxy that were accreted by the Milky Way. Finally, in the case of M92, a bimodality in metallicity with a difference of $\sim$0.6 dex is observed between the RRL population of the cluster ([Fe/H]$=-1.6 \pm 0.1$ dex) and the tidal tails ([Fe/H]$=-2.2 \pm 0.1$ dex); this, along with other evidences, leads us to hypothesize that M92 is the nuclear star cluster of a disrupted dwarf galaxy, which is the one that forms the stream, similar to M54 and Sagittarius, or LMS-1 and NGC 5053 and NGC 5054.

In summary, the segregation of the RRL in the streams by type of RRL or Oosterhoff is not a standard feature along the streams; but it is rather a peculiarity of a few, or even contamination from other substructures. On the other hand, the presence of segregation and bimodalities in metallicity indicates a more complex origin history, either because the progenitor of the stream is simply a dwarf galaxy, or because it has more than one associated component, such as a globular cluster embedded in

its host galaxy that may or may not be both disrupted.

5.2 RRL in the progenitor and its tidal tails

A relevant observation from our analysis of the RRL in the clusters and tails of streams with an associated progenitor is that those whose progenitor has a significant number of RRL, have only a handful in their tails, such as in M3, ω Cen, or NGC 3201. This can be explained through mass segregation.

Mass segregation is a well-known dynamical process in globular clusters, whereby the more massive members gradually migrate to the cluster center, while the lighter ones tend to move farther from it (Spitzer, 1987). To study the impact of this process on stellar escape and tidal tail formation, Balbinot & Gieles (2018) applied the cluster evolution code `EMACSS` (Gieles et al., 2014; Alexander et al., 2014), combined with a semi-analytic model for the evolution of the stellar mass function, and found that the first stars to escape are preferentially of low mass. As a result, stellar streams are more easily detected when the progenitor is close to dissolution, such that a higher fraction of massive (and therefore brighter) stars are in the tails; and near apocenter, where the stream is in the most densely packed stage.

The RRL, being evolved stars, are among the most massive stars that are still alive in the population; thus, their escape is a sign that the progenitor of the stream is in the final stages of dissolution, as seen in Tucana III or Pal 5. Vice versa, this implies that progenitors with the largest populations of RRL are not necessarily optimal targets for identifying RRL in their tidal tails or to detect the tails at all.

In Fig. 5.1, we can empirically see this, where we show the remaining mass fraction of the cluster (μ, left panel) and lifetime (T_{diss}, right panel) as a function of the ratio between RRL on the progenitor and the total. We separate the streams with an associated progenitor of our sample into three groups: 1) Those with many RRL (>10) and the majority of them (>50%) in the cluster (M3-Svöl, ωCen-Fimbulthul, NGC 3201-Gjöll, M5, M68-Fjörm, NGC 5466, M2, NGC 1851, and NGC 6101) shown as blue dots; 2) those with few RRL and the majority of them in the cluster (NGC 2298, NGC 1261, NGC 288, NGC 2808, and NGC 6397)[1] shown as green symbols; and 3) those with the majority of the RRL in the tidal tails (Tucana III, Pal5, and M92 [2]) shown as magenta dots. These numbers indicate that streams with the majority of the RRL in their tails are not common, suggesting that this might be a short stage in the process of producing a stellar stream.

This classification is consistent with the lifetimes of their progenitors (Baumgardt et al., 2019, 2023) and with the expected outcome from mass segregation. Clusters in the first group have long lifetimes, exceeding a Hubble time in almost all cases, whereas those in the second and third groups with low-mass systems and most of their RRL in their tidal tails, respectively, have short lifetimes. In particular, in group 2, NGC 2298 has a lifetime of only $T_{\rm diss} = 2.4$ Gyr and a remaining mass cluster fraction $\mu = 0.08$, but this is a result of its unusually high inferred initial mass (Baumgardt et al., 2019, 2023). On the other hand, NGC 1261 and NGC 2808, shown as green triangles in Fig. 5.1, have more than 10 RRL in their progenitors according to Cruz Reyes et al. (2024); therefore, they actually belong to the first group. The relation between the fraction of RRL and mass retained in the progenitor further supports this picture. Clusters with a higher remaining mass cluster fraction tend to retain more of their RRL. This is consistent with the expected production rate of these stars and indicates that the RRL escape the progenitor along with an amount of mass proportional to their number.

We also observed that streams where most RRL are found in the tails tend to lie near apocenter, where tidal debris is most spatially concentrated and easier to detect, although this does not necessarily reflect a direct causal connection with RRL escape, rather an observational bias. Other orbital

[1] NGC 6397 has zero RRL at all and, therefore, is not represented in Fig. 5.1.

[2] In the case of M92, according to our hypothesis (see Sec. 4.2.2), the RRL of the cluster and tails are independent of each other; thus, this stream would not formally belong to group 3, but we keep it in it.

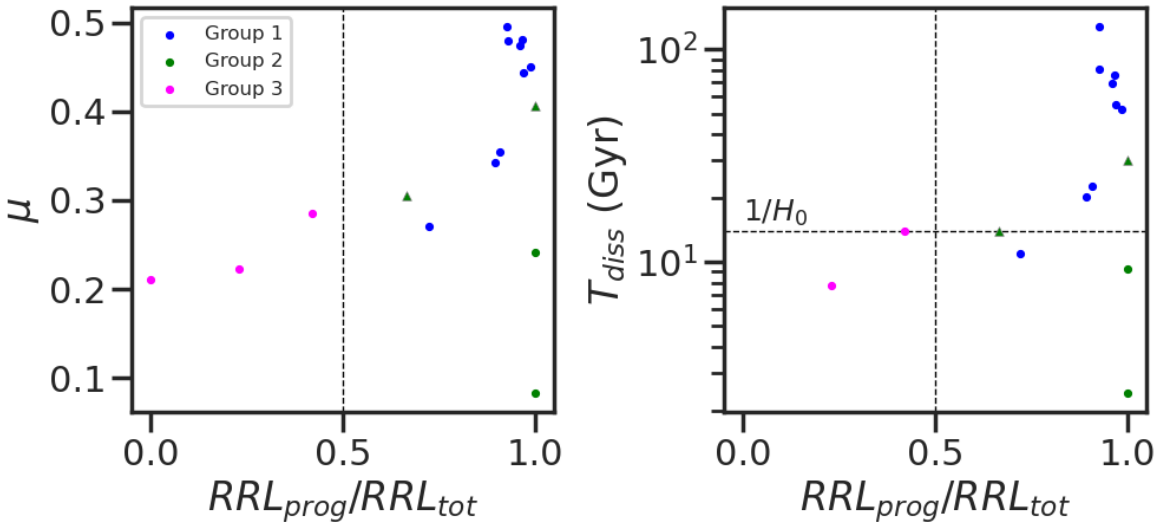

Figure 5.1: Remaining mass fraction of the cluster (μ, right panel) and lifetime (T_{diss}, left panel) as function of the ratio between RRL on the progenitor and the total. Group 1 (blue dots) correspond to streams with many RRL (>10) and the majority of them (>50%) in the cluster, group 2 (green symbols) correspond to those with few RRL and the majority of them in the cluster; and group 3 (magenta dots) to those with the majority of the RRL in the tidal tails. In the bottom panel, there is a missing point from group 3, corresponding to Tucana III, due to the lack of a inferred lifetime in the literature. In group 2, the triangle symbols correspond to NGC 1261 and NGC 2808 which have more RRL than the ones we identify (>10, Cruz Reyes et al., 2024); therefore, actually belonging to the first group.

parameters, including tidal radius, eccentricity, pericenter, and apocenter distance, were explored but show no clear correlation with the RRL ratio (not shown).

We found that there is a higher fraction of streams with associated RRL in those with progenitors (13/17, ∼75%) than in those without (19/34, ∼45%); this does not contradict what we stated in this chapter. Even though we expect to find more RRL in the tidal tails of streams whose progenitor is close to dissolution, the currently progenitor-less streams are likely less massive (lower mass means shorter lifetimes); therefore, a smaller number (or none) of RRL is expected in them.

Overall, these results show that the presence of RRL in tidal tails is linked to the late stages of cluster dissolution. Streams with an associated progenitor whose RRL are mostly in the tails are rare and likely represent a brief evolutionary stage, while the majority of systems retain nearly all of their RRL in the progenitor, consistent with the predictions of mass segregation.

5.3 Intrinsic dispersions

In this work, we have consistently obtained intrinsic proper motion dispersions, as described in Sec. 4, for 70 of 75 tracks with proper motion information in the `galstreams` library.

The dispersions that we found might appear large if we compare them with Li et al. (2022), who, after analyzing a dozen stellar streams with S^5 data, concluded that globular cluster streams have velocity dispersions lower than ∼ 5 km/s. However, there are several independent examples of robust cases with high velocity dispersions that are consistent with our results, such as Balasubramaniam et al. (in prep., private communication), who found that the Turranburra and Elqui streams have dispersions of 24.2 km/s and 28.5 km/s, respectively. In addition, theoretical studies, like Errani et al. (2015) and Peñarrubia et al. (2025), argue that dwarf galaxies embedded in a dark matter halo can

be affected by the dark matter profile (core/cusp nuclei) or by interactions with dark matter subhalos, heating up the system and inflating their velocity dispersions.

Moreover, Helmi et al. (1999) showed through numerical simulations that the velocity dispersion of stellar streams can increase significantly at orbital turning points (apocentres or pericentres). In Fig. 5.2, we present the intrinsic tangential velocity dispersion of the streams inferred in this work, σ_{v_t}, as a function of their orbital phase. The left panel shows the 17 streams with associated progenitors, where the orbital phase information was taken from the DbGC (see Sec. 2), and the tangential velocity dispersions were computed using the median stream distances reported in `galstreams`. The right panel displays 39 of the 57 analyzed streams with physically consistent orbital phase information ($0 < \frac{R_{\rm gc}-R_{\rm peri}}{R_{\rm apo}-R_{\rm peri}} < 1$) reported by Bonaca & Price-Whelan (2025); the tangential velocity dispersions were calculated using the mean stream distances also reported by Bonaca & Price-Whelan (2025).

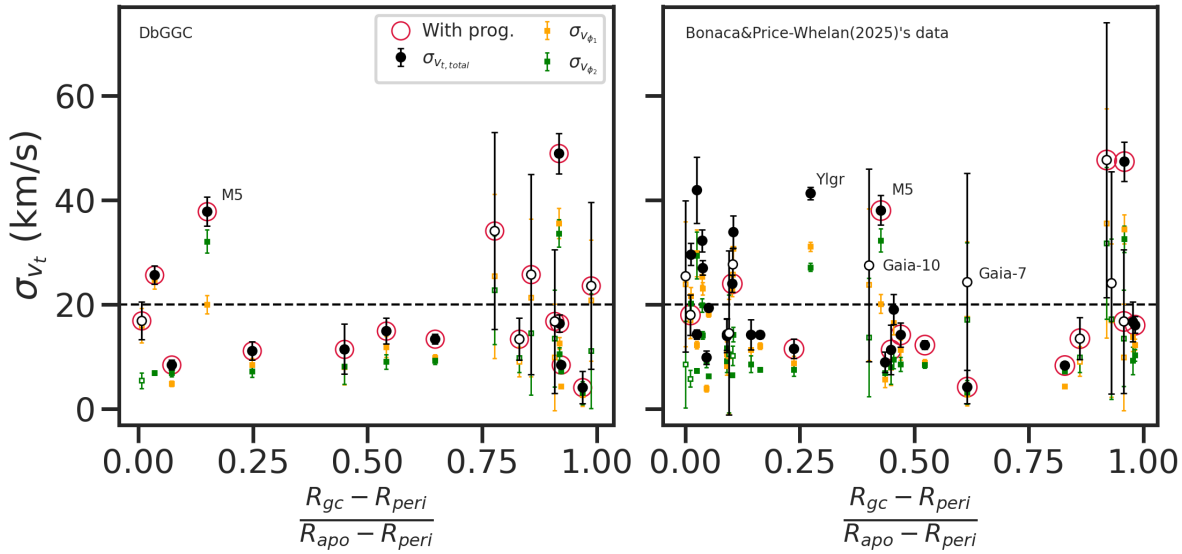

Figure 5.2: Intrinsic tangential velocity dispersion of the streams as function of their orbital phase. **Left:** The 17 streams studied with an associated progenitor which orbital phase information is obtained from the DbGC. **Right:** The 39 streams studied with physically consist orbital phase information reported in Bonaca & Price-Whelan (2025). The orange and green squares are the velocity dispersions in the components along and perpendicular to the stream, respectively; and the black circles are total velocity dispersions. Fill and empty symbols are the streams with and without members already reported in the literature, respectively; and therefore, with and without prior information of their intrinsic tangential velocity dispersion. The red empty circles indicates the streams associated with a progenitor.

Among the streams shown in the left panel, 6 out of 17 present velocity dispersions higher than 20 km/s, all located near orbital turning points. Similarly, in the right panel, 16 out of 39 streams show high dispersions, 75% of which are also found near turning points. The correlation between high dispersions and orbital turning points is consistent with the results of Helmi et al. (1999) and indicates that these high inferred dispersions might be an actual dynamical feature. Additionally, in the streams that have members already reported in the literature (filled symbols in Fig. 5.2), we used them to obtain a reference value of the intrinsic dispersions, which then served as the prior for our RRL-based inference (see Sec. 3.2.2). The dispersions inferred from these reported members were already large, and our results are consistent with them.

The main difference between the two panels of Fig. 5.2 is the orbital phase of the streams, which depends on the assumed Galactic potential and the accuracy of the orbital information of the object. Since the streams with progenitors have more robust orbital information, DbGC's orbital phases are

more trustworthy; however, Bonaca & Price-Whelan (2025) do not limit themselves to streams with a surviving progenitor. In particular, we highlight the case of M5, where using the orbital phase of 0.43 reported by Bonaca & Price-Whelan (2025) would result in an anomalously high dispersion. In contrast, adopting the – more reliable – orbital phase of 0.15 reported in the DbGC yields a dispersion consistent with Helmi et al. (1999) results. A similar situation might also be occurring in the other three anomalous cases: Gaia–7, Gaia–10, and Ylgr.

In summary, while our intrinsic dispersions may appear large, there are several studies, both theoretical and observational, that are consistent with our results. The ones that appear unusually large (>20 km/s) correspond to streams that are located at the turning points of their orbits, consistent with Helmi et al. (1999) predictions.

Chapter 6

Conclusions

In this work, we have presented the first systematic census of RRL stars kinematically associated with known stellar streams, motivated by the need for a homogeneous and distance-precise tracer that enables a full characterization of the streams. We constructed a probabilistic membership model based on proper motion and distance information, which identifies the RRL associated with known streams with proper motion reported in `galstreams`, and used these RRL to derive distance gradients (or anchor mean distances) as a function of an angular coordinate along the stream, to establish their intrinsic dispersions, and to study and compare the RRL population of the streams and their progenitors.

For our search we used a compilation of the largest Milky Way RRL catalogs (Gaia SOS, PS1, and ASAS-SN-II), with $\sim 2.8 \times 10^5$ RRL after quality cuts. Among the 56 streams (75 tracks) that we studied, 17 have an associated progenitor and 39 do not; there were 12 streams with more than one track reported in the literature. Of those with a surviving progenitor, we identified RRL in the tails of 13 stellar streams, 5 of them with more than 3 RRL. Of those with no progenitor, we identified RRL in 20 stellar streams, 9 of them with more than 3 RRL. We recover and expand previously known RRL associations, identifying new candidate members; except in the case of the GD-1 stream, in all the other 32 streams where we identify RRL, we detect at least one new member. We summarize the properties of the tracks in Tables 4.2 and give a list of the candidate members for each track in Table B.1.

Another important result of the census is that in all the streams with identified RRL we were able to anchor more precise distances to streams with only a mean value, confirm already reported distance gradients, and, in particular, infer new distance gradients to 5 streams: both components of Jhelum, LMS-1, Turranburra, Indus, and Elqui. This improved distance information is crucial to make full phase-space studies of the stellar streams themselves and of the Galaxy, such as inferring the Galactic potential from their orbits, studying the nature of the dark matter, or rebuilding the assembly history of the Milky Way.

From a global perspective, the census discards some particular patterns and reveals others.

1. The segregation by RRL type reported in the Pal 5 stream by Price-Whelan et al. (2019) was recovered. A similar effect is not observed in any of the other streams; thus, it is safe to conclude that this is a peculiarity of this particular stream, whose origin remains elusive.

2. Particular segregations by Oosterhoff were observed in three streams; in one case, it is likely contamination from the LMC (Cetus-Palca), in another it might be due to the RRL leaving the zero-age horizontal branch (AAU), and in the other it is due to a bimodality in the metallicity of the RRL population (M92).

3. The bimodality in metallicity observed in three streams (ωCen, Jhelum, and M92) reflects a complex origin story; in particular, for the case of Jhelum, this supports the scenario where

the stream is the result of a globular cluster (narrow component) and a dwarf galaxy (broad component) accreted and disrupted by the Galaxy. For the case of M92, we propose the scenario in which M92 is the nuclear star cluster of a disrupted host dwarf galaxy responsible for the stream observed by I21; meanwhile, the Sollima (2020)'s and T20's tracks might trace the tidal tails of the cluster; to confirm these hypotheses, more information and analysis are needed; in particular, proper motion data for the T20 tracks is required.

4. Streams with an associated progenitor that have a large fraction of their RRL in the tidal tails are uncommon and appear to trace progenitors in advanced stages of dissolution (e.g., Tucana III and Pal 5), consistent with expectations from mass segregation and cluster evolution (Balbinot & Gieles, 2018).

5. We have consistently obtained, for the first time, intrinsic velocity dispersions for 70 of the 75 tracks with proper motion information in the `galstreams` library. This is a relevant contribution of this work, as it is required by automated searches, such as the census conducted here, and it should facilitate similar future studies not limited to RRL stars. This information will be added to `galstreams` in its next version.

6. The intrinsic velocity dispersions inferred for several streams are large (Li et al., 2022); these large dispersions correlate in many cases with orbital turning points (Helmi et al., 1999) and with previously reported high-dispersion samples, suggesting that some measured dispersions might be real dynamical features; however, reliable inference requires larger tracer samples than the small-number statistics of the RRL.

In summary, this first systematic RRL census across all known streams with reported distances and proper motions provides a step forward in a homogeneous characterization of the Milky Way tidal debris. These results expand the knowledge of the known (RRL) members in many streams, anchor precise distances, and reveal patterns in RRL populations that shed light on the progenitor lifetimes and the stream formation scenarios. The method presented here can be applied to other types of standard candles, and the catalog of high-probability members can be combined with spectroscopic follow-up to obtain full phase-space information. Such combined analyzes will allow for more reliable inference of stream properties and improved constraints on the Galactic potential.

The experience and results of the census also leave us with lessons on aspects that can be improved. We highlight the sensitivity of the method to the choice of tracks. In more than one case, an identified RRL was classified as a member according to one track but not by others. In addition, some streams associated with a progenitor have reported tracks in the literature that show mismatches in sky position (e.g., ω Cen), distance (e.g., M68–Fjörm), and/or proper motion (e.g., NGC 1851) relative to their progenitor. This census represents a first approach to find out which of the studied streams contain a significant number of RRL based on the currently reported tracks. In future work, these issues could be addressed by running the inference blindly where possible and, in addition, inferring new RRL–based tracks for streams with sufficient members, as well as for those lacking any prior information.

Bibliography

Abbas, M., Grebel, E. K., & Simunovic, M. 2021, ApJ, 915, 49

Alexander, P. E. R., Gieles, M., Lamers, H. J. G. L. M., & Baumgardt, H. 2014, MNRAS, 442, 1265

Antoja, T., Ramos, P., Mateu, C., et al. 2020, A&A, 635, L3

Awad, P., Canducci, M., Balbinot, E., et al. 2023, arXiv e-prints, arXiv:2312.12524

Balbinot, E. & Gieles, M. 2018, MNRAS, 474, 2479

Baumgardt, H., Hénault-Brunet, V., Dickson, N., & Sollima, A. 2023, MNRAS, 521, 3991

Baumgardt, H. & Hilker, M. 2018, MNRAS, 478, 1520

Baumgardt, H., Hilker, M., Sollima, A., & Bellini, A. 2019, MNRAS, 482, 5138

Baumgardt, H. & Vasiliev, E. 2021, MNRAS, 505, 5957

Bellini, A., Libralato, M., Bedin, L. R., et al. 2018, ApJ, 853, 86

Belokurov, V., Deason, A. J., Koposov, S. E., et al. 2018, MNRAS, 477, 1472

Belokurov, V., Evans, N. W., Irwin, M. J., Hewett, P. C., & Wilkinson, M. I. 2006, ApJ, 637, L29

Belokurov, V., Evans, N. W., Irwin, M. J., et al. 2007, ApJ, 658, 337

Bonaca, A., Conroy, C., Price-Whelan, A. M., & Hogg, D. W. 2019a, ApJ, 881, L37

Bonaca, A., Geha, M., & Kallivayalil, N. 2012, ApJ, 760, L6

Bonaca, A., Hogg, D. W., Price-Whelan, A. M., & Conroy, C. 2019b, ApJ, 880, 38

Bonaca, A., Naidu, R. P., Conroy, C., et al. 2021, ApJ, 909, L26

Bonaca, A. & Price-Whelan, A. M. 2025, New A Rev., 100, 101713

Cabrera-Gadea, M., Mateu, C., & Ramos, P. 2024, arXiv e-prints, arXiv:2410.22427

Cacciari, C., Corwin, T. M., & Carney, B. W. 2005, AJ, 129, 267

Caldwell, N., Bonaca, A., Price-Whelan, A. M., Sesar, B., & Walker, M. G. 2020, AJ, 159, 287

Callingham, T. M., Cautun, M., Deason, A. J., et al. 2022, MNRAS, 513, 4107

Carballo-Bello, J. A., Martínez-Delgado, D., Navarrete, C., et al. 2018, MNRAS, 474, 683

Carballo-Bello, J. A., Sollima, A., Martínez-Delgado, D., et al. 2014, MNRAS, 445, 2971

Carretta, E., Bragaglia, A., Gratton, R., D'Orazi, V., & Lucatello, S. 2009, A&A, 508, 695

Catelan, M. & Smith, H. A. 2015, Pulsating Stars

Chandra, V., Conroy, C., Caldwell, N., et al. 2022, ApJ, 940, 127

Chang, J., Yuan, Z., Xue, X.-X., et al. 2020, ApJ, 905, 100

Clement, C. 2017, in European Physical Journal Web of Conferences, Vol. 152, European Physical Journal Web of Conferences, 01021

Clementini, G., Ripepi, V., Garofalo, A., et al. 2023, A&A, 674, A18

Clementini, G., Ripepi, V., Molinaro, R., et al. 2019, A&A, 622, A60

Combes, F., Leon, S., & Meylan, G. 1999, A&A, 352, 149

Cruz Reyes, M., Anderson, R. I., Johansson, L., Netzel, H., & Medaric, Z. 2024, A&A, 684, A173

de Boer, T. J. L., Belokurov, V., & Koposov, S. E. 2018, MNRAS, 473, 647

de Boer, T. J. L., Erkal, D., & Gieles, M. 2020, MNRAS, 494, 5315

Deason, A. J. & Belokurov, V. 2024, New A Rev., 99, 101706

Drlica-Wagner, A., Bechtol, K., Rykoff, E. S., et al. 2015, ApJ, 813, 109

Errani, R., Penarrubia, J., & Tormen, G. 2015, MNRAS, 449, L46

Eyre, A. & Binney, J. 2009, MNRAS, 399, L160

Fahrion, K., Müller, O., Rejkuba, M., et al. 2020, A&A, 634, A53

Ferguson, P. S., Shipp, N., Drlica-Wagner, A., et al. 2022, AJ, 163, 18

Foreman-Mackey, D. 2014, Blog Post: Mixture Models, version 1, Zenodo

Foreman-Mackey, D., Hogg, D. W., Lang, D., & Goodman, J. 2013, PASP, 125, 306

Gaia Collaboration, Prusti, T., de Bruijne, J. H. J., et al. 2016, A&A, 595, A1

Gieles, M., Alexander, P. E. R., Lamers, H. J. G. L. M., & Baumgardt, H. 2014, MNRAS, 437, 916

Grand, R. J. J., Fragkoudi, F., Gómez, F. A., et al. 2024, MNRAS, 532, 1814

Grand, R. J. J., Gómez, F. A., Marinacci, F., et al. 2017, MNRAS, 467, 179

Grillmair, C. J. 2006, ApJ, 645, L37

Grillmair, C. J. 2019, ApJ, 884, 174

Grillmair, C. J. 2022, ApJ, 929, 89

Grillmair, C. J. & Dionatos, O. 2006, ApJ, 643, L17

Grillmair, C. J. & Johnson, R. 2006, ApJ, 639, L17

Hanke, M., Koch, A., Prudil, Z., Grebel, E. K., & Bastian, U. 2020, A&A, 637, A98

Hansen, T. T., Ji, A. P., Da Costa, G. S., et al. 2021, ApJ, 915, 103

Hansen, T. T., Riley, A. H., Strigari, L. E., et al. 2020, ApJ, 901, 23

Helmi, A. 2020, ARA&A, 58, 205

Helmi, A., White, S. D. M., de Zeeuw, P. T., & Zhao, H. 1999, Nature, 402, 53

Hendel, D., Scowcroft, V., Johnston, K. V., et al. 2018, MNRAS, 479, 570

Holoien, T. W. S., Marshall, P. J., & Wechsler, R. H. 2017, XDGMM: eXtreme Deconvolution Gaussian Mixture Modeling, Astrophysics Source Code Library, record ascl:1708.026

Huang, K.-W. & Koposov, S. E. 2022, MNRAS, 510, 3575

Ibata, R., Bellazzini, M., Thomas, G., et al. 2020, ApJ, 891, L19

Ibata, R., Malhan, K., Martin, N., et al. 2021, ApJ, 914, 123

Ibata, R., Malhan, K., Tenachi, W., et al. 2024, ApJ, 967, 89

Ibata, R. A., Bellazzini, M., Malhan, K., Martin, N., & Bianchini, P. 2019a, Nature Astronomy, 3, 667

Ibata, R. A., Lewis, G. F., Thomas, G., Martin, N. F., & Chapman, S. 2017, ApJ, 842, 120

Ibata, R. A., Malhan, K., & Martin, N. F. 2019b, ApJ, 872, 152

Ibata, R. A., Malhan, K., Martin, N. F., & Starkenburg, E. 2018, ApJ, 865, 85

Iorio, G. & Belokurov, V. 2021, MNRAS, 502, 5686

Jayasinghe, T., Stanek, K. Z., Kochanek, C. S., et al. 2019, MNRAS, 486, 1907

Jensen, J., Thomas, G., McConnachie, A. W., et al. 2021, MNRAS, 507, 1923

Ji, A. P., Li, T. S., Hansen, T. T., et al. 2020, AJ, 160, 181

Johnson, C. I. & Pilachowski, C. A. 2010, ApJ, 722, 1373

Kirby, E. N., Cohen, J. G., Guhathakurta, P., et al. 2013, ApJ, 779, 102

Koposov, S. E., Belokurov, V., Li, T. S., et al. 2019, MNRAS, 485, 4726

Koposov, S. E., Erkal, D., Li, T. S., et al. 2023, MNRAS, 521, 4936

Koposov, S. E., Irwin, M., Belokurov, V., et al. 2014, MNRAS, 442, L85

Koposov, S. E., Rix, H.-W., & Hogg, D. W. 2010, ApJ, 712, 260

Kruijssen, J. M. D., Pfeffer, J. L., Reina-Campos, M., Crain, R. A., & Bastian, N. 2019, MNRAS, 486, 3180

Kunder, A., Popowski, P., Cook, K. H., & Chaboyer, B. 2008, AJ, 135, 631

Kundu, R., Minniti, D., & Singh, H. P. 2019, MNRAS, 483, 1737

Kundu, R., Navarrete, C., Fernández-Trincado, J. G., et al. 2021, A&A, 645, A116

Kuzma, P. B., Da Costa, G. S., & Mackey, A. D. 2018, MNRAS, 473, 2881

Kuzma, P. B., Da Costa, G. S., Mackey, A. D., & Roderick, T. A. 2016, MNRAS, 461, 3639

Kuzma, P. B. & Ishigaki, M. N. 2025, MNRAS, 537, 2752

Laporte, C. F. P., Belokurov, V., Koposov, S. E., Smith, M. C., & Hill, V. 2020, MNRAS, 492, L61

Li, T. S., Ji, A. P., Pace, A. B., et al. 2022, ApJ, 928, 30

Li, T. S., Koposov, S. E., Erkal, D., et al. 2021, ApJ, 911, 149

Li, T. S., Koposov, S. E., Zucker, D. B., et al. 2019, MNRAS, 490, 3508

Li, X.-Y., Huang, Y., Liu, G.-C., Beers, T. C., & Zhang, H.-W. 2023, ApJ, 944, 88

Lindegren, L., Klioner, S. A., Hernández, J., et al. 2021, A&A, 649, A2

Majewski, S. R., Patterson, R. J., Dinescu, D. I., et al. 2000, in Liege International Astrophysical Colloquia, Vol. 35, Liege International Astrophysical Colloquia, ed. Noels, A., Magain, P., Caro, D., et al., 619

Malhan, K., Ibata, R. A., Carlberg, R. G., Valluri, M., & Freese, K. 2019, ApJ, 881, 106

Malhan, K., Valluri, M., & Freese, K. 2021a, MNRAS, 501, 179

Malhan, K., Yuan, Z., Ibata, R. A., et al. 2021b, ApJ, 920, 51

Martin, C., Carlin, J. L., Newberg, H. J., & Grillmair, C. 2013, ApJ, 765, L39

Mateu, C. 2023, MNRAS, 520, 5225

Mateu, C. 2024, Research Notes of the American Astronomical Society, 8, 85

Mateu, C., Holl, B., De Ridder, J., & Rimoldini, L. 2020, MNRAS, 496, 3291

Mateu, C. & Vivas, A. K. 2018, MNRAS, 479, 211

Medina, G. E., Muñoz, R. R., Vivas, A. K., et al. 2018, ApJ, 855, 43

Moreno, E., Pichardo, B., & Velázquez, H. 2014, ApJ, 793, 110

Naidu, R. P., Conroy, C., Bonaca, A., et al. 2020, ApJ, 901, 48

Newberg, H. J., Yanny, B., & Willett, B. A. 2009, ApJ, 700, L61

Nibauer, J. & Bonaca, A. 2025, ApJ, 985, L22

Odenkirchen, M. & Grebel, E. K. 2004, in Astronomical Society of the Pacific Conference Series, Vol. 327, Satellites and Tidal Streams, ed. Prada, F., Martinez Delgado, D., & Mahoney, T. J., 284

Odenkirchen, M., Grebel, E. K., Rockosi, C. M., et al. 2001, ApJ, 548, L165

Olszewski, E. W., Saha, A., Knezek, P., et al. 2009, AJ, 138, 1570

Palau, C. G. & Miralda-Escudé, J. 2019, MNRAS, 488, 1535

Palau, C. G. & Miralda-Escudé, J. 2021, MNRAS, 504, 2727

Palau, C. G., Wang, W., & Han, J. 2025, MNRAS, 539, 2718

Peñarrubia, J., Errani, R., Vitral, E., & Walker, M. G. 2025, MNRAS [arXiv:2506.03904]

Pilkington, K., Few, C. G., Gibson, B. K., et al. 2012, A&A, 540, A56

Price-Whelan, A. M. & Bonaca, A. 2018, ApJ, 863, L20

Price-Whelan, A. M., Mateu, C., Iorio, G., et al. 2019, AJ, 158, 223

Prudil, Z., Kunder, A., Dékány, I., & Koch-Hansen, A. J. 2024a, A&A, 684, A176

Prudil, Z., Smolec, R., Kunder, A., Koch-Hansen, A. J., & Dékány, I. 2024b, A&A, 685, A153

Ramos, P., Antoja, T., Mateu, C., et al. 2021, A&A, 646, A99

Ramos, P., Antoja, T., Yuan, Z., et al. 2022, A&A, 666, A64

Ramos, P., Mateu, C., Antoja, T., et al. 2020, A&A, 638, A104

Riley, A. H., Bieri, R., Deason, A. J., et al. 2025, arXiv e-prints, arXiv:2509.06859

Rockosi, C. M., Odenkirchen, M., Grebel, E. K., et al. 2002, AJ, 124, 349

Searle, L. & Zinn, R. 1978, ApJ, 225, 357

Sesar, B., Grillmair, C. J., Cohen, J. G., et al. 2013, ApJ, 776, 26

Sesar, B., Hernitschek, N., Mitrović, S., et al. 2017, AJ, 153, 204

Shipp, N., Drlica-Wagner, A., Balbinot, E., et al. 2018, ApJ, 862, 114

Shipp, N., Li, T. S., Pace, A. B., et al. 2019, ApJ, 885, 3

Smith, H. A. 1995, Cambridge Astrophysics Series, 27

Sollima, A. 2020, MNRAS, 495, 2222

Soszyński, I., Udalski, A., Szymański, M. K., et al. 2016, Acta Astron., 66, 131

Spitzer, L. 1987, Dynamical evolution of globular clusters

Starkman, N., Bovy, J., & Webb, J. J. 2020, MNRAS, 493, 4978

Stringer, K. M., Drlica-Wagner, A., Macri, L., et al. 2021, ApJ, 911, 109

Tau, E. A., Vivas, A. K., & Martínez-Vázquez, C. E. 2024, AJ, 167, 57

Tavangar, K. & Price-Whelan, A. M. 2025, arXiv e-prints, arXiv:2502.13236

Thomas, G. F. & Battaglia, G. 2022, A&A, 660, A29

Thomas, G. F., Jensen, J., McConnachie, A., et al. 2020, ApJ, 902, 89

Valluri, M., Fagrelius, P., Koposov, S. E., et al. 2025, ApJ, 980, 71

Vasiliev, E. & Baumgardt, H. 2021, MNRAS, 505, 5978

Viswanathan, A., Starkenburg, E., Koppelman, H. H., et al. 2023, MNRAS, 521, 2087

Vivas, A. K., Martínez-Vázquez, C., & Walker, A. R. 2020, ApJS, 247, 35

Vivas, A. K., Zinn, R., & Gallart, C. 2006a, in Revista Mexicana de Astronomia y Astrofisica Conference Series, Vol. 25, Revista Mexicana de Astronomia y Astrofisica Conference Series, ed. Abad, C., Bongiovanni, A., & Guillen, Y., 37–40

Vivas, A. K., Zinn, R., Subero, Y., & Hernández, J. 2006b, in Revista Mexicana de Astronomia y Astrofisica Conference Series, Vol. 26, Revista Mexicana de Astronomia y Astrofisica Conference Series, 60–63

Wang, F., Zhang, H. W., Xue, X. X., et al. 2022, MNRAS, 513, 1958

Webb, J. J., Harris, W. E., Sills, A., & Hurley, J. R. 2013, ApJ, 764, 124

Weiss, J., Newberg, H. J., & Desell, T. 2018, ApJ, 867, L1

White, S. D. M. & Frenk, C. S. 1991, ApJ, 379, 52

White, S. D. M. & Rees, M. J. 1978, MNRAS, 183, 341

Williams, M. E. K., Steinmetz, M., Sharma, S., et al. 2011, ApJ, 728, 102

Woudenberg, H. C., Koop, O., Balbinot, E., & Helmi, A. 2023, A&A, 669, A102

Xu, C., Tang, B., Li, C., et al. 2024, A&A, 684, A205

Yang, Y., Zhao, J.-K., Tang, X.-Z., Ye, X.-H., & Zhao, G. 2023, ApJ, 953, 130

Ying, J. M., Chaboyer, B., Boudreaux, E. M., et al. 2023, AJ, 166, 18

York, D. G., Adelman, J., Anderson, Jr., J. E., et al. 2000, AJ, 120, 1579

Yuan, Z., Chang, J., Beers, T. C., & Huang, Y. 2020, ApJ, 898, L37

Yuan, Z., Malhan, K., Sestito, F., et al. 2022, ApJ, 930, 103

Yuan, Z., Matsuno, T., Sitnova, T., et al. 2025, arXiv e-prints, arXiv:2502.09710

Yuan, Z., Smith, M. C., Xue, X.-X., et al. 2019, ApJ, 881, 164

Zinn, R. 1993, in Astronomical Society of the Pacific Conference Series, Vol. 48, The Globular Cluster-Galaxy Connection, ed. Smith, G. H. & Brodie, J. P., 38

Zinn, R., Horowitz, B., Vivas, A. K., et al. 2014, ApJ, 781, 22

Appendix A

Properties used for each track

In Table A.1 we show all the technical properties needed to reproduce our work: the ranges in ϕ_1, ϕ_2 and distance of the sample box for each track studied with its reference, the observational width of the stream, the number of RRL in the whole window and in the on and off stream regions, the number of Gaussians used for the background model, the ratio between the extended on-stream region and its complementary area in the sky window, the tidal radius and heliocentric distance of the progenitor when it is still alive, and whether there are previous reported members with proper motion and distance information. The full table can be found in a public repository[1].

Table A.1: First 5 rows of a summary of properties used for each track. (1) Name of the track on `galstreams` (2) Name of the corresponding stream (3) ϕ_1 range of the box sample (4) ϕ_2 range of the sample box (5) Distance range of the box sample (6) Sky width from `galstreams` (7) Whether are members with proper motion information available reported in the literature (8) Whether are members with distance information available reported in the literature (9) Whether the stream has a progenitor associated with (10) Tidal radius of the progenitor (11) Heliocentric distance of the progenitor (12) Total number of RRL in the sample box (*tot*), the on-stream region (*st*), and the off-stream region (*bkg*) (13) Number of Gaussians used for the background model (14) Reference of the track.

TrackName	StreamName	ϕ_1 range (°)	ϕ_2 range (°)	d range (kpc)	σ_{ϕ_2} (°)	pm avai.	d avai.	Prog.	r_t (pc)	$d_{\rm prog}$ (kpc)	N *(tot, st, bkg)*	N *BIC*	Ref. (*)
AAU-ATLAS-L21	AAU-ATLAS	(-18.33, 16.92)	(-3.60, 4.05)	(11.06, 39.60)	0.30	T	T	F	-	-	117, 26, 48	3	(1)
AAU-AliqaUma-L21	AAU-AliqaUma	(8.19, 22.44)	(-4.76, 3.83)	(14.77, 45.46)	0.26	T	T	F	-	-	39, 6, 17	1	(1)
ATLAS-I21	ATLAS	(-13.55, 13.55)	(-4.39, 4.33)	(4.42, 45,92)	0.35	T	T	F	-	-	162, 31, 65	3	(2)
Aquarius-W11	Aquarius	(-9.28, 9.19)	(-42.04, 42.36)	(1.78, 7.29)	3.78	F	F	F	-	-	264, 44, 143	2	(3)
C-19-I21	C-19	(-21.43, 23.16)	(-8.71, 8.35)	(10.80, 25.20)	0.76	F	F	F	-	-	398, 74, 224	3	(2)
				...									

(*) **References:** (1): Li et al. (2021), (2): I21, (3): Williams et al. (2011), (4): Shipp et al. (2019), (5): Yuan et al. (2022), (6): Thomas & Battaglia (2022), (7): Price-Whelan & Bonaca (2018), (8): Ferguson et al. (2022), (9): Bonaca et al. (2019a), (10): Malhan et al. (2021a), (11): Grillmair (2022), (12): Yang et al. (2023), (13): Grillmair (2019), (14): Palau & Miralda-Escudé (2019), (15): Palau & Miralda-Escudé (2021), (16): Caldwell et al. (2020), (17): Koposov et al. (2019), (18): Koposov et al. (2023), (19): Price-Whelan et al. (2019), (20): Chandra et al. (2022).

[1] `https://drive.google.com/drive/folders/1XoqzaVN2Xco60stMNMh3Ow8FCRFCZqTE?usp=sharing`: This link will be replace for a Zenodo permanent publication link upon approval of this work.

Appendix B

Membership probability of RRL

In Table B.1 we show all the RRL with $p_{\rm memb} > 0.5$ and their properties: distance, period, amplitude, type, and photometric metallicity. The RRL that are identified as members are tagged as `Member detection = T`. The full table can be found in the same repository as the Table A.1.

Table B.1: First 5 rows of the RRL with a probability higher than 50% of belonging to one of the studied tracks. If the star is closer than $3\sigma_{\phi_2}$ from the sky track then is considered a member of the stream (Member detection = T), if not it is used to estimate the number of contaminants. The metallicity provenance indicate if the metallicity of the RRL was obtained from Li et al. (2023, Li23) or drawn from the metallicity distribution of the halo (Halo run). The period and amplitude uncertainties are $\sim 5 \times 10^{-6}$ days and ~ 0.02 mag, respectively.

Gaia DR3 `source_id`	d (kpc)	Period (d)	Amp.-V (mag)	Type	[Fe/H] adopted	[Fe/H] provenance	$P_{\rm memb}$	Member detection	TrackName
2350310424833246592	18.70 ± 0.89	0.592307	1.08	RRab	-2.15 ± 0.27	Li23	1.00	T	AAU-ATLAS-L21
2346142279330813184	20.4 ± 1.3	0.572475	0.83	RRab	-2.23 ± 0.39	Li23	1.00	T	AAU-ATLAS-L21
5039937417965798656	19.4 ± 1.1	0.327495	0.42	RRc	-1.51 ± 0.20	Halo run	1.00	T	AAU-ATLAS-L21
5040718998934473472	21.7 ± 1.0	0.599083	1.14	RRab	-2.10 ± 0.26	Li23	1.00	T	AAU-ATLAS-L21
2362676975707859584	18.0 ± 1.6	0.676645	0.69	RRab	-2.06 ± 0.52	Li23	1.00	T	AAU-ATLAS-L21
...									